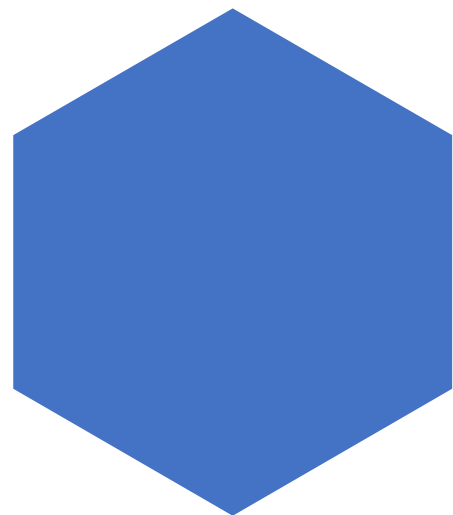
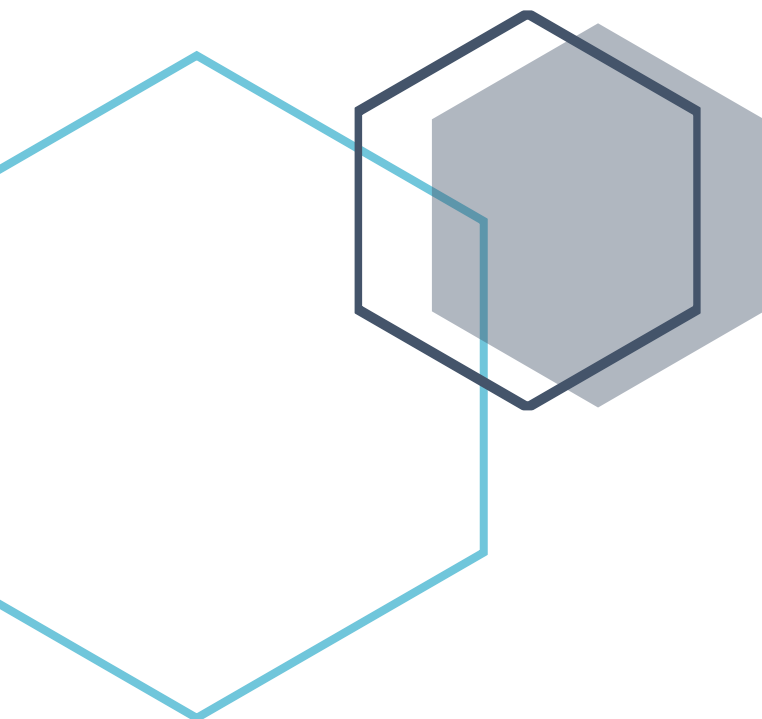




# Hydrogenated Indium Oxide (IO:H) by Plasma Enhanced Spatial Atomic Layer Deposition for Thin film PV Application

Saksham Pandey – MSc Thesis





# Hydrogenated Indium Oxide (IO:H) by Plasma Enhanced Spatial Atomic Layer Deposition for Thin film PV Application.

By

Saksham Pandey

in partial fulfilment of the requirements for the degree of

**Master of Science**

in Sustainable Energy Technology

at the Delft University of Technology,

to be defended publicly on Monday August 26, 2019 at 3:00 PM.

Supervisor:	Dr. ir. Yves Creyghton	TNO
	Prof Dr.Olindo Isabella	TU Delft
Thesis committee:	Prof Dr.Olindo Isabella	TU Delft
	Dr. Gregory Pandraud	TU Delft
	Dr. Sten Vollebregt	TU Delft
	Dr. ir. Yves Creyghton	TNO

*This thesis is confidential and cannot be made public until August 26, 2021.*

An electronic version of this thesis is available at <http://repository.tudelft.nl/>.



# Abstract

Hydrogenated Indium Oxide (IOH) has been recognized as a high performance transparent conductive oxide (TCO) due to its excellent mobility ( $>100 \text{ cm}^2/\text{Vs}$ ) and high transparency ( $>90\%$ ) in the visible and near infrared region of the spectrum.

Plasma enhanced spatial atomic layer deposition (PESALD), a new type of deposition process developed recently at TNO has been used to perform the deposition of IOH in this project. Sputtering is a process conventionally used in the industry for the deposition of TCO. However, PESALD offers several benefits when compared to sputtering. The process is continuous, operated at atmospheric pressure allowing large area and high throughput processing. In addition to this, PESALD uses a fully remote plasma source to avoid any substrate damage caused by the bombardment of ions. Ion-induced substrate damage could sometimes pose a problem in magnetron plasma sputter deposition processes.

Different process parameters like precursor pickup flow, gas concentration in the plasma, substrate velocity and reactor temperature were altered in order to find improved conditions for IOH depositions. A novel dimethylaminopropyl-dimethylindium (DADI) precursor was used and the impact of its use was studied at different process conditions. In order to find the more optimal conditions, the IOH layers were deposited and characterized on glass substrate. Spectroscopic ellipsometry (SE), Hall effect measurements 4 point probe measurements, reflectance and transmittance measurements and X-ray diffraction were used for analysing growth, electrical, optical and structural properties of the layers. SCOUT software is also used for a better optical analysis of the films. Additionally, the degradation of the layers under damp heat and atmospheric conditions is investigated during the course of this project. Finally, the most optimum PESALD process parameters have been used to perform deposition of the TCO on CIGS solar cells.

# Contents

<b>Acknowledgement</b> .....	iv
<b>1 Introduction</b> .....	1
1.1. Solar energy.....	1
1.2. Thin film solar cells.....	2
1.2.1 CIGS solar cells .....	3
1.3. Transparent conductive oxides (TCO).....	3
1.3.1 Applicability .....	4
1.3.2 Electrical conductivity .....	5
1.3.3 Scattering mechanisms .....	7
1.3.4 Optical properties .....	9
1.4. Indium Oxide ( $\text{In}_2\text{O}_3$ ) .....	11
1.5. Motivation.....	12
1.6. Objective .....	13
1.8. Thesis Outline .....	13
<b>2 Literature review</b> .....	15
2.1. Thin film deposition techniques .....	15
2.1.1 Sputtering.....	15
2.1.2 Atomic layer deposition (ALD) .....	16
2.2. Review of transparent conductive oxides .....	17
2.2.1 Tin doped indium oxide (ITO) .....	17
2.2.2 Indium doped zinc oxide (IZO) .....	17
2.2.3 Zirconium doped indium oxide (IO:Zr) .....	17
2.2.4 Hydrogen doped indium oxide (IO:H) .....	17
2.3. TCOs on CIGS solar cell .....	20
2.4. Ageing of TCOs.....	20
<b>3 Plasma enhanced spatial atomic layer deposition</b> .....	22
3.1. Spatial atomic layer deposition (SALD) .....	22
3.2. Plasma enhanced spatial atomic layer deposition (PESALD).....	22
3.3 Metal Precursor.....	24
3.4 Plasma.....	26
3.4.1 Atmospheric plasma sources .....	26
3.4.2 Dielectric barrier discharge (DBD).....	27
3.4.3 Plasma source .....	29
3.5 ALD temperature window and non- uniformities .....	29

<b>4 IO:H deposited by plasma enhanced spatial atomic layer deposition</b> .....	32
4.1 Methodology .....	32
4.1.1 Growth analysis.....	33
4.1.2 Electrical analysis.....	34
4.1.3 Optical, structural & ageing analysis.....	34
4.2 Process Parameters.....	35
4.3 Process sensitivity.....	36
4.4 Growth and electrical properties.....	36
4.4.1 Influence of DADI precursor partial pressure.....	37
4.4.2 Influence of [H <sub>2</sub> ].....	39
4.4.3 Influence of substrate velocity .....	41
4.4.4 Influence of [H <sub>2</sub> O] in plasma and reactor temperature .....	44
4.5 Optical properties .....	47
4.6 Structural properties .....	52
4.7 Ageing.....	55
4.8 Conclusion & recommendations.....	58
<b>5 IO:H as TCO on CIGS solar cells</b> .....	60
5.1 Methodology .....	60
5.2 Reproducibility test.....	63
5.3 Motivation.....	63
5.4 Performance of CIGS solar cells .....	64
5.5 Conclusion & recommendations.....	68
<b>6 Conclusion</b> .....	69
<b>Recommendations</b> .....	70
<b>Appendix A</b> .....	73
Characterization techniques.....	73
IOH layer characterisation techniques.....	73
Four-Point Probe Setup .....	73
Ellipsometer Setup.....	73
Hall Measurement Setup.....	75
Spectrophotometer.....	76
X-ray diffraction.....	77
CIGS solar cell characterisation techniques .....	78
Illuminated J-V curve.....	78
External quantum efficiency (EQE) .....	78
<b>Appendix B</b> .....	79
Additional information.....	79

B.1 Expected growth and nucleation during the ALD process and subsequent solid phase crystallization by B. Macco. ....	79
B.2 Paschen's law.....	79
B.3 Process conditions used for determining the process sensitivity.....	80
B.4 Refractive index of amorphous and crystallized IO:H.....	81
B.5 Transmittance & reflectance measurements for IO:H samples at 6.7% [H <sub>2</sub> O] for variable reactor temperatures .....	82
B.6 Raman spectroscopy .....	83
B.7 Texture coefficient calculations for IO:H samples at 6.7% [H <sub>2</sub> O] for variable reactor temperatures.....	83
<b>Bibliography</b> .....	<b>84</b>

# Acknowledgement

First, and foremost I would like to thank Dr. ir. Yves Creyghton and TNO-Solliance for giving me this opportunity. This was my first experience at scientific research and I don't think I could have had a better guide. Yves, I really appreciate the transparency and clarity in our communication and the level of quality, precision and accuracy that you demanded from me, would be an honour to work with you again in the future. Next, I would like to thank Dr. Olindo Isabella for his regular feedback and suggestions, pertaining to the project. I am in awe with the efficient and precise nature of your suggestions, this helped me immensely to build the roadmap for this project. Here, I would also like to mention the contribution of Dr. Valerio Zardetto, who helped me in successfully applying the IO:H layer developed by PESALD process on to a CIGS solar cell. Finally, I am grateful of the ALD team at TNO-Solliance who were really supportive and appreciative of my research.

A lot of sincere gratitude also goes to my parents, because of whom I was able to get this opportunity. I would also like to thank all my friends in the Netherlands. Thanks for keeping me sane during this period. Finally, I am very grateful of Ms. Lis Andersen for constantly supporting me during my studies. Overall, I appreciate the time and effort put by everyone who was involved with this project in any way.

It was a pleasure to work on this interesting subject.

# 1 Introduction

“Keep your face to the sun and you will never see the shadows.”

—Hellen Keller

The power of the sun can be strongly felt from this quote. It is an irony that the person conveying this strong message to the world was herself blind. However, she was able to see what no one else could in those days.

This chapter provides a general introduction to this thesis. The importance of solar energy is indicated and the concept of second generation PV technology or thin film PV technology is elaborated. The main focus of this thesis is set on the transparent conductive oxide (TCO) layer of the thin film solar cell. Hydrogen doped indium oxide (IO:H) is the TCO investigated in this project due to its excellent electro-optical properties. Figure 1 depicts a TCO layer in a thin film solar cell. In thin film solar cells, the active semiconductor layer is sandwiched between a TCO layer and an electrical back contact [1]. The TCO layer may be deposited by using an innovative plasma enhanced spatial atomic layer deposition (PESALD) process which is discussed in detail in this thesis.

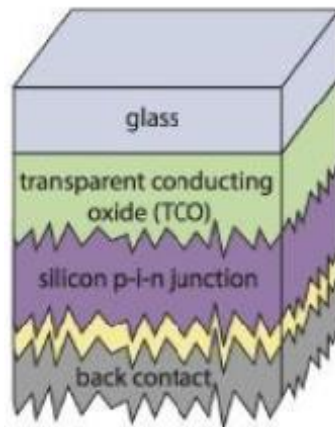


Figure 1 TCO layer in Tandem Cell Application [1]

## 1.1. Solar energy

In recent years, there has been a constant urge to switch to a cleaner and more renewable source of energy. Solar energy or the energy harvested from the light energy emitted by the sun is considered a frontrunner amongst all the renewable sources of energy. As a result of which a lot of research is being performed for developing high efficiency solar cells.

The sun's energy is converted into usable energy by using the concept of photovoltaic effect. The photovoltaic effect can be understood as the potential difference at the junction of two different materials in response to electromagnetic radiation [1]. This happens when the light from the sun is absorbed in a semiconductor material. This results in the formation of electron hole pair in the semiconductor and the movement of electrons from the valence band to the conduction band. Only light of certain wavelength can ensure the formation of electron hole pair. This is limited by the bandgap of the material. Hence, only photons having energy greater than the bandgap are able to contribute towards the formation of the electron hole pairs.

As it can be observed in Figure 2, the International Renewable Energy Agency reported that the global renewable energy generation capacity grew by 167 GW in 2017, displaying a stable growth of 8.3%. The

major contributor of this growth was solar energy, which grew by 32%. The main reason for this growth is attributed to the significant cost reductions experienced in the PV market. Between 2010-2017, the levelized cost of electricity from PV fell by 73%. The cost of PV technologies is already within range of fossil fuel based power. In 2017, 98 GW of PV installations came online, outpacing the year's combined new capacity installations of coal, gas and nuclear power. China leads the global capacity installations of PV, with nearly half of the capacity installed in 2017 followed by India [2].

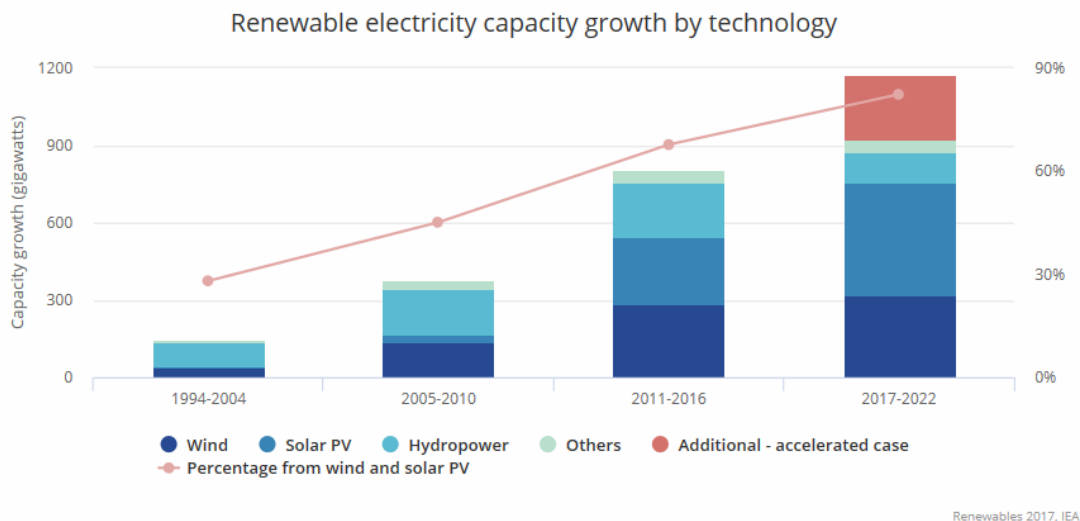


Figure 2 Renewable electricity growth by technology[3]

Overall, solar energy continues to establish its strong foothold in the energy market. Hence, working towards the research and development of new generation solar cells would only expedite the process of achieving a purely renewable based energy infrastructure.

## 1.2. Thin film solar cells

Currently, the PV technology is dominated by crystalline Si. However, as solar cells are more widely inculcated in our lifestyles a next generation of PV technology called as “Thin Film Solar Cell” is expected to play a major role in the solar energy infrastructure. These films are much thinner than the conventional first generation c-Si technology. This improves their flexibility and results in a lightweight layer. Thin film solar cells were also expected to be much cheaper than the conventional c-Si, however due to the current price decline in wafer based solar cells, they have not yet become economically viable [1]. However, in the future possibility of a decline in price of thin film solar cells cannot be discarded due to a favorable economy of scale.

The main motive of using thin film technology is its potential in relation to mass production. As compared to crystalline Si based modules which are entirely dependent on silicon, thin film solar cells are made by using a wide variety of PV materials like amorphous silicon, copper indium gallium selenide (CIGS), cadmium telluride (CdTe) and perovskites. All thin film technologies can be incorporated as building integrated photovoltaics (BIPV). A common characteristic amongst these technologies is their direct bandgap which enables them to be used as a very thin film. They also have a very low temperature coefficient which enables them to resist high temperatures [4].

Even though, the effectiveness of thin films in minimizing the material usage is evident its efficiency still remains relatively lower than wafer technology. Hence, both the agendas of minimum material and higher efficiency must be simultaneously met in order to produce energy at a low cost. In this thesis, applicability of the TCO by unique PESALD process for CIGS perovskite solar cells has been demonstrated. A brief insight into the growth and working of CIGS solar cells can be found in the next section.

## 1.2.1 CIGS solar cells

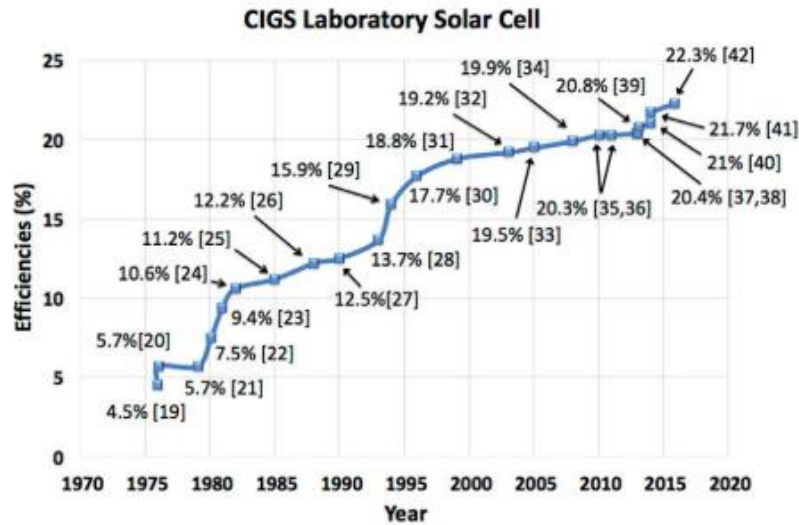


Figure 3 CIGS cell efficiency [5]

Figure 3 displays the growth of CIGS solar cell technology from 1976. CIGS based thin film solar cell modules represent the highest efficiency alternative for a large scale, commercial thin film solar cells. Single cell efficiency over 20% have been recorded as shown in the figure. Modules with efficiencies over 16% have also been recorded. The structure of the first CIGS solar cell is depicted in Figure 4b. The structure uses soda lime as the glass substrate. The glass is coated with molybdenum which acts as the rear contact for the p-type CIGS absorber layer. Mo reflects the unabsorbed light back into the bulk of the cell. The absorber layer in this case is merely 4.04  $\mu\text{m}$ , which is extremely thin compared to crystalline silicon at 170-200  $\mu\text{m}$  [5]. This is followed by the deposition of CdS on the absorber layer. CdS is deposited as an intermediate hole transport layer to improve the interface properties and act as a buffer layer to protect the CIGS absorber layer [6]. This is followed by a thin intrinsic ZnO layer, to protect the CdS and CIGS absorber layer during the deposition of the front contact typically by sputtering. Sputtering process is known to have a damaging effect for the underneath layer [7]. Finally, aluminium doped zinc oxide (AZO) is deposited as the front transparent contact. In this project, hydrogen doped indium oxide (IO:H) is used as a front contact and deposited by using a unique PESALD process on a similar CIGS solar cell architecture.

## 1.3. Transparent conductive oxides (TCO)

The main focus of this thesis is set upon developing a high performance transparent conductive oxide (TCO) layer of IO:H using PESALD. Hence, it is essential to get a thorough insight into the concept of a TCO. To simplify things, TCO can be merely understood as a transparent electrode. The simultaneous occurrence of high optical transparency (>80%) in the visible as well as near infrared region and low electrical resistivity close to that of metals (<1 m $\Omega\text{cm}$ ) is the primary quality that defines a TCO. As one might expect, these two characteristics are not mutually compatible and hence there is an active research in this field.

Thin film metal oxides of indium, cadmium, tin, zinc and their alloys can be doped accordingly to obtain the desired opto-electronic properties for a TCO. Defects present in the materials such as oxygen vacancies, impurities, substitutions and interstitials donate electrons in the conduction band of the materials resulting in the electrical conductivity [8]. The optical transparency limit is set by the band gap of the material which should be  $\geq 3$  eV to ensure transparency throughout the visible spectrum. Additionally, there are secondary requirements like ageing, interfacial properties, chemical stability and band alignment matching which are vital for a high performance TCO. An intrinsic stoichiometric material is unable to ensure the simultaneous

occurrence of these properties. As a result of which, the only way in which a good transparent conductor can be obtained is by suitably doping a wide band gap ( $>3$  eV) thin film metal oxide [9].

Almost all the materials used as TCOs are n type semiconductors, implying that these materials are doped with excess electrons. However, p type TCOs have also been researched and investigated. A high performance p-type TCO could be used with a n-type TCO to form a p-n heterojunction. Also, with the growth of PV technology and solar water splitting, p-type electrodes would be required for efficient holes collection [10]. Such TCOs include  $\text{CuGaO}_2$ ,  $\text{CuAlO}_2$ ,  $\text{NiO}$  etc [11]. In addition to this, traditionally only crystalline materials have been used for TCO. However, since the 2000s there has also been a rise of amorphous TCO materials. Amorphous material fabrication results in homogenous films with very smooth surfaces at low temperatures. These qualities are particularly required for plastic substrates and flexible electronic applications [8].

### 1.3.1 Applicability

The simultaneous transmittance and conductance in a TCO ensures that they find their application in a wide variety of electronic, opto-electronic and mechanical applications. The two major applications of TCOs include display devices and thin film solar cells. Apart from these, TCOs are also used as mirrors for glass windows, incandescent bulbs, resistors, transistors, anti-reflection coating etc [9].

In a display device, the TCO layer allows for the electric signal to be conducted through it to each pixel. This results in the emission of light from each pixel which is transmitted out via the TCO. Meanwhile in a thin film solar cell, the main job of a TCO is to allow the penetration of light into the bulk of the solar cell. This light is then used to make electron hole pairs in the bulk which are collected at the front and rear transparent electrodes.

In Figure 4 below, applications of TCOs in different types of thin film solar cells is shown. Figure 4a) depicts a hydrogenated amorphous silicon solar cell with a front and rear transparent electrode. The function of the front TCO is to allow visible light to reach the bulk of the cell. The function of the rear transparent electrode is to transmit the residual light which is back reflected from the rear electrode and conduct the current. Figure 4b) depicts a CIGS solar cell with a n-type  $\text{ZnO:Al}$  as a front TCO. Figure 4c) depicts the application of TCO in a tandem cell configuration. In tandem solar cells, there are two main designs namely: two-terminal (2T) and four-terminal (4T). As it can be seen in the figure, since 2T design involves a monolithic fabrication meaning that the second sub cell is made on top of the front sub cell and connected by a tunnel junction or recombination layer. This results in only two external electrical contacts out of which only one is required to be a TCO to allow the light to enter the bulk. Meanwhile in a 4T design, both the cells are fabricated separately and are physically stacked on top of each other. This is why 4 individual contacts are required in this configuration out of which 3 must be semi-transparent to allow the light to enter both sub-cells.

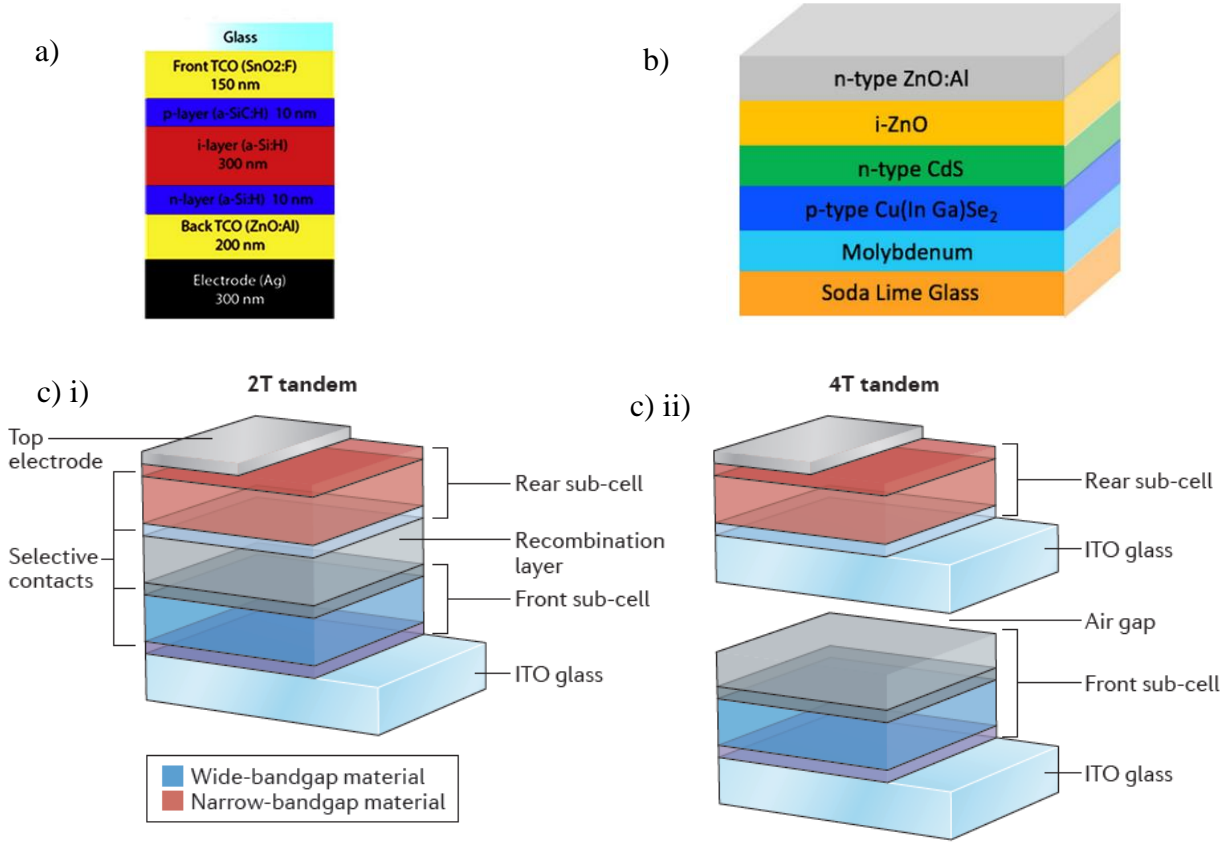


Figure 4 TCO in Solar Cell a) Amorphous silicon solar cell [12] b) CIGS solar cell [5] c) Tandem Solar Cell [13] i) 2 terminal ii) 4 terminal

A wide variety of deposition techniques like sputtering, pulsed layer deposition, atomic layer deposition have been used for the deposition of TCO. This is further discussed in detail in section 2.1.

### 1.3.2 Electrical conductivity

In this section, the primary characteristic of an electrode i.e its conductivity is introduced and elaborated. Herewith, the definition of electrical conductivity and the underlying principles and phenomena influencing the electrical conductivity of a TCO have been studied in detail. The main job of an electrode is to provide an unrestricted path for the electrons to flow through it, so that current could be easily extracted from it. This is ensured by maintaining low resistance or high conductivity in the electrode.

TCO being a transparent electrode needs to fulfil this criterion. The high conductivity of a n-type TCO like IO:H is a consequence of degenerate doping. A high level of doping in a semiconductor is referred as degeneration. This results in high carrier density ( $n_e$ ) in the material, which can be treated as a free electron gas. The required carrier density for degeneracy of a material is given by the Mott criteria [14].

$$n_{deg}^{\frac{1}{3}} a_0^* \cong 0.25 \quad (1.1)$$

Here,  $n_{deg}$  refers to the induced degeneration and  $a_0^*$  refers to the effective Bohr radius

$$a_0^* = \frac{h^2 \epsilon^M \epsilon_0}{\pi m_e^* e^2} \quad (1.2)$$

Where  $\epsilon^M$  is the static dielectric constant of the host lattice,  $\epsilon_0$  the vacuum permittivity,  $m_e^*$  the effective electron mass equivalent to  $0.35m_e$  and  $e$  the elementary charge. It has been reported by Hamberg et al. for  $In_2O_3$  that  $a_0^* \cong 1.3$  nm and degeneration occurs when  $n_e > 6 \times 10^{18} \text{ cm}^{-3}$  [15]. Since typically recorded carrier

densities of  $\text{In}_2\text{O}_3$  are in the range of  $10^{20} \text{ cm}^{-3}$  to  $10^{21} \text{ cm}^{-3}$ , it is considered degenerate. In order to define the conductivity of a material, it is important to understand the behavior of these free electrons in the material. Inside the free electron gas, the electrons diffuse and are accelerated by an external field ( $\vec{E}$ ). This effect is depicted in eqn. 1.3.

$$\vec{E} = \vec{e}_x E_0 \quad (1.3)$$

The movement of an electron in the field can be described by the equation of motion.

$$-e\vec{E} = m_e^* \frac{d^2x}{dt^2} + m_e^* \frac{dx}{dt} \quad (1.4)$$

Consider, the electrons are in a constant electric field. In such a scenario, there is no acceleration experienced by the electron. The electrons are scattered due to collisions. As a result of which, the drift velocity of the electron ( $\vec{v}_d$ ) can be defined as

$$\vec{v}_d = \frac{dx}{dt} = \frac{e\tau}{m_e^*} \vec{E} = \mu_e \vec{E} \quad (1.5)$$

Here,  $e$  is the constant electron charge equal to  $1.6 \times 10^{-19} \text{ C}$ ,  $\tau$  is the average time between collisions also referred to as the relaxation time,  $m_e^* = 0.35 m_e$  where  $m_e$  is the effective mass of the electrons and  $\mu_e$  is the electron mobility. Effective electron mass is defined as the mass an electron has when it is interacting with identical particles in a thermal distribution. Eq 1.5 assumes that after each scattering event, the carrier's motion is randomized as a result of which it has zero average velocity. Then it is accelerated uniformly in the electric field, until it scatters again. From eq 1.6, it can deduced that

$$\mu_e = \frac{e\tau}{m_e^*} \quad (1.6)$$

The current density ( $\vec{J}$ ) can be simply defined as the coming together of free electrons.

$$\vec{J} = -n_e e \vec{v}_d = -n_e e \mu_e \vec{E} = \sigma \vec{E} \quad (1.7)$$

Where  $\sigma$  is defined as the conductivity and  $n_e$  represents the charge carrier density.

$$\sigma = \frac{1}{\rho} = \frac{n e^2 \tau}{m_e^*} = n_e e \mu_e \quad (1.8)$$

The reciprocal of conductivity provides the resistivity. Both conductivity and resistivity are considered material properties. A commonly used term for investigating the electrical properties is called the sheet resistance ( $R_{SH}$ ). Resistivity and sheet resistance are related as follows:

$$R_{SH} = \frac{\rho}{d} \quad (1.9)$$

Here,  $d$  is considered the thickness of the film. Sheet resistance is a measure of resistance of thin films that are nominally uniform in thickness. Since, the films are uniform in thickness they are treated as two dimensional entities. As a result of which, it can be directly inferred from sheet resistance that the current is flowing parallel to the plane of the film. It is denoted by the unit 'ohms per square'. This is dimensionally equivalent to 'ohm' however it helps in avoiding misinterpretation as the bulk resistance.

Hence, it can be concluded that conductivity of the film can be improved by increasing the charge carrier density ( $n_e$ ) or electron mobility ( $\mu_e$ ). In addition to this, sheet resistance can be reduced by increasing the thickness of the film. As previously seen in Eq 1.6, mobility is dependent on the relaxation time  $\tau$ . So, greater

the average time between collisions greater the mobility. With increased scattering, the relaxation time decreases. Details of the scattering mechanisms are explained in the next section.

### 1.3.3 Scattering mechanisms

Low resistivities are obtained by either high mobility or high carrier concentrations as mentioned before. High carrier concentrations can be achieved by excessive doping however this can have adverse effects on the material properties. This can result in formation of scattering centers. In addition to this, it would also result in excessive free carriers resulting in greater absorption at longer wavelength due to free carrier absorption. This effect is further elaborated later in this section using the Drude model. In order to counter these effects, a lot of research is focussed on improving the mobility. The dominant scattering mechanisms in a material directly affect the mobility of a material.

The major scattering mechanisms reported for the materials are ionized impurity scattering, grain boundary scattering, neutral impurity scattering and phonon scattering. The detailed explanation of these dominant scattering mechanisms has been provided in the next section. However, there can be other sources of scattering as well. For instance, scattering due to surface roughness [16] or scattering at the interface of amorphous and crystalline phases [17]. The net electron mobility can be represented by the following equation.

$$\frac{1}{\mu_{net}} = \sum \frac{1}{\mu_i} \quad (1.10)$$

Here,  $\mu_{net}$  is the total electron mobility and  $\mu_i$  is the contribution of each scattering mechanism.

#### Ionized impurity scattering

A lot of ionized impurities such as oxygen vacancies, dopants etc are present in degenerate semiconductors (carrier density  $> 10^{19} \text{ cm}^{-3}$ ). These impurities act as scattering centers for electrons. As a result of which, as the charge carriers are increased, the scattering also increases. According to the Brooks-Herring-Dingle model, mobility due to ionised impurity scattering ( $\mu_{iip}$ ) can be given by the following equation [18]. This model assumes that the scattering centers are homogeneously distributed.

$$\mu_{iip} = \frac{3(\epsilon_0 \epsilon_r)^2 h^3 n_e}{Z^2 (m_e^*)^2 e^3 n_i} \frac{1}{F_i(\xi)} \quad (1.11)$$

Here  $\epsilon_0$  and  $\epsilon_r$  are the vacuum and static permittivity,  $h$  is the Planck's constant,  $Z$  and  $n_i$  are the charge and concentration of the impurity respectively.

$$F_i(\xi) = \ln(1 + \xi) - \frac{\xi}{1 + \xi} \quad (1.12)$$

$$\xi = (3\pi^2)^{\frac{1}{3}} \frac{\epsilon_0 \epsilon_r h^2 n_e^{\frac{1}{3}}}{m_e^* e^2} \quad (1.13)$$

#### Grain boundary scattering

Grain boundary can be defined as a 2-D interface between two crystallites. They act as a defect source in a material where charges can be trapped. This results in the formation of a potential barrier which obstructs the

flow of electrons in the material and hamper its mobility. This type of scattering becomes particularly vital, when the grain size is comparable to the mean free path [19]. The mean free path ( $\lambda_{mfp}$ ) can be given by the following equation [20].

$$\lambda_{mfp} = \frac{\hbar\mu_e}{e} (3\pi^2 n_e)^{\frac{1}{3}} \quad (1.14)$$

This equation holds true for  $n_e > 1-2 \times 10^{19} \text{ cm}^{-3}$  and shows the direct relation of the mean free path with the carrier concentration. The foundation of the mobility model depicting the influence by the grain boundary scattering was laid by Petritz et al [21] and further extended by Seto et al [22]. This model is shown below

$$\mu_{gbs} = \frac{eL}{\sqrt{2\pi m_e^* kT}} \exp\left(-\frac{E_b}{k_b T}\right) \quad (1.15)$$

Here,  $\mu_{gbs}$  is the mobility due to grain boundary scattering, L is the grain size, k the Boltzmann constant, T the temperature and  $E_b$  is the grain boundary potential or height of the potential barrier. In order to determine the influence of grain boundary scattering in the material, optical and hall mobility of the materials can be determined. The drude model providing the relation between the opto-electronic properties in a material can be used to determine the optical mobility. Optical mobility provides information related to the intragrain properties whereas hall mobility provides information on the intergrain properties. Hence, if the optical and hall mobility are equal it can be deduced that the influence of grain boundary scattering is negligible in the material. And if the value of hall mobility is smaller than the optical mobility, it can be deduced that there is grain boundary scattering in the material. However, for TCOs the influence of grain boundary scattering is found to be minute [23]. Still, this influence must be considered.

## Neutral impurity scattering

As the name suggests, neutral impurity scattering is the scattering caused by the inactive (neutral) dopant material. This kind of scattering is observed at very high doping concentrations ( $> 10^{21} \text{ cm}^{-3}$ ). Unlike the previously mentioned scattering mechanisms, neutral impurity scattering is not directly related to the carrier concentration. Instead, it depends directly on to the concentration of neutral impurities [19]. The contribution to mobility due to neutral impurity scattering is given by the following equation [24].

$$\mu_{nis} = \frac{m_e^* e^3}{20 \epsilon_0 \epsilon_r \hbar^3 n_N} \quad (1.16)$$

Here,  $\mu_{nis}$  is mobility due to neutral impurity scattering,  $\hbar = \frac{h}{2\pi}$  and  $n_N$  is the density of neutral scattering centers. This scattering mechanism are not expected to have much influence in TCOs.

## Phonon scattering

The mobility of the charge carriers in a material are also influenced by the vibrations in the lattice, which are augmented at higher temperatures. Above 0 K, atoms in a lattice vibrate, creating waves called phonons. The scattering caused by these waves is called as phonon or lattice vibration scattering. The contribution to mobility due to phonon scattering can be given by Eq 1.17 [20].

$$\mu_{ps} = \frac{2\sqrt{2\pi} \hbar^4 C_l}{2(m_e^*)^{\frac{5}{2}} E_d^2 (kT)^{\frac{3}{2}}} \quad (1.17)$$

Here,  $\mu_{ps}$  is mobility due to phonon scattering,  $C_l$  is the longitudinal elastic constant and  $E_d$  is the deformation potential constant in eV.

### 1.3.4 Optical properties

A primary requirement of TCO materials in a solar cell is its high optical transmission for photon energies greater than the bandgap of the absorber material used. For instance, for the commonly used polycrystalline Si the bandgap is 1.1 eV. This implies that the TCO should ensure high transmission for the spectral range of 1100 nm i.e. the visible and near infrared region. This requirement is tough to meet for many TCOs as there can be substantial absorption in the near infrared region due to excessive doping, which is done to improve the conductivity of the material as previously mentioned.

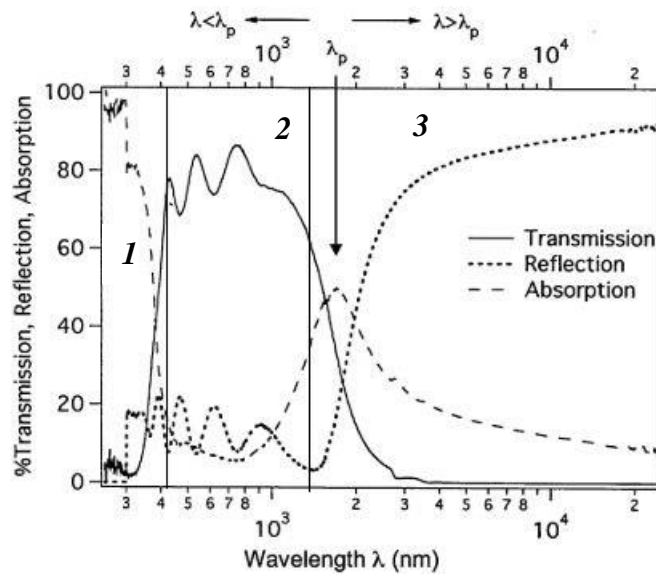


Figure 5 Transmittance, reflectance and absorption of a TCO,  
1) Absorption due to bandgap 2) Transmittance window 3) Free carrier absorption [8]

In Figure 5, transmittance, reflectance and absorption spectrum of a general TCO is shown. Area 1 of the figure depicts the region of the spectrum where the energy of the photon is greater than the bandgap of the material. As a result of which, this part of the spectrum is absorbed into the material. The bandgap of most TCOs is greater than 3 eV to ensure more part of the spectrum is transmitted through it. Area 2 of the spectrum depicts the transmittance window of a TCO. This area needs to be maximised into the near infrared region as much as possible in order to ensure higher transmittance of the spectrum. There is minimal parasitic absorption and reflection in this region. Hence, it can be considered the operational region of a TCO. Finally, Area 3 depicts the free carrier absorption region of the spectrum. Here,  $\lambda_p$  depicts the wavelength symbolic of the plasma frequency. As the plasma frequency increases, the transmittance window decreases and vice versa. The decreased transmission in this region is due to free carrier absorption (FCA).

Plasma frequency is given by Eqn. 1.18. This equation shows that the optical and the electronic behaviour of TCOs are closely related to each other.

$$\omega_p = \sqrt{\frac{e^2 n_e}{\epsilon_0 \epsilon_r m_e^*}} \quad (1.18)$$

It can be deduced from Eqn. 1.14 that as the charge carrier density is increased the plasma frequency also increases, which in turn results in a reduced transmittance window for the material. However, based on Eqn. 1.8 it can be seen that the conductivity of a material improves by increasing its carrier density. Hence, this counter effect of increased charge carriers on the optical properties of the material is countered by focussing on improving the mobility of the material.

In order to understand plasma frequency, consider an electrically neutral plasma in equilibrium. An electrically neutral plasma comprises of a gas with equal densities of positively charged ions and negatively charged electrons. If an electron or a group of electrons are displaced with respect to ions, they are pulled back by coulombic force. This is what happens when the electromagnetic radiation is incident on the material. If the thermal motion of the electrons is ignored, it can be shown that the charge density oscillates at the plasma frequency. This frequency represents the onset of free carrier absorption [25]

## Drude model

As previously mentioned, the decreased transmission towards higher wavelength is caused by free carrier absorption. This implies that the optical behaviour of a TCO is closely related to its electrical properties. This is described by the Drude model [26]. The susceptibility ( $\chi^{FC}$ ) accounting for the free carriers in the Drude model can be expressed by the equation below [27].

$$\chi^{FC} = -\frac{\omega_p^2}{\omega^2 + i\omega\omega_\tau} \quad (1.19)$$

Here,  $\omega_p$  refers to the plasma frequency and  $\omega_\tau$  refers to the damping term.  $\omega_\tau$  can be obtained from the relaxation time  $\tau$ . Both of these terms have been derived in Eqn 1.18 and Eqn 1.6 respectively. It can be deduced from these equations that  $\omega_p$  and  $\omega_\tau$  are dependent on the charge carriers and mobility respectively.

Due to this effect a TCO film which is transparent in the visible region, reflects light in the long wavelength region, with the plasma frequency defining the onset. The damping term defines the steepness in this transition. As the plasma frequency shifts to higher frequency due to increased carrier concentration, the optical prerequisite of a high transmission will limit the carrier concentration. On the other hand, both the plasma frequency and conductivity will benefit directly from high mobilities [27].

## Burstein-Moss shift

The doping of the metal oxide induces an electron degeneracy in the material as mentioned before, which can be explained by the Burstein-Moss shift. Electron degeneracy can be understood as a situation where the electron carrier concentration exceeds the conduction band density of states [28]. As shown in Figure 6a), in an intrinsic semi-conductor, the fermi level lies exactly in the center of conduction band and valence band. For a nominally doped semiconductor, the position of the fermi level shifts closer to the conduction band and valence band depending on the nature of doping. The example of n-doping is shown in Figure 6b) However, in the case of degenerate doping the fermi level shifts into the conduction band for n-type and into the valence band for p-type semiconductors respectively. This results in apparent increment or decrement in the band gap. The bandgap increases for a degenerately doped n-type semiconductor as the fermi level is present inside the conduction band. It can be understood by the fact that an electron from top of the valence band can only be excited to a level above the fermi level which is present inside the conduction band for a degenerate n-type semiconductor. This is the case with most TCOs as a big majority of TCOs are n-type. The difference of the conduction band minimum and the energy of the lowest empty states (position of the fermi level) that can be filled with electrons from the valence band is called the Burstein-Moss shift.

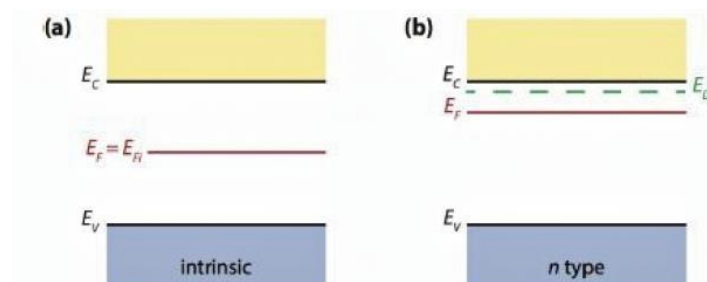


Figure 6 Doping [1]

This effect is shown for a generic n-type TCO in its band structure in Figure 7. In Figure 7,  $E_{g0}$  refers to the fundamental band gap which is the difference of the highest level of the valence band and the lowest level of the conduction band. This value should be greater than 3 eV to ensure the transmittance in the visible part of the spectrum.  $E_F - E_{VBM}$  refers to the apparent bandgap of the n-type semiconductor due to its degenerate nature.  $E_F$  refers to the fermi level which has been shifted to the conduction band and  $E_{VBM}$  refers to the valence band maximum. EA, WF,  $E_{CBM}$ ,  $I_P$  and  $E_{vac}$  denote electron affinity, work function, conductor band minimum, ionization potential and vacuum level respectively.

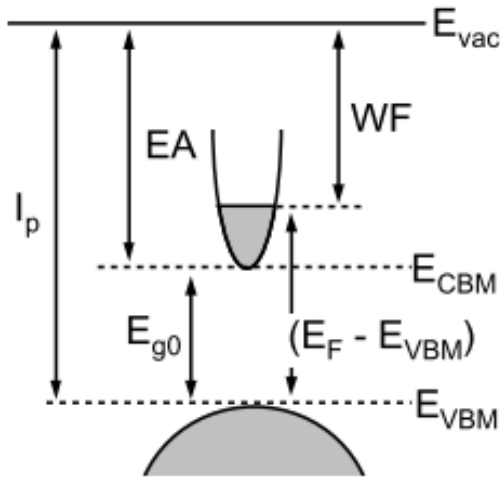


Figure 7 Burstein-Moss Shift [28]

#### 1.4. Indium Oxide ( $In_2O_3$ )

60 years ago, the oxidation of an Indium layer deposited by evaporation at high temperatures resulted in polycrystalline  $In_2O_3$  which was both conductive and transparent. Its conductivity particularly depended on the oxygen content in the environment [29].  $In_2O_3$  is a wide bandgap, n-type semiconductor. Its effective mass ( $m_e^*$ ) is found to be between  $0.35 m_e$  [15]. It has been known to have electron concentrations of  $10^{19} cm^{-3}$  due to non-parabolicity of the conduction band [30]. It is known to be less stable than other wide bandgap oxides like ZnO and  $Ga_2O_3$ . Its application as a TCO and as an active gas sensor material have been widely researched.

$In_2O_3$  mainly crystallises in a stable bixbyite structure with lattice parameter of  $a = 10.117 \text{ \AA}$  [31]. This is a body centered cubic structure which consists of 80 atoms. It is derived from a  $2 \times 2 \times 2$  (face centered cubic structure) fluorite structure out of which 25% of the oxygens are removed. As a result of which 8 Indium atoms occupy the positions marked by  $In_1$  and 32 Indium atoms occupy the positions marked by  $In_2$  as depicted in Figure 8. A metastable rhombohedral conundrum structure also exists which can be observed in Figure 8. The lattice parameter for this structure corresponds to  $a = 5.487 \text{ \AA}$  and  $c = 14.510 \text{ \AA}$ . This rhombohedral structure is rarely observed or is usually stabilized under growth conditions [32].

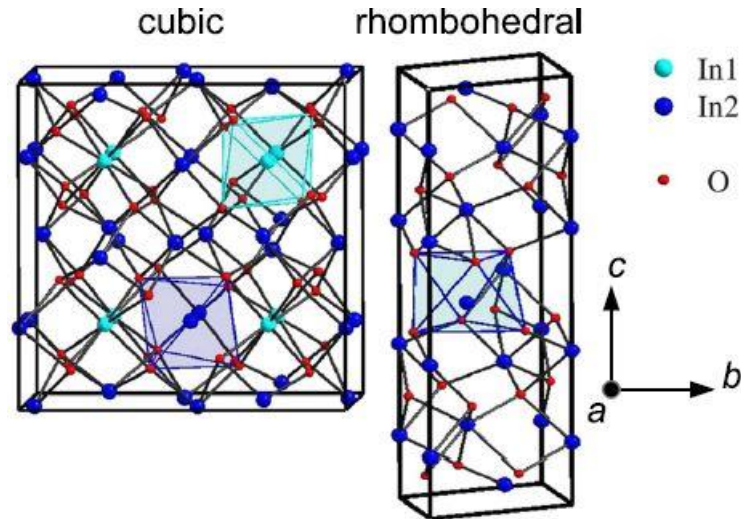


Figure 8 Crystal structure of BCC  $\text{In}_2\text{O}_3$ . Here  $\text{In}_1$  and  $\text{In}_2$  atoms are light blue and dark blue and O atoms are dark red [33].

$\text{In}_2\text{O}_3$  is transparent in the visible region with a strong optical absorption in the UV region. The fundamental bandgap of  $\text{In}_2\text{O}_3$  ranges between 2.6-2.9 eV and has been investigated very intensively [34, 35] because the optical measurements overestimated the bandgap to be  $\sim 3.8$  eV. It was revealed that electrical dipole between the valence and conduction bands at the  $\Gamma$  point are prohibited up to 0.8 eV below the valence band maximum. Hence, explaining the difference observed between the electrical and the optical bandgap. In this thesis, hydrogenated indium oxide (IO:H) a TCO based on  $\text{In}_2\text{O}_3$  with high mobility and excellent optical property is studied in detail.

## 1.5. Motivation

Solar energy as a primary source of energy is growing at a fast pace. The capacity trend depicted in Figure 2 is evident of this growth. However, to further boost the process the cost of PV systems need to decrease further. This can be done by increasing the efficiency of the solar cells, as this would have a direct influence on the overall economy of scale. TCOs as described in this chapter are an integral part of a thin film solar cell. The improvement of their electro-optical properties will have a direct influence on the efficiency of the solar cell. However, it is an intricate balance of electrical and optical characteristics in a TCO which result in its optimal functioning. This balance if disturbed could have detrimental effects on the properties of a TCO. This makes working on the TCO layer extremely intriguing and challenging.

The TCO chosen for this project is hydrogenated indium oxide (IO:H). IO:H is a high mobility material having high transmittance in the visible and near infrared region, due to reduced free carrier absorption in the near infrared region. The excellent electro-optical characteristics of IO:H are further discussed and compared in detail with other commonly used TCOs in the next section of the thesis. In addition to this, the PESALD process is used to perform the deposition of IO:H. This unique process offers several advantages over the other commonly used deposition techniques. This includes performing deposition at a lower temperature, causing less damage to the substrate due to ion bombardment and a scope of large scale application in the future due to its operability in atmospheric conditions. Additionally, the process ions generated during deposition have low temperature even though plasma is used in this process. It is also important to mention that in the current stack of the thin film solar cells developed by TNO, ALD has been already used for the deposition of buffer layers in the cell. Hence, investigating the possibility of adding a different types of layers so as a high performance TCO using the same type of atmospheric pressure operated and industrially scalable equipment is an additional motivation. Finally, after performing the necessary process development steps, a PV demonstrator of a CIGS solar cell using the TCO layer of IOH deposited by PESALD is made and evaluated for the first time. Overall, the combination of all the aforementioned factors provide the perfect drive for this research.

## 1.6. Objective

The main objective of this thesis is to develop a high performance layer of IO:H with optimum electro-optical characteristics using a unique PESALD process and further investigate its applicability on a thin film CIGS solar cell. In order to achieve these objectives the following research questions have been investigated and answered.

1. What are the process conditions required for successfully depositing IO:H using the PESALD process?
  - a. What is the apt precursor pickup flow?
  - b. What is the apt H<sub>2</sub> concentration in the plasma?
  - c. What is the apt substrate velocity?
  - d. What is the apt H<sub>2</sub>O concentration in the plasma?
  - e. What is the temperature range in which this deposition can take place?
2. How are the optical and structural properties of the IO:H layer influenced by the variable reactor temperature and H<sub>2</sub>O concentration in the plasma?
3. How is the reliability of the IO:H layer influenced by the variable reactor temperature and H<sub>2</sub>O concentration in the plasma?
4. How does the IO:H layer perform on a CIGS solar cell?

## 1.8. Thesis Outline

This thesis comprises of 6 chapters, aiming on the optimization of PESALD process to deposit IO:H and utilizing the results to implement it on a CIGS solar cell.

In Chapter 1, an introduction to the topic of transparent conductive oxides and its relevance to the field of solar energy is presented. The electrical, optical properties of the TCOs and their correlation to each other by proven scientific concepts are elaborated upon. This is followed by a brief section stating basic information about In<sub>2</sub>O<sub>3</sub> compound.

In Chapter 2, the literature study performed during the course of the thesis is presented. This includes information on the commonly used thin film deposition techniques, followed by a review on the different type of TCOs commonly used in the industry. This also includes information about IO:H which is the TCO of choice for this master thesis. Additionally, literature study based on the performance of the TCOs on CIGS solar cells and their ageing tendencies is also presented since these aspects of the TCO layers were investigated during this project.

Chapter 3 elaborates on the PESALD technique. It commences with description of the spatial and plasma enhanced ALD techniques. Then the components of the PESALD process, namely the metal precursor and plasma source are elaborated. Finally, common non-uniformities observed in the ALD process are also discussed.

Chapter 4 firstly provides an overview of the methodology used to perform the experiments and introduces the process parameters. This is followed by the presentation and discussion of the results obtained, focusing on the process development of PESALD for IO:H. Finally, some conclusions and recommendations based on these results are presented, which act as the foundation for the next chapter.

Chapter 5 focuses on the results and discussion of the CIGS solar cells obtained by using the most optimum conditions for TCO depositions obtained from chapter 4. Firstly, the conditions used for depositing the IO:H

are used to reproduce the results as per the requirement of the CIGS solar cells. Then the performance of the TCO on the cells is evaluated and discussed. Finally, conclusions and recommendations for future work are provided.

Finally, in Chapter 6, the results from the main takeaways from this research are summarized in order to briefly understand the current status of this research. Furthermore, some recommendations are made to for the future in order to further investigate and improve the performance of the TCO layers and hence, the corresponding solar cells.

# 2 Literature review

The theory for TCOs introduced in the previous chapter is put into use in this chapter. An insight into the world of TCOs and their deposition techniques, along with their applicability on a solar cell is provided. Firstly, the commonly used thin film deposition technique, sputtering is elaborated. It is accompanied by explaining the atomic layer deposition process since a special PESALD process is used in this project to perform the deposition of IO:H. This is followed by a review of the different TCOs like ITO, IZO, IO:Zr and IO:H and for some of the TCOs the results of their applicability on solar cells have also been documented. Finally, the effect of ageing on TCOs is also touched upon.

## 2.1. Thin film deposition techniques

Thin film deposition, as the name suggests is the method of applying a very thin film of material (typically in the range of a few nanometers to about 100 micrometers or even as small as the thickness of a few atoms) onto a substrate. These techniques have a wide range of application in the semiconductor industry, solar panels, CDs, disk drives and optical devices.

Thin film deposition is usually divided into two broad categories- physical vapour deposition (PVD) and chemical vapour deposition (CVD). PVD refers to a wide range of methods where a material is released from a source and deposited on a substrate using mechanical, electromechanical or thermodynamic processes. PVD comprises of methods like sputtering, evaporation, pulsed layer deposition etc. In PVD, a pure material source is turned into gaseous state using electricity, temperature etc and then it condenses onto the substrate, resulting in the desired layer. Meanwhile, CVD takes place when a chemical reaction takes place between two or more volatile fluid precursor on a substrate resulting in a chemically deposited coating. An impure material source is used in this process, which is first injected into the chamber, it then settles and decomposes onto the substrate, leaving the desired layer, while the byproducts are purged away. CVD comprises of methods like vapor phase epitaxy, metalorganic CVD (MOCVD), atomic layer epitaxy (ALE) etc. CVD is generally used to produce the highest purity and highest performance solid materials [36]. In this thesis, a modification of CVD namely atomic layer deposition has been used to perform the deposition of the TCO. In the next chapter, the atomic layer deposition technique used in this thesis are discussed in detail.

### 2.1.1 Sputtering

Sputtering is the most commonly used method for depositing TCOs. As previously mentioned, it is a type of PVD. There are different types of sputtering namely Radio frequency (RF) sputtering, direct current (DC) sputtering and reactive sputtering. The difference between these sputtering methods lies in the different sources that are used to generate power. RF sputtering is the commonly used method of sputtering and its major advantage as compared to other methods of sputtering is the reduced trap density in layers which results in better mobility [37].

During sputtering, the substrate to be coated and the target material to be deposited are placed in a vacuum chamber containing an inert gas. Moreover, a negative charge is applied to the target material which would result in the plasma glow during deposition. Negative target source material act as the cathode in this situation. As a result of which electrons flow in the vacuum chamber and collide with the inert gas atoms. The inert gas atoms become positively charged and collide with the negatively charged target material. These collisions result in the ejection of atomic sized particles from the target source. This results in the deposition of thin film on the surface of the substrate. This process is depicted in Figure 9.

Ion induced substrate damage poses a problem in sputtering. In order to curb this effect, a buffer layer is required to protect the layer. Additionally, it is difficult to maintain the uniformity of the layer. Sputtering is also quite expensive limiting its large scale application due to the need of maintaining a vacuum. PESALD process used in this project overcomes this limitation and hence, has been used for performing deposition for this project.

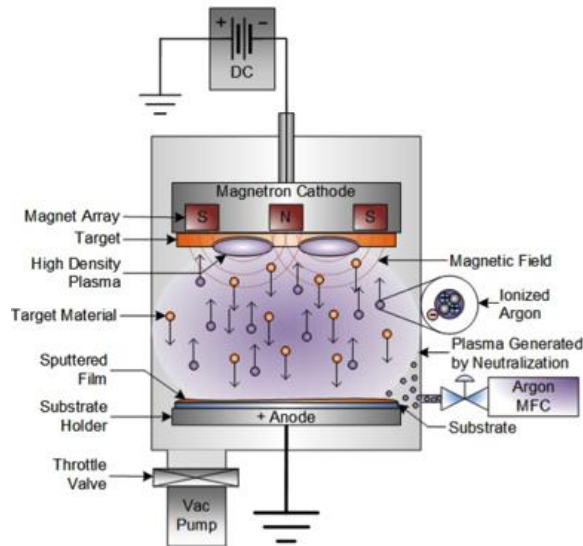


Figure 9 Sputtering process [38]

### 2.1.2 Atomic layer deposition (ALD)

ALD is a technique used for depositing thin films on substrates. It uses self-limiting reactions to deposit monolayers sequentially (layer-by-layer) on the substrate. ALD is considered a very precise and controllable process for creating thin films. In the commonly used chemical vapor deposition all the precursors and the byproducts are present in the same chamber at once, this makes it extremely difficult to control the deposition process at an atomic scale. This precision is achieved in atomic layer deposition by splitting the deposition process into half reactions. Each of the half reactions can be separately controlled. In a standard ALD process, first the substrate is exposed to the first precursor. This results in the reaction of the precursor with all the available reaction sites on the substrate. ALD is a self-limiting process, hence the reaction stops after all the reactive sites are filled. This is followed by purging to remove the excess precursor. Then, the second precursor is exposed and it reacts with the existing layer formed by the half reaction with the first precursor. Again, the excess precursor is purged and a monolayer is hence deposited. This process cycle is repeated to obtain the desired thickness of the film as shown Figure 10. The conformality of the deposited layers is considered one of the critical factor in choosing ALD over other deposition techniques like CVD or sputtering. In addition to this ALD also ensures tailoring of the layer thickness and more control over the composition. Although extremely precise, the ALD deposition rate is generally low as compared to the other deposition techniques.

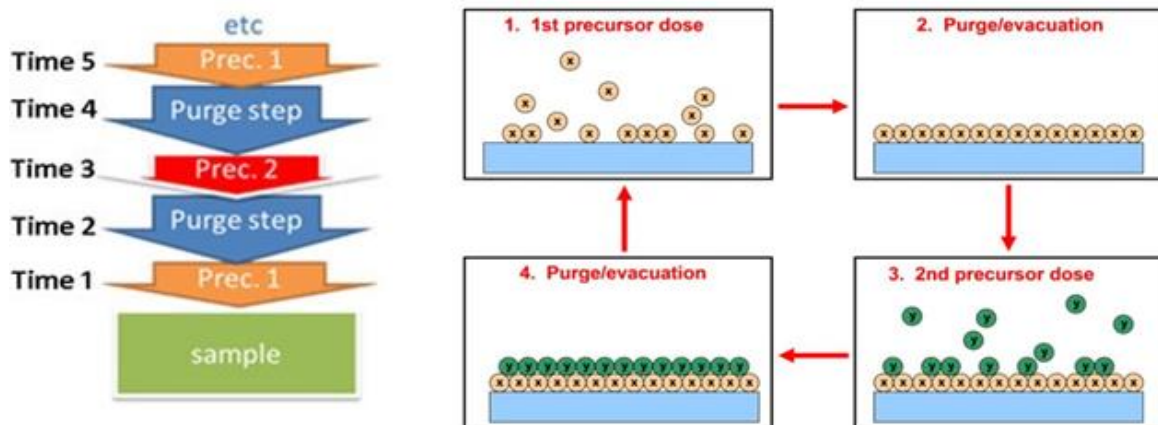


Figure 10 Temporal atomic layer deposition [39, 40]

## 2.2. Review of transparent conductive oxides

A summary of the available and popularly used transparent conductive oxides is provided in this section. Tin doped indium oxide, indium doped zinc oxide, zirconium doped indium oxide and hydrogen doped indium oxide are the materials reviewed in this section. The most interesting results for IO:H using sputtering and ALD are discussed. The electrical and optical properties are mainly investigated and reported applicability is further discussed.

### 2.2.1 Tin doped indium oxide (ITO)

ITO is widely used as a TCO, since low resistive films with high transparency in the visible wavelengths and large work function can be easily fabricated at low temperatures ( $\leq 200$  °C). High conductivity is obtained due to the activation of the Sn donors [41]. However, the mobility ( $\mu$ ) of a typical TCO is relatively low (30-40  $\text{cm}^2/\text{Vs}$ ) due to the presence of ionised impurities [37]. Due to the low mobility, there is an enhanced influence of free carrier absorption in near infrared region of the spectrum as discussed before in section 1.3.4. This is evident by its high carrier concentration ( $\sim 15 \times 10^{20} \text{ cm}^{-3}$ ) when subjected to annealing temperature  $> 150$  °C [42]. The high conductivity and transparency in the visible region for ITO can be attributed to its highly degenerate behaviour as a n-type semiconductor with a large band gap of around 3.5-4.3 eV [43]. However, it is also important to note that ITO exhibits decrease in conductivity and optical transparency with time and have a very poor chemical stability [44].

### 2.2.2 Indium doped zinc oxide (IZO)

Zinc oxide (ZnO) has a direct band gap of 3.27 eV and high chemical stability against reducing environment. It also possesses a textured surface and high work function (4.7-5.3 eV) with simultaneous occurrence of high transparency in the visible region and conductivity. In addition to this, it is relatively inexpensive, readily available and can be produced by a simple and scalable process [44]. However, it is known that undoped ZnO are unstable at high temperatures and can be improved by introducing impurities. Originally, pure ZnO has high resistivity. Doping of ZnO with In increases its conductivity since  $\text{Zn}^{2+}$  atoms are replaced by a higher valence  $\text{In}^{3+}$  atoms. Since Indium has one more electron than Zn, it acts as a donor impurity and creates a n-type semiconductor. It is interesting to note that IZO deposited as TCO is amorphous, which is the reason why it has a narrow bandgap [45]. Hence, amorphous IZO is considered a high mobility (60  $\text{cm}^2/\text{Vs}$ ) alternative with no requirement of an annealing step.

### 2.2.3 Zirconium doped indium oxide (IO:Zr)

IO:Zr is one of the most promising TCO materials. It is an ultratransparent and highly conductive material. The conductivity of the material can be attributed to its high doping and high mobility (100  $\text{cm}^2/\text{Vs}$ ). The primary sources of doping are the  $\text{Zr}^{4+}$  dopants and the oxygen deficiencies. The origin of high mobility in IO:Zr is attributed to the high crystalline quality of grains after annealing and to a similarity of size between  $\text{Zr}^{4+}$  and  $\text{In}^{3+}$  ions. The high transparency is attributed to the combination of high optical bandgap and low free carrier absorption in the near infrared region (NIR) [46]. It has also been suggested that the improved NIR transmittance originates from a modification of the permittivity of the material by adding  $\text{ZrO}_2$  [47]. Additionally, it is important to note that as compared to IO:H (other high mobility TCO) no water is used in the fabrication of IO:Zr, resulting in simplification of the process.

### 2.2.4 Hydrogen doped indium oxide (IO:H)

A high mobility material is very well suited for a TCO application as this allows both a high conductivity and high transparency as previously mentioned in section 1.3.4. Thin film  $\text{In}_2\text{O}_3$  layers have been doped with Mo, Ti, Zr and W [48], in order to obtain high mobility. However, these materials require high deposition temperatures making the process incompatible for certain temperature sensitive applications. This limitation is overcome by IO:H and hence it is the material of choice for this project. Koida et al. reported that amorphous IO:H with small crystallites were produced upon sputtering of  $\text{In}_2\text{O}_3$  at room temperature in the presence of

water. It is reported that H<sub>2</sub>O in the process improves the carrier density as hydrogen acts as the source of donors and results in an amorphous layer. Oxygen vacancies and hydrogen are considered the major donors in IO:H. This layer was then post annealed for 2 hours at low temperature ( $\leq 200$  °C) resulting in a high mobility (140 cm<sup>2</sup>/Vs) and low carrier density ( $1-2 \times 10^{20}$  cm<sup>-3</sup>) layer. The resistivity of the layer was found to be at par with a typical ITO film ( $\sim 0.29$  m $\Omega$ cm), additionally an improved transmittance in the near infrared region was observed due to the reduced carriers which can be observed in Figure 11b) [42]. The increase in mobility upon post annealing is attributed to the solid phase crystallisation. In IOH, the structure changes from amorphous to polycrystalline at 150 °C. This can be confirmed from Figure 11a) where the electrical properties namely mobility, carrier density and resistivity are plotted as a function of post deposition annealing temperature. It can be observed that mobility of IOH increases remarkably after 150 °C whereas the mobility for ITO remains almost the same. The carrier density of IOH on the other hand decreases for IOH due to improved mobility and resistivity remains similar to that of ITO.

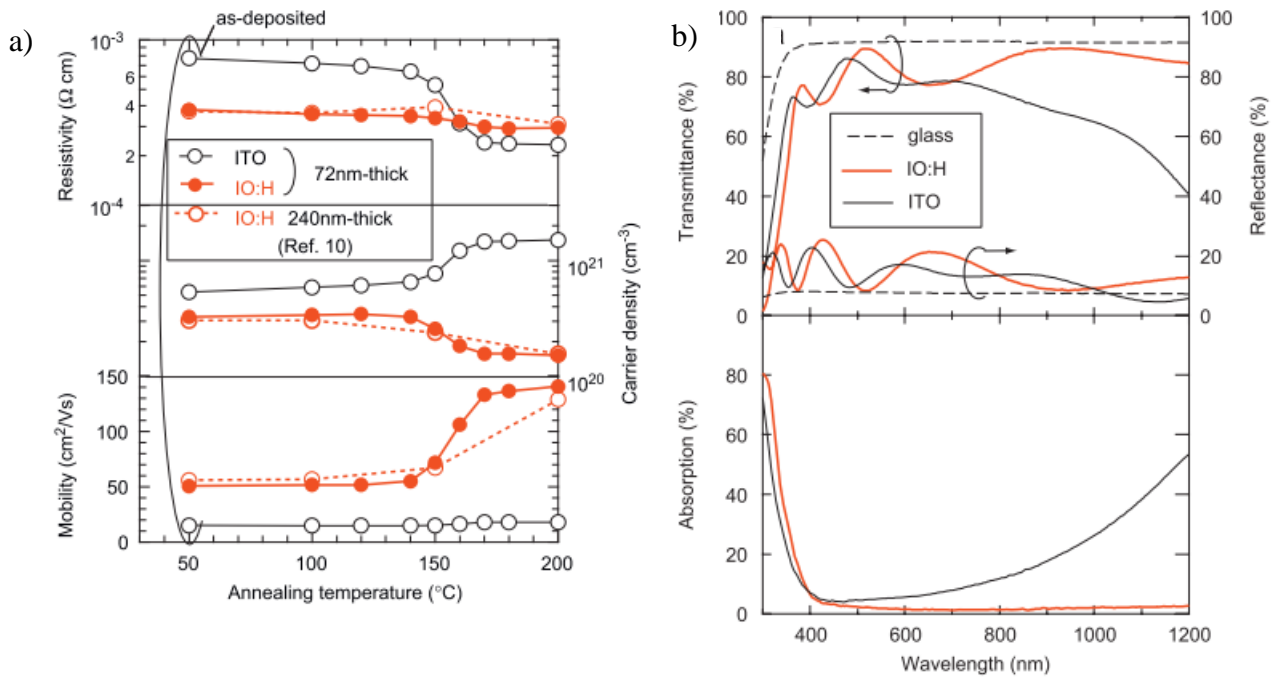


Figure 11a) Electrical properties of sputtered IOH compared with sputtered ITO upon post deposition annealing temperature [49] b) Optical Properties of sputtered IOH compared with sputtered ITO for annealing temperature of 200°C [49]

IOH has also been deposited, using ALD by Dr. B. Macco as part of his PhD work. Firstly amorphous IO:H was deposited using ALD which was later annealed to perform solid phase crystallization (SPC). Polycrystalline films with high mobility (140 cm<sup>2</sup>/Vs) and low resistivity (0.27 m $\Omega$ cm) were reported. It was found out that better opto electronic properties were observed for layer deposited at lower temperatures. Additionally, crystallization was observed to occur at a faster rate for high annealing temperatures but final grain properties were found to be independent of annealing temperature. It is interesting to note that the highest mobility for IO:H using this method was obtained at the lowest deposition temperature (100 °C) and annealing temperature had no effect on the mobility. Agreeing on Koida's hypothesis, increase in mobility is attributed to grain growth and crystallisation. Grain boundary scattering is found to be negligible in the grains. Overall, more pure and high quality grains are produced using ALD. It is also reported that <4% of H act as an active dopant in crystallized films [50]. The growth of the IO:H grain using this method can be observed in Appendix B.1. In the recent studies conducted by Husein et al, IOH is deposited by sputtering and it is observed that at high H concentrations, the grain size is reduced, causing the onset of grain boundary scattering and the decrease of ionised impurity scattering. The effect of grain boundary scattering becomes more prominent for 5% and 7% H in the layer [51, 52].

In addition to this, better opto electronic properties for IOH deposited by ALD as compared to sputtering are reported by Keller et al. The layers deposited by sputtering are annealed post deposition whereas the ALD layers are deposited at a temperature of 145 °C without any post deposition annealing. In sputter IOH layers, several micro/nano voids and cracks are present. ALD layers on the other hand are found to have larger and

more homogenous grains [53]. A compilation of the electrical properties for the aforementioned TCOs along with the techniques used to deposit them is done in Table 1.

Material	Mobility (cm <sup>2</sup> /Vs)	Carrier Density (1E20cm <sup>3</sup> )	Resistivity (mΩcm)	Deposition Technique
ITO	30	2	0.1	RF Sputtering[46, 54]
IZO	58	2.1	0.51	RF Sputtering [54]
IZO	10	7	0.872	ALD [55]
IO:Zr	100	2.5-3	0.25	RF Sputtering [54]
IO:Zr	76	2.2	0.37	ALD [56]
IOH	140	1-2	0.27	ALD [50]
IOH	110	1	0.5	RF Sputtering [54]

*Table 1 Comparison of TCO electrical properties*

## Donors

Donors or defects as its well known are the main contributors to the electronic properties in the semiconductors. The predominant defects in IO:H which contribute towards its conductivity are oxygen vacancies and hydrogen donors. Electronic properties of most oxides originate from oxygen vacancies. It can be understood that one oxygen vacancy would result in two free carriers, which would result in an increase in the carrier density and hence, the conductivity. They are considered common in metallic oxides. This is a consequence of non-stoichiometric nature of the oxides. Their concentration depends on the partial pressure of oxygen in the atmosphere. They are mainly caused by the crystal growth process, annealing or substitutions inside the crystal structure [57]. However, it can be understood that these oxygen vacancies also act as major scattering centers governed by the ionised impurity scattering mechanism explained in section 1.3.3. This complies well with the reported results in literature where post annealing has resulted in improved mobility and decreased carrier density due to reduced oxygen vacancies [42, 50]. The 0 and +2 donor states of oxygen vacancy contribute as a shallow donor in In<sub>2</sub>O<sub>3</sub> [58]. Although, commonly oxygen vacancies contribute as deep donors in metal oxides [59]. Deep donors mean that energy levels due to the oxygen vacancies are added deep in the bandgap [60]. Additionally, it is seen that oxygen concentrations result in improved transmittance in In<sub>2</sub>O<sub>3</sub> [61].

In addition to the oxygen vacancies, calculations by Limpijumrong et al. have shown that substitutional and interstitial hydrogen acting as shallow donors play a vital role in contributing to the conductivity of In<sub>2</sub>O<sub>3</sub>. A shallow donor means that the energy levels added in the material due to the hydrogen impurity do not add energy levels > 0.075 eV. As a result of which, the carrier concentration is increased due to hydrogen impurity [60]. Interstitial donors are one in which the proton forms an O-H bond with an already existing O atom and substitutional hydrogen are those where the proton occupies the oxygen vacancy. Out of the two, the substitutional hydrogen is much more stable [59]. Hydrogen can also exist as neutral H<sub>2</sub> molecule which do not adsorb the infrared (IR) part of the spectrum. Hydrogen not only contributes directly to n-type doping, it

also passivates dangling bonds and acceptor dopants. Since hydrogen is such a small atom, there is often hidden hydrogen found in metal oxides which further gets activated upon annealing [58].

### 2.3. TCOs on CIGS solar cell

A n-type conducting material with a high bandgap for high transparency is used as the front transparent contact in a CIGS solar cell. High lateral conduction is a desired attribute of this layer to transport the photogenerated charge carriers to the contacts. Apart from transparency and conductivity, moisture stability and compatibility are other important attributes based on which a TCO is chosen. Traditionally, aluminium doped zinc oxide (AZO) has been the material of choice as a TCO for CIGS solar cell. However, the presence of Al has known to result in increased moisture absorption in the film. This moisture exposure can have detrimental effects, resulting in increased resistivity of the TCO layer [38].

As previously mentioned, the CIGS cell architecture from Figure 4b) has been used in this project using IOH as a TCO. The performance of a similar CIGS cell using AZO, IZO and IOH deposited by sputtering have been investigated by Witte et al and the results are depicted in Figure 12 i). All the results are provided without an anti-reflection coating here. IOH seems to be performing at par with the reference AZO and IZO TCOs. However, it suffers due to the loss in fill factor probably due to the introduction of H<sub>2</sub>O during sputtering [45]. Furthermore, Keller et al. reported the performance of IOH deposited by sputtering and ALD on a CIGS solar cell. The results were compared with those obtained with a reference AZO. As it can be seen in Figure 12 ii) application of IOH has a distinct improvement on the short circuit current density ( $J_{sc}$ ) and open circuit voltage ( $V_{oc}$ ). Here PVD (physical vapor deposition) refers to the sputtered layer. The fill factor (F.F.) remains to be the limiting factor for IOH [53]. Fill factor losses are also attributed to the increased contact resistance between the front contact and the metallic grid [54]. Overall, these findings provide sufficient motivation to investigate the possibility of depositing a high performance TCO layer of IOH by using a unique plasma enhanced spatial ALD process.

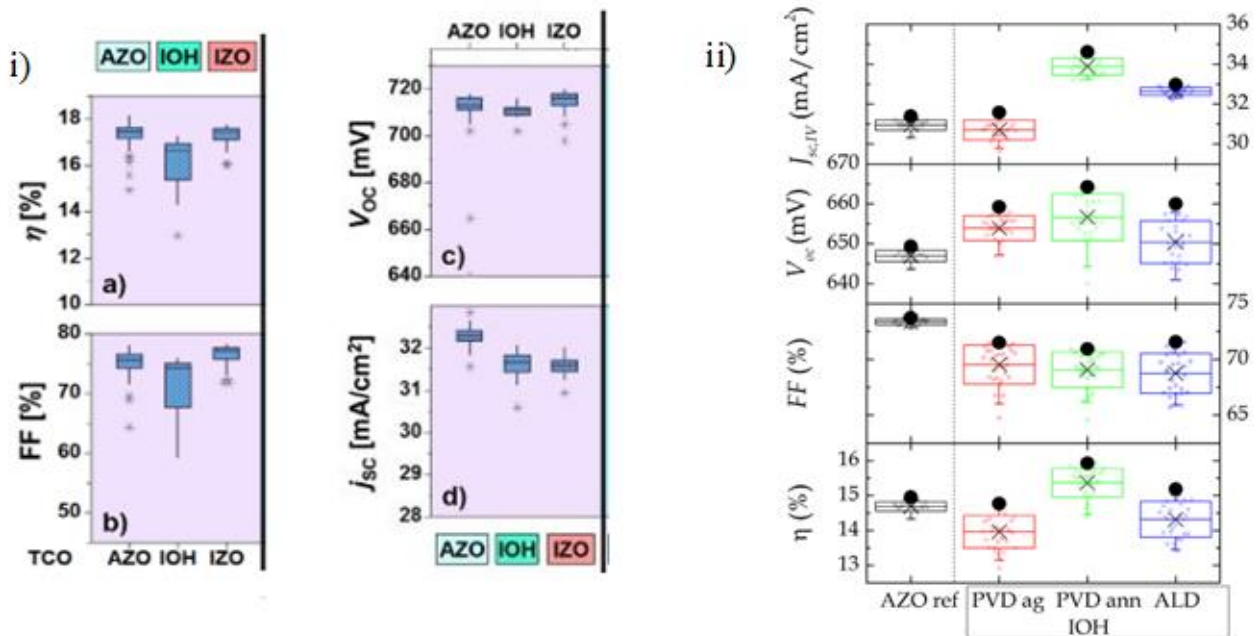


Figure 12 i) IV Characterisation of CIGS cell by Witte et al.[45] and ii) Keller et al.[53]. Here,  $J_{sc}$  is short circuit current density,  $V_{oc}$  is open circuit voltage, F.F. is the fill factor and  $\eta$  is the cell efficiency.

### 2.4. Ageing of TCOs

Application of TCOs on solar cells require them to have long term stability. Hence, it is essential to check the stability of these TCOs. Fast ageing of the electrode is simulated by placing them under damp heat conditions

(85 °C, 85% relative humidity). This investigation has been carried out by Tohsophon et al. for indium oxide based electrodes. ITO, IO:H and IZO are the materials that were studied. Based on this study, it has been shown that for ITO, IZO sheet resistance goes up by 3% and 13% respectively after 1000h of damp heat test. For IO:H on the other hand, sheet resistance degrades by 75%. It has been shown that this degradation is minimised by capping IO:H with a thin layer of ITO. The degradation comes down to 9% in this scenario. These results can be observed in

Figure 13 [54]. Degradation of IO:H is attributed to the removal of H at grain boundaries, which is responsible for the passivation of the layers. H is removed due to the chemisorption of OH groups to create H<sub>2</sub>O, increasing the potential barrier for electron transport.

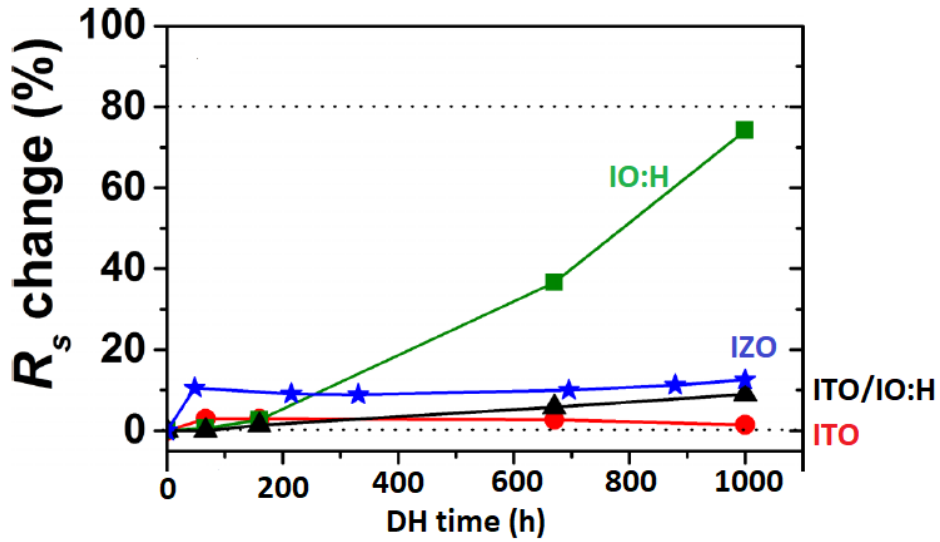


Figure 13 Change in electrical properties upon damp heat test [54]

# 3 Plasma enhanced spatial atomic layer deposition

In this chapter, the working of the unique plasma enhanced spatial atomic layer deposition technique developed at TNO is elaborated. Firstly the evolution of this technique from the aforementioned temporal ALD technique is explained. Then the two main components of the process, the metal precursor and the plasma are elaborated upon. This is followed by providing an insight into the non-uniformities observed in the ALD process.

## 3.1. Spatial atomic layer deposition (SALD)

Building on the background provided in section 2.1.2 about temporal ALD. An innovative advancement is made to this deposition process. In order to increase ALD deposition rates, obtain a high throughput and reduce the cost of ALD, a new method of spatially separating the half reactions has been devised. This is achieved by using a reactor head with separate gas flow channels, moving the substrate along those flow channels while continuously flowing chemical precursor gases to the substrate at various locations of the substrate. This results in simultaneous deposition of precursors on different regions of the substrate. Hence, simultaneously a half reaction takes place at two different regions of the substrate. Since the substrate is moving, after forming a saturated monolayer from one precursor it moves to the region where the second precursor is deposited hence completing the ALD cycle. Furthermore, the SALD setup at TNO operates at atmospheric pressure resulting in reduced cost of operation. It is important to note that constant purging keeps taking place throughout the deposition. This is essential to keep the two half reactions separate from each other as the mixing of the precursors in the gas phase would lead to undesired CVD and powder formation. A schematic of the SALD process along with a graphical representation of the substrate location can be seen in Figure 14. An important feature of SALD is the fact that precursors react with the substrate only in contrast with classical time-sequenced ALD where deposition occurs everywhere in the reactor. The absence of ‘parasitic deposition’ can be used to decrease chemical precursor consumption.

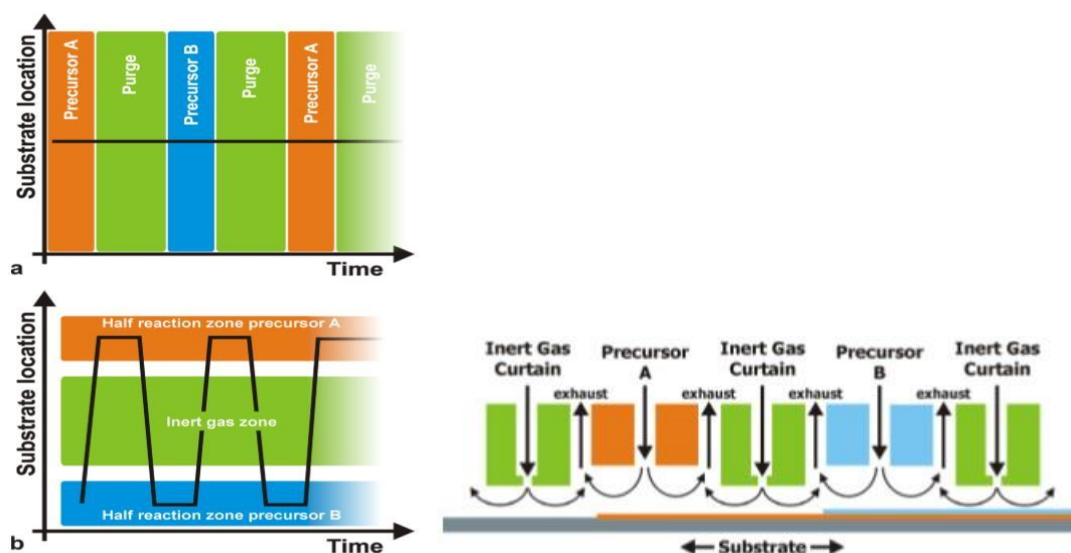


Figure 14 Spatial atomic layer deposition [40]

## 3.2. Plasma enhanced spatial atomic layer deposition (PESALD)

For the deposition of IO:H in this project, a plasma enhanced SALD setup has been used. The term plasma refers to the ionized state of a gas discharge created in an electric, magnetic or electromagnetic field. When

a plasma is applied in a molecular gas, not only ions but a variety of chemical reactive radicals is formed. Incorporating plasma in the SALD setup for depositing IO:H is particularly useful. Using plasma allows a wide variety of processing conditions and material properties. Past work at TNO-Solliance has shown that plasma enhanced ALD could improve the carrier density, impurity content and electronic properties of the deposited film. It allows low-temperature deposition on heat-sensitive substrates and leads to a wider choice in type of precursors as well. The presence of plasma in a gas changes its chemical reactivity. This would curb down the need of thermal energy for performing the deposition. Hence, same quality of deposition can be done at a lower substrate temperature. The schematic of a single cycle of PESALD process can be observed in Figure 15. Like most ALD, this is also based on a binary reaction sequence. Here, the first reaction involves the metal precursor step followed by the plasma step. It is essential to remember that such a surface limited thus high precision deposition is achieved at atmospheric pressure.

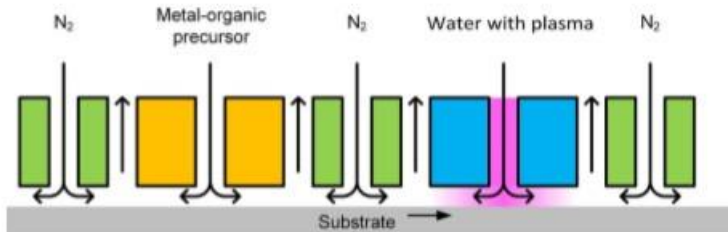


Figure 15 Schematic of PESALD process [40]

The PESALD setup used in this project can be observed in Figure 16. Figure 16 a) and b) refer to the top view and front view of the PESALD setup inside the oven. Figure 16 c) depicts the complete PESALD setup from outside the oven. The stationary reactor head with the injector slots for the metal precursor and plasma is clearly depicted in Figure 16a. It is assumed that the substrate is revolving at an angular velocity of  $\omega$  and  $w$  shows the length of the substrate exposed to the metal precursor at distance  $r$  from the center. Based on these parameters, the following relation for the exposure time ( $\tau$ ) is deduced.

$$\tau = \frac{w}{\omega r} \quad (3.1)$$

Since angular velocity  $\omega$  of the substrate is constant, it can be said that as the distance from the center  $r$  increases, the rotational speed of the substrate increases. So, in order to ensure a uniform deposition of the precursor it is essential that the length of the substrate exposed to the precursor also increases with an increase in  $r$  so that each part of the substrate has a constant exposure time. Hence, a pie shaped slot is used for depositing the metal precursor. The plasma slot is equipped with a linear remote plasma source, thus the flow of radicals (number of radicals per second per  $\text{cm}^2$ ) is constant as a function of radius. Since the plasma radicals react with each other in the gas phase (radical recombination loss) and not only with the substrate, most of the radicals do not reach the exhaust channel. Figure 16 b) clearly depicts the components of the setup. The gas bearing present in between the metal precursor and plasma slot plays a vital role in separating the two half reactions during the deposition process. Figure 16 c) is a photograph of the PESALD setup depicting the setup from outside the oven, connected to a plasma power source, oven temperature regulator, substrate controller and oscilloscope. A vacuum chuck is used to fix the substrate on to the holder before moving the substrate extremely close to the reactor head. Free rotation of the substrate is manually controlled before commencing the motor-driven rotary movement.

The ALD process is studied with growth experiments which means that the layers are deposited on bare substrates and investigated afterwards ex situ. Growth studies can be used to investigate the influence of various process conditions such as temperature. However, the byproducts obtained as a result of layer decomposition can only be assumed by these growth experiments. One way by which layer decomposition could be observed is by the etching phenomenon, for instance. In this project, IO:H was deposited by using binary step (metal precursor + plasma) process in the ALD cycle. Depositions were performed using an Indium precursor called 3-(dimethylamino) propyl dimethyl indium (DADI). Plasma was produced in a gas mixture of  $\text{H}_2$ - $\text{N}_2$ - $\text{H}_2\text{O}$ . In addition to this, parameters such as speed of the substrate, temperature of the reactor, plasma power, flow of water,  $\text{H}_2$ , and precursor were altered. A controlled evaporation mixing (CEM) system was used to mix water with the carrier gas while performing depositions. CEM allows the user to mix a defined

quantity of liquid with the carrier gas. This is particularly useful in deciding the optimum amount of water flow required to obtain the IO:H layer with good electrical and optical properties.

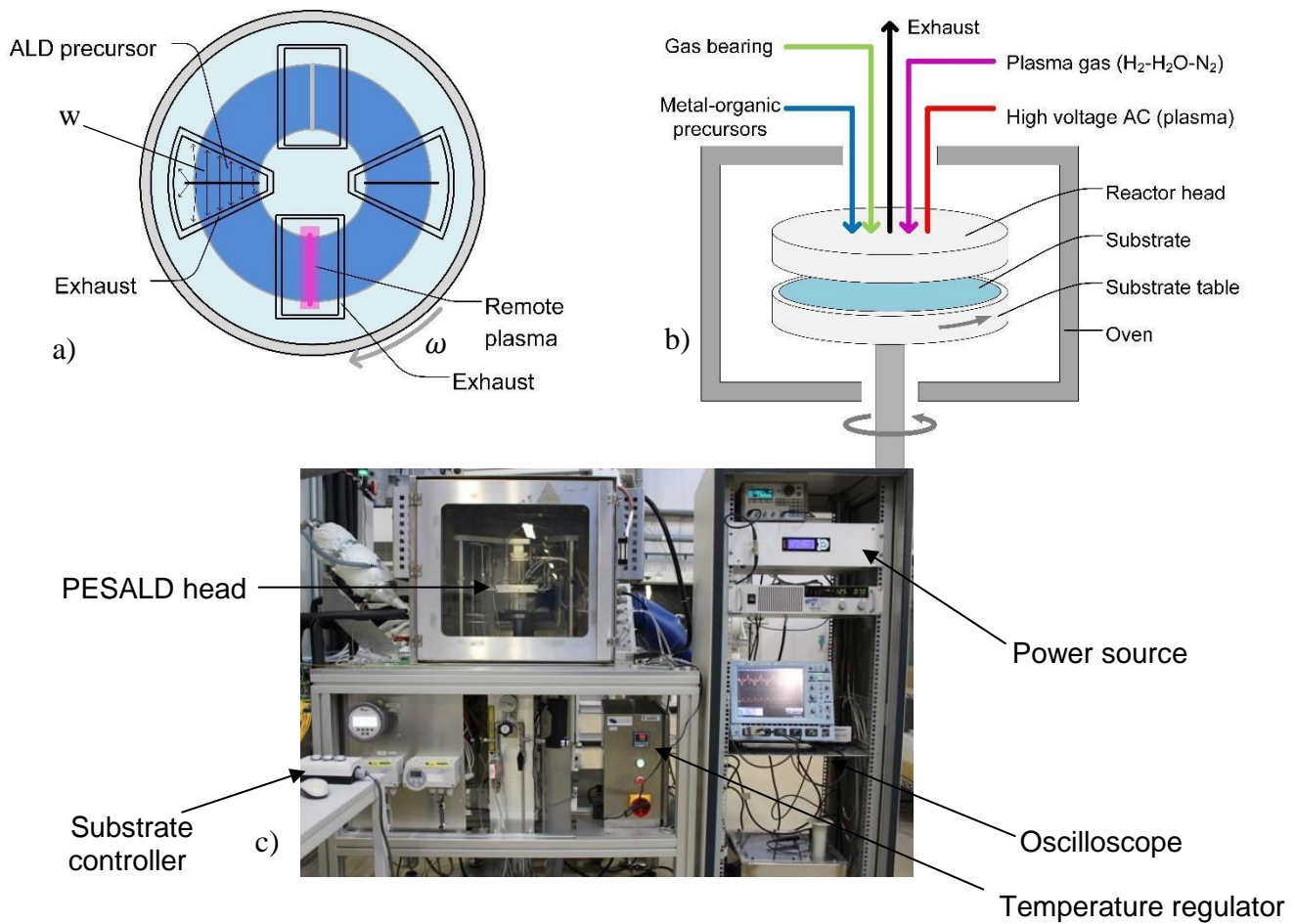


Figure 16 a) PESALD Top View b) PESALD Front View c) Real time picture of PESALD Setup

### 3.3 Metal Precursor

The metal precursor is one of the two key ingredients used for the deposition in this PESALD process. For a precursor to be compatible for the ALD process, it needs to adhere to three basic properties. Firstly, It must have enough vapor pressure to be transported to the substrate surface. Secondly, it should undergo decomposition at an acceptable temperature, ensuring that no decomposition takes place in the gas phase before the completion of the surface reaction. And finally, It should not react in the gas phase. The metallic component of the material deposited is obtained from the metal precursor. Solid and liquid precursors are commonly used as metal precursors. Liquid precursors can be drawn by vapor drawing, bubbling or by direct liquid injection. Solid precursors in general have certain disadvantages. They often require higher temperatures than liquid to achieve the desired vapor pressure. Solid precursors can also undergo decomposition. The precursor chosen for deposition directly influences the growth rate of the process and the quality of the layer deposited [36]. In addition to this, there are often instabilities in vapor delivery observed which act as a bottleneck of solid phase precursor materials.

For the deposition of indium oxide using ALD, solid In precursors have been used in the past which showed relatively low vapor pressure and poor reproducibility [62, 63]. Additionally liquid precursors such as  $\text{InCl}_3$ , indium acetylacetonate [ $\text{In}(\text{acac})_3$ ] and trimethylindium (TMI) have been previously used in literature. These precursors require relatively high deposition temperatures, result in slow ALD growth rates [64] and high electrical resistivity[63]. Faster growth rates were obtained for cyclopentadienylium ( $\text{InCp}$ ) but the deposition temperature still remained high (200-300 °C) [65]. However, recently it has been shown in the work

of B. Macco that conductive films can be deposited at low temperature (100 °C) using InCp, but the films required a simultaneous injection of H<sub>2</sub>O and O<sub>2</sub> and a high temperature post annealing step to obtain the desired opto-electronic properties [50]. In addition to this, InCp is a very expensive metal precursor (\$366 per gram, Strem Chemical Inc.) as compared to TMI (\$62 per gram, Strem Chemical Inc.) . Hence, it is vital to choose a liquid precursor that requires low deposition temperatures while permitting fast growth rates and good opto-electronic properties of the film at an economical price.

The growth of materials deposited by ALD processes are characterized by using growth per cycle (GPC). This can be understood as the ratio of the thickness of the layer to the number of cycles made to reach that thickness. It is important to note that GPC is not a measure of the chemical kinetics, rather it is dependent on the available chemisorption sites, surface morphology and the reactivity of the surface. For this project, dimethylamino-kN)propyl-kC] dimethyl-Indium (DADI) precursor has been used. DADI is known to be less reactive with oxygen and water as compared to other commonly used Indium precursor like TMI. This is particularly useful for the PESALD system used here for deposition since it operates at atmospheric conditions. It is a liquid precursor and it has high vapor pressure at room temperature, hence resulting in reduced chance of contaminating the system. This makes it more suitable for upscaled applications and plasma processes. Thermogravimetric analysis of DADI, where the mass of DADI is measured over time as the temperature changes reveals that a rapid mass reduction of DADI occurs around 70 °C, which is most likely a consequence of vaporisation. Additionally, a low amount of non volatile residue has been reported. The differential scanning calorimetry of DADI in which the difference in the amount of heat required to increase the temperature is measured reveals that heat flow remains almost constant above 50 °C and a sharp drop occurs near 350 °C, depicting decomposition of the precursor. These effects can be observed in Figure 17 below. DADI precursor is known to saturate at the GPC of 0.06 nm/cycle. It has been reported by Maeng et al. that the resistivity of In<sub>2</sub>O<sub>3</sub> thin film deposited by ALD of DADI and ozone decrease as the deposition temperature is increased from 100-250 °C. Low carrier density ( $\sim 10^{18}$  cm<sup>-3</sup>) have been reported for the layers grown at 100°C, in agreement with the high resistivity obtained. The mobility of the layer also remains low (10 cm<sup>2</sup>/Vs) at low temperature and increases at higher temperatures (50 cm<sup>2</sup>/Vs) using DADI [66].

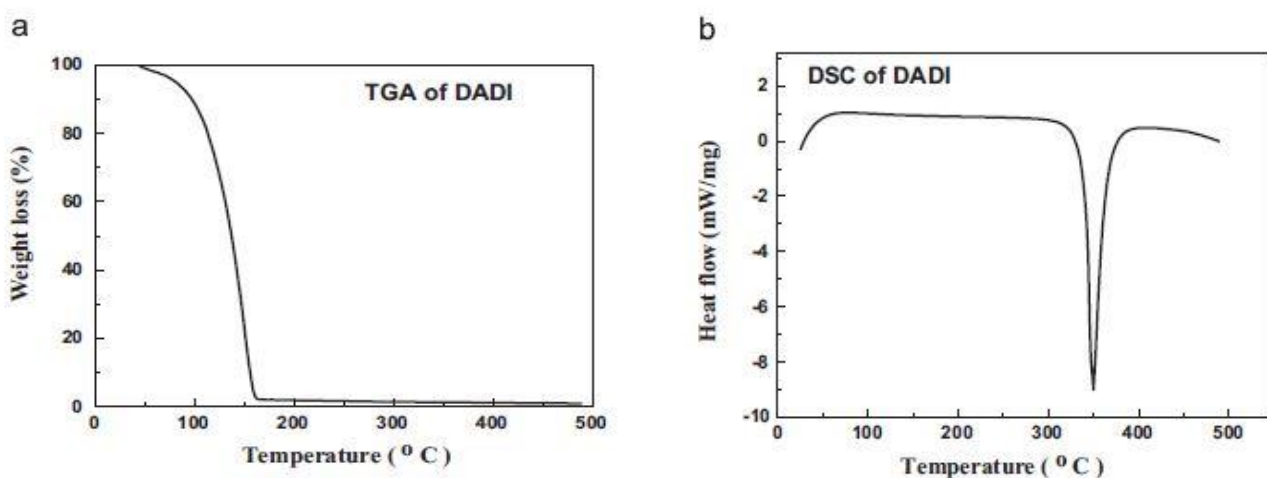


Figure 17 TGA and DSC of DADI [66].

During the metal precursor step, it can be firstly assumed that the glass surface is fully terminated with OH clusters. Then when the surface is exposed by the DADI precursor, it should ideally react with the available OH clusters to form the In-O bonds with the release of methane (CH<sub>4</sub>). Following the basic principle of an ALD self limiting precursor step, all the available OH clusters on the glass should now be replaced by the methyl clusters, resulting in no more available sites for surface reaction due to DADI. This is then followed by the plasma step.

A disadvantage of DADI is the low GPC observed, this could be attributed to the phenomenon of steric hindrance in ALD surface reactions. This could be due to the larger molecular size of DADI as compared to other precursor like TMI, for example. More details on steric hindrance can be found in section 3.5.

## 3.4 Plasma

A brief introduction to the plasma step was provided in the beginning of section 3.2. Plasma can be understood as the ionized state of matter. It tends to exist when a material in its gas phase is energized to the limit where the electrons are not associated with the atomic nucleus, however they show collective behaviour due to the long range coulombic force. Based on this definition, in order for a state of matter to be qualified as plasma it needs to meet the following criterion [67].

1. The medium should be electrically neutral (quasineutral).
2. The medium must show collective behaviour.

As, it was mentioned before the deposition takes place at atmospheric pressure (AP). Hence, it was essential to use a plasma source that would be compatible to such high pressure. There are three possible geometries which can be chosen. The plasma source can either be a corona discharge, direct plasma or a remote plasma source. Electrode geometries for low pressure direct and remote are depicted in Figure 18.

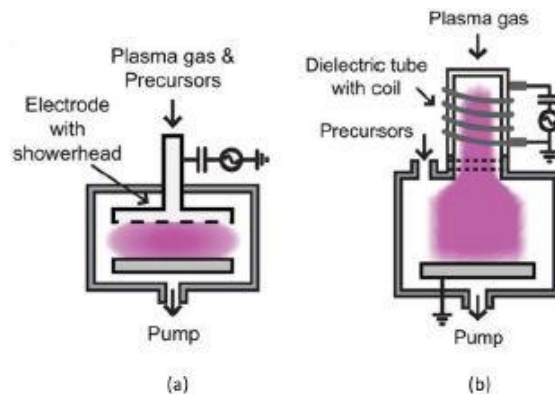


Figure 18 a) Direct plasma source b) Remote plasma source [68]

A direct plasma source is one in which the reactive species which form the core of the plasma are made directly above the substrate. Meanwhile, for the remote plasma these reactive species are formed somewhere else and then transported on to the substrate. The remote approach is the one that has been utilised for the plasma sources in the PESALD reactor of TNO Solliance. Since, the deposition is performed at such high pressure it is essential to have a tighter control over the plasma parameters which would be tough to achieve by using a direct plasma source [69]. The high pressure operation poses another difficulty which needs to be overcome by the plasma source. At AP and room temperature ( $\sim 300$  K) conditions,  $2.3 \times 10^{19} \text{ cm}^{-3}$  atoms/molecules are present. This high density of molecules results in high tendency of collisions usually in the range of  $10^{10}$ - $10^{12}$  Hz. As a result of which, the gas used for creating the reactive species in the plasma are heated and the plasma temperature is increased. This is undesirable for the plasma operation in PESALD. This gas heating is avoided by pulsing the excitation of the plasma gas at a low excitation frequency ( $\ll 1$  MHz) which in turn limits the duration of the plasma discharge. In the following section, a brief introduction is provided to the commonly used AP plasma sources and the choice of plasma source along with the reason for the low aforementioned excitation frequency used for the PESALD process is explained.

### 3.4.1 Atmospheric plasma sources

The breakdown of a gas between electrodes at a distance follow Paschen's law. This theory does not hold true for atmospheric pressure plasma, however surprisingly similar trends are observed. Theory of the Paschen's law can be found in Appendix B.2. An everyday technology based on atmospheric plasma systems is the electric arc welding. However, this is an example of a thermal plasma. In thermal plasma sources more than 80% of the applied power can be transferred into heat. In such arcs temperatures can go to as high as  $10,000$  °C. As previously mentioned such high temperature plasma is not suitable for deposition. As a result of which, cold "non equilibrium" plasma is required. Here, the main energy carriers are electrons and the rest

of the nucleus remains cold. Understandably, a higher breakdown voltage is required for generating AP plasma discharge [70].

Overall, the atmospheric plasmas can be classified with respect to their excitation frequencies as following. This is depicted in Figure 19.

- DC (direct current) and low frequency discharges.
- Radio frequency waves plasma
- Microwave discharges

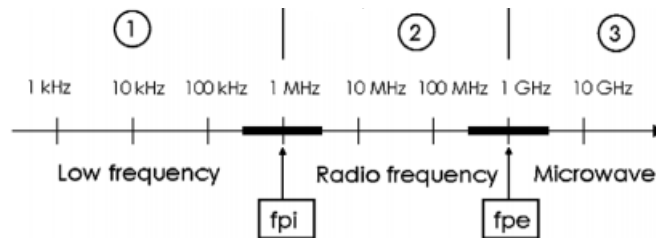


Figure 19 Atmospheric (cold) plasma classification based on excitation frequency [71]

It is to be noted that in this project,  $N_2$  is the carrier gas used for deposition in the plasma comprising of ~37%  $H_2$  and ~9%  $H_2O$ . For stable and homogenous plasmas in  $N_2$ , frequencies are limited to 50-200kHz [69]. And hence a low frequency discharge type plasma with a pulsed power supply to regulate the plasma temperature is incorporated for the plasma source used in the PESALD reactor. A commonly observed atmospheric pressure plasma discharge which follows this principle is the corona discharge. This kind of discharge is commonly observed due to the ionization of fluid such as air surrounding a conductor. The drawback of this AP plasma source is that the micro arcs generated cause non homogenous treatment of the material surface. In order to overcome this disadvantage, a surface dielectric barrier discharge is developed. This is the type of plasma source used in the PESALD reactor [72].

### 3.4.2 Dielectric barrier discharge (DBD)

As it can be seen in Figure 20, the DBD device consists of two plane parallel electrodes out of which either one or both the electrodes are covered by an insulator (dielectric). The plasma gas flows in the gap between the electrodes. The gap is set at a few millimeters. In order to transport current through the gas gap, the electric field needs to be higher than the breakdown level of the gas. This results in a large amount of micro-discharges. Micro-discharge is a term often practised to describe filamentary structured DBD plasma. Micro-discharges comprise the different time-phases of discharge development: initial streamer development, local surface discharge development on the dielectric barrier and charge saturation. The order in which these discharge phases are observed is the same for different configurations of DBD plasma, however the magnitude of occurrence varies from one configuration to another. These configurations are elaborated later in this section. For further clarification, a streamer can be understood as a dense and mobile structure which exits as a result of a distortion in a field [73].

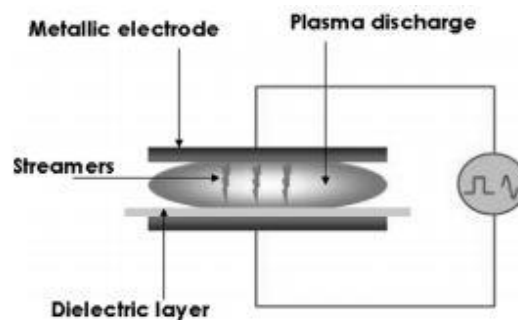


Figure 20 Schematic of a DBD setup [68]

The identical phases obtained in all DBD configurations are enlisted in the work of Gibalov. et al. as the following [73].

1. Townsend or pre breakdown phase: This is the first phase and it is indicative of the breakdown of the plasma gas. The overall field strength in the discharge region remains unaltered during this phase. Increase in the number of electrons is observed which arise from previous discharge processes or by natural sources. These electrons provide the necessary trigger for the first avalanches. Further electron multiplication, results in the electron reaching the critical value by the Raether-Meek criterion and the streamer phase is reached.
2. Streamer phase: The discharge dynamics during the streamer phase result in the microdischarge channels. Depending on the dynamics, it might result in either a constricted non homogenous (filamentary) or a more broad homogenous discharge. The streamer could either be cathode directed or anode directed.
3. Decay phase: The last phase is indicative of the loss or decay of discharge which is purely dependent on the movement of the ions.

It is vital to mention here that unless explicitly mentioned, a discussion about streamers and their corresponding channels comprise of both filamentary as well as homogenous DBD [73]. A homogenous treatment of the surface is observed for the DBD plasma source used at TNO. In the DBD plasma source used at TNO, ceramic is used as an insulating material (dielectric barrier). The plasma developed by using these sources is completely remote and has been observed not to cross over to the substrate. Remote nature of the plasma ensures that the transport of radicals is flow dominated. In the case of direct DBD, the transport of radicals is dominated by diffusion phenomenon.

As mentioned initially in the section, three possible configurations for DBD plasma are the following [67].

1. Figure 21 a) depicts the volume discharge configuration is the one where discharge exists in the gas volume between the electrodes.
2. Figure 21 b) depicts the surface discharge configuration, here the discharge is directly formed on the dielectric surface without travelling through a gas volume.
3. Figure 21 c) depicts coplanar discharge configuration, in this case several pairs of electrodes are inserted into the dielectric in the same plane, resulting in discharge on the surface of the dielectric.

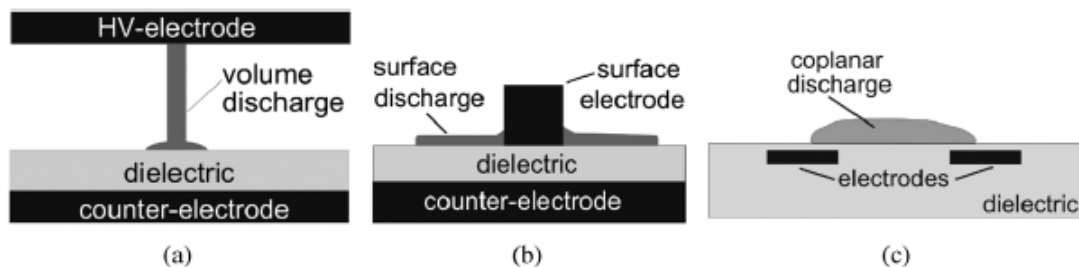


Figure 21 Configurations of a DBD plasma. a) Volume discharge b) Surface discharge c) Coplanar discharge [73]

The DBD plasma sources from TNO used in this project are unique, since they have certain combined characteristics of the aforementioned DBD plasma configurations as mentioned below.

1. Volume discharge generation is observed in very small gaps.
2. In these sources, surface discharge is eventually obtained from the volume discharges.
3. The geometry of the plasma sources is optimised for plasma generation as close as possible to the substrate without being transferred to the surface, when the surface is conductive. This is essential to keep the conductivity of the surface intact.

A detailed description of the plasma source used in this project is provided in the next section.

### 3.4.3 Plasma source

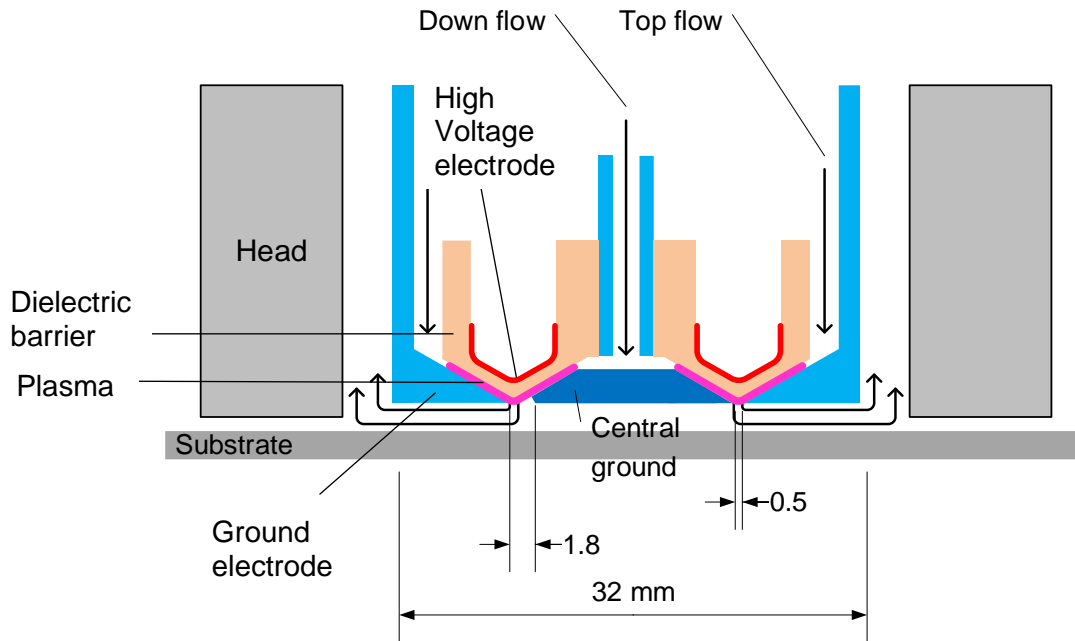


Figure 22 Schematic of plasma source R3.6 and R3.2

Figure 22 depicts the cross section of two plasma sources R3.6 and R3.2 along with their dimensions. The same housing and dielectric barrier is used for both these sources. The remote plasma is created here between the wedge shaped ground electrodes and dielectric barrier. The distance between the dielectric barrier surface and the substrate is between  $\sim 0.17$ - $0.2$  mm, depending on the barrier gas pressure. Moreover, the gap between the dielectric barrier and ground electrode is  $0.1$  mm. These sources consist of three ground electrodes, one central ground electrode and the two identical ground electrodes on either side of the central ground electrode and two plasma gas outlet slits. In addition to this, the right and left side of the plasma sources are basically mirror images of one another. The only difference between the two sources is in the central ground as it can be observed in Figure 22. For R3.2 the central ground provides a gas slit width of  $0.5$  mm as shown on the right side in Figure 22 and for R3.6 the central ground provides a gas slit width of  $1.8$  mm as shown on the left side in Figure 22. R3.6 is the plasma source used during this project. It is important to note that due to a damage incurred in the right slit of the source, only the left slit was operational during this project. The slit width of  $1.8$  mm is used in this source to increase the treatment area of the substrate. The width is not increased uniformly on both sides, rather it has been increased in the shape of a triangle. This non uniform increase in slit width is the primary reason why a radial dependence in layer growth and electrical properties has been observed for the deposited samples as discussed in section 4.5. This happens because a flow along the length of the plasma slit is induced due to this triangular shape, however this has resulted in improved conductivity for the TCO deposited.

Moreover, the remote plasma is transported on to the substrate by using two flow channels which are named as down flow and top flow. Between these two, down flow is the one which is directly in contact with the substrate surface whereas top flow as the name suggests results in a flow on top of the down flow. The role of the top flow is to push the radical flux of the down flow on to the substrate. Previous experiments performed at TNO have shown that the top flow indeed does not mix with the down flow. It is important to note that the dimensions shown in Figure 22 are not upto scale. The width of the exhaust channel and the distance between the head and the substrate are particularly underestimated in the image.

### 3.5 ALD temperature window and non- uniformities

ALD is a chemical technique and hence it is difficult to achieve pure, saturated growth using it. The main essence of an ALD process lies in its self limiting nature as was mentioned before in section 2.1.2. However, this is an ideal case scenario which does not hold true for all ALD systems. The reaction pathways which

result in self limiting growth by ALD are very limited as there are very few precursors which facilitate such growth. Also, a non uniform distribution of the precursor in the carrier gas could also influence the uniformity of the layer deposited. Additionally, it is also essential to ensure rapid pulsing of precursors, and their uniform gas distribution followed by an effective purge step[74].  $Al_2O_3$  is one of the rare materials which shows an ideal ALD model [75].

There are several qualities that a reactant must meet in order to develop an ALD process through it. A precursor should be volatile and turn gaseous without applying much heat. The composition of the precursor should remain intact in the gaseous phase until it reacts on to the substrate. This is a tough feat to achieve especially for the atmospheric SALD device at TNO, as the system is exposed to the atmosphere which could contribute to the contamination of the gases. Moreover, the rate of reactions on the substrate should be high and the nature of the reactions should be irreversible in order to achieve growth saturation rapidly [76]. Ideally, after reaction with the substrate the reactant should not decompose, etch or damage the substrate or the growth of the layer on the substrate. However, a lot of irregular behavior in deposition is observed for different temperature regimes using the ALD process.

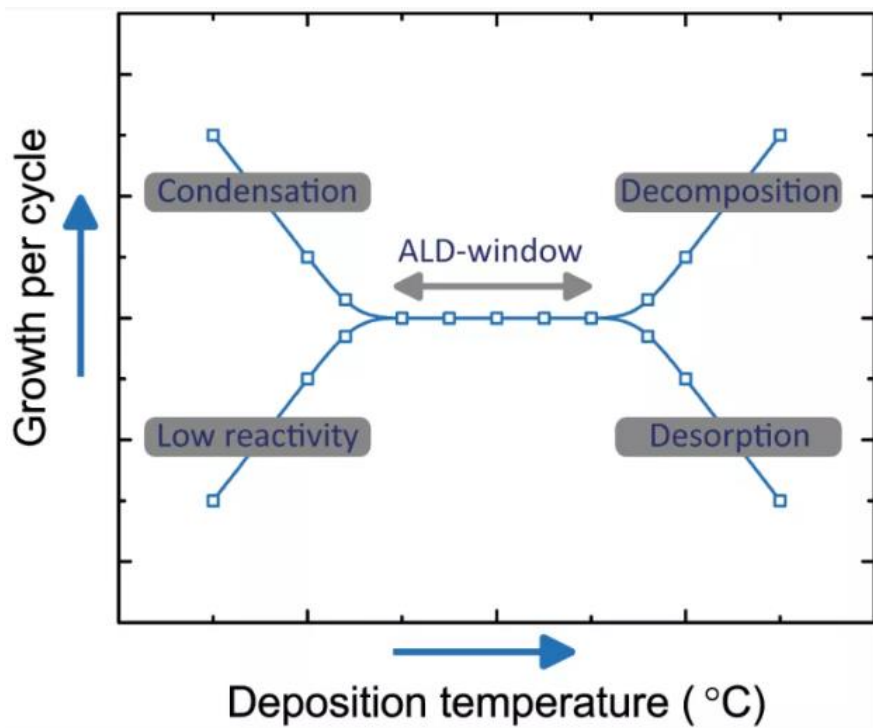


Figure 23 ALD temperature window [77]

An ideal behavior of the reactant is observed in what is referred as the “ALD temperature window” [78]. This is depicted in Figure 23. In the ALD temperature window, the growth for each cycle has reached saturation and does not increase or decrease with the temperature. However, outside the ALD window the growth during each cycle of deposition varies. At lower temperatures, due to the lack of thermal energy for completing the reaction the reactants could condensate resulting in reduced growth. It could also be possible that the precursors do not react properly with the substrate, resulting in increased growth due to physisorption. At higher temperatures, the precursors could undergo decomposition and be adsorbed on to the substrate, resulting in increased growth. This would be similar to growth by CVD. Such increased CVD growth is also observed as a result of overlapping pulses, when both precursors in the gas phase simultaneously exist near the gas substrate. It is also possible that due to the excess thermal energy, some adsorbed precursor species are released or desorbed out of the substrate resulting in decreased growth [74, 75]. This ideal behavior could be particularly useful for depositions where a uniform temperature is difficult to maintain. However, this behavior is not shown for many ALD process. The lack of ideal behavior could also be useful when irregular growth distribution due to the by-products generated during deposition could be compensated by the known growth distribution due to the temperature gradient.

Another important criterion contributing to the irregular growth could be the size of the precursor specie. A big precursor with heavy ligands would inhibit the reactions taking place in the next precursor step. It might also reduce the number of active sites. This would result in non uniformity in layer. Hence, it is preferred to have small precursors. This phenomenon of non uniformity in layer growth due to a big precursor specie is called steric hindrance[76]. This phenomenon could certainly play a role in determining the layer growth for this project because of the bulky molecular structure of the DADI precursor as it can be observed in Figure 24.

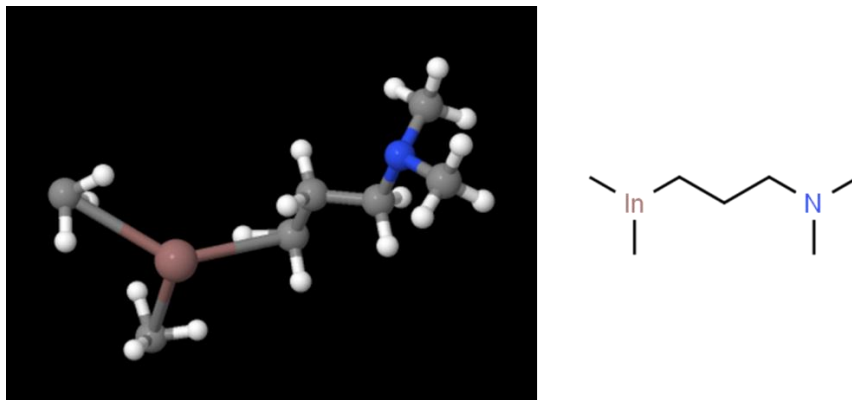


Figure 24 Ball-stick model and structural formula of [3-(Dimethylamino)propyl] (dimethyl) indium (DADI) [79]

# 4 IO:H deposited by plasma enhanced spatial atomic layer deposition

In this chapter, an investigation is performed to develop the PESALD process for IO:H deposition using the novel DADI metal precursor. Firstly, the methodology used to analyse the samples in terms of its growth, electrical, optical, structural and ageing properties has been put forth. In the subsequent section, the process parameters used for performing the experiments are briefly introduced and explained. This is followed by the section where the influence of process parameters on the layer properties has been shown through experimental results. These results are discussed and based on them, apt process conditions are set for the deposition. Finally, the results are summarised in the final section of the chapter and recommendations are made to further investigate and improve the process.

The primary focus of these experiments has been to improve the electrical properties of the deposited samples at a low reactor temperature while simultaneously monitoring the growth of the layers using the new DADI precursor. This is done in order to obtain a suitable reference condition for extending this research in the future. Since deposition of IO:H by PESALD is extremely novel and unique, electrical conductivity of the deposited layer was chosen as the first criterion to optimise the process. Also, IO:H is known to be a high mobility TCO with low free carrier absorption in the near infrared region (NIR) and high transmittance in the visible region hence these criteria have been investigated to find the apt reference condition. In addition to this, structural analysis and ageing effects of the layers have been looked into as well to further bolster the argument. Finally, the most suited reference condition is chosen for a PV demonstrator whose results will be presented and discussed in chapter 5.

A major portion of the research questions related to the process development are discussed and answered in this part of the report. The main research questions as mentioned in section 1.6 guiding the research activities are the following.

1. What are the process conditions required for successfully depositing IO:H using the PESALD process?
  - a. What is the apt precursor pickup flow?
  - b. What is the apt H<sub>2</sub> concentration in the plasma?
  - c. What is the apt substrate velocity?
  - d. What is the apt H<sub>2</sub>O concentration in the plasma?
  - e. What is the temperature range in which this deposition can take place?
2. How are the optical and structural properties of the IO:H layer influenced by the variable reactor temperature and H<sub>2</sub>O concentration in the plasma?
3. How is the reliability of the IO:H layer influenced by the variable reactor temperature and H<sub>2</sub>O concentration in the plasma?

## 4.1 Methodology

IO:H has been deposited using the PESALD setup described in section 3.2. Corning Eagle XG borosilicate glass substrates of dimension 150x150x0.7mm were used for performing the deposition. Glass substrates

were cleaned in an ultrasonic bath and pre-treated with plasma for 5 mins before performing the deposition. The deposition resulted in a donut shaped deposition area as show in Figure 25 with an inner radius of ~23 mm and an outer radius of ~53 mm. This is so, because the plasma source used for these depositions has an aperture of 30 mm. Radial dependence has been observed on the samples deposited as a result of which growth and electrical characterization of the samples was done at 3 distinct radii, 30 mm, 40 mm and 50 mm respectively. The geometry of the plasma source as discussed in section 3.4.3 is the main reason for this radial dependence. However, in order to draw logical comparisons and to avoid the boundary effect all other results are presented with regard to the centre of the deposition area (40 mm radial distance from the centre of the substrate). As a result of which optical and structural measurements are also obtained for the centre of the donut shaped deposition area. It is important to note that azimuthal variation in measurements in general was not observed in the system, except for a few rare occasions. Azimuthal variation is subject to occur mainly as a result of mechanical gap variations between the fixed SALD head and the rotating substrate. Those variations are expected to be small and their potential effects are not studied as part of this project. Finally, all treated substrates have been stored under ambient air conditions in protective boxes. Standard characterization techniques have been used to characterise the growth, electrical, optical and structural properties of the layers. For detailed information regarding the working of the characterization techniques, refer to Appendix A.

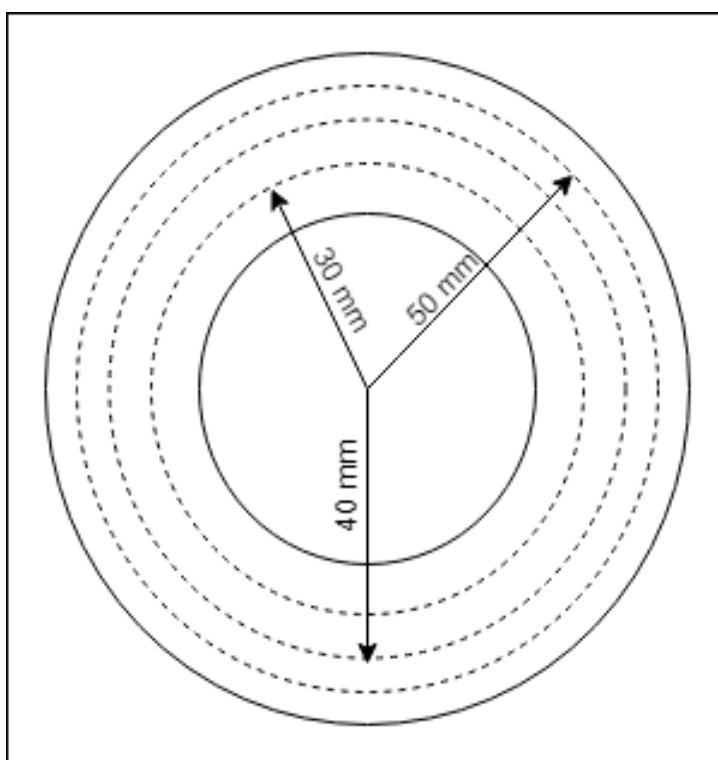


Figure 25 Donut shaped deposition area

#### 4.1.1 Growth analysis

For understanding the nature of growth in the deposited area, layer thickness and refractive indices at 2 eV (620 nm) are measured using spectroscopic ellipsometry. A Horiba UVISSEL ellipsometer with a range of 1.5-3.5 eV is used for this purpose. The elliptical beam from the ellipsometer is incident at an angle of 70 degrees and the elliptical light beam has a spot size of 2x4 mm approximately. In order to obtain maximum resolution, the spot size length is aligned perpendicular to the radius of the donut during measurement. Ellipsometer uses an optical model to represent the substrate and deposited layer. The substrate is considered optically semi-infinite in this model. Hence, in order to make the glass substrate optically semi-infinite 3M Scotch tape is stuck on its back side. This curbs the back reflections from the glass substrate. The function of the model is to extract the desired fitting parameters namely thickness and refractive index (n,k) from the measurement. Tauc-Lorentz model has been used to represent the IO:H on a glass substrate. The accuracy of the thickness measurements has been further affirmed by performing some depositions on silicon substrate. Using silicon

as the substrate ensures that there are no back reflections which results in a more accurate thickness measurement. An error in measurement of 0.3-8% for the layer thicknesses is estimated. It is important to keep in mind that this range of error takes into account all possible causes of error like the location and size of the spot from the elliptical beam, the nature of fitting and the variation observed by the repetition of tests. In order to obtain a more accurate error analysis, repeated experiments are recommended however due to the long exposure times required to perform the depositions and high occupancy of the SALD setup, this could not be done. Hence, in the results provided in this thesis however, only the error from the fitting done by the software is taken into account.

#### 4.1.2 Electrical analysis

For performing the electrical characterisation of the samples, a four point probe and a hall measurement setup have been used. A Keithley 2611A system is used for performing the four point probe measurement. Sheet resistance of the layer is obtained using this system within 24 hours after deposition. The probes are placed perpendicular to the radial direction as the point of the probes are linearly arranged. The radial resolution of the sheet resistance measurement is approximately 1 mm and is comparable with the spatial resolution of the ellipsometer. Using the sheet resistance obtained from this measurement and the thickness obtained from the ellipsometer, resistivity at the desired part of the layer is obtained by applying equation 1.9.

Furthermore, an Ecopia Hall Effect Measurement System, HMS-5000 is used for performing the hall measurement. Electron carrier density and mobility of the layer is obtained using this measurement. For this measurement, the sample is cut into 15 mm x 15 mm samples so that it could accurately fit the sample holder. The symmetry of the measurement is ensured to be  $\sim 1$  for each measurement. This is done in order to reduce error in calculation. Additionally, the resistivity obtained from this method is compared to the resistivity obtained using the ellipsometer and sheet resistance. However, the resistivity using the ellipsometer and sheet resistance is used instead of taking an average from the 4 electrode tips in the hall measurement, the latter method ensures that the resistivity is measured at a localised point.

#### 4.1.3 Optical, structural & ageing analysis

In order to obtain the optical properties, optical transmission and reflectance have been performed using an Agilent Cary 6000i UV-Vis-NIR spectrometer sensitive in the range of 175-1800 nm. The measurements have been taken in the range of 300-1200 nm. For this measurement, the sample is cut into 30 mm x 30 mm to cater to the sample holder available for this device. Before each measurement, a reference measurement referred to as the "baseline" measurement is done. It is often observed that the baseline measurement exceeds 100%. This happens because the system is not completely isolated and dark, as a result of which some light tends to penetrate into the system resulting in this error. An error of  $\sim 2-3\%$  is estimated here.

In addition to this, in order to get a clear idea of the free carrier absorption in the near infrared region, extinction coefficient ( $k$ ) is obtained in the range of 1-3.5 eV, using SCOUT software. Like ellipsometer, SCOUT software also uses optical models. It uses the O'Leary Johnson Lim (OJL) model in UV absorption and the extended Drude model in NIR. The transmittance and reflectance measurements of the samples are inputted into the SCOUT software, which fits it to an already existing model from its own database for ITO on glass substrate and corresponding spectra is obtained. This software outputs the thickness and the refractive indices ( $n, k$ ). Only the data for the extinction coefficient ( $k$ ) is used from this software, as the rest is obtained by measuring it directly from the ellipsometer. This is done because the ellipsometer did not operate in the near infrared region.

For performing the structural characterization, X ray diffraction (XRD) has been performed using a Pananalytical Empyrean XRD diffractometer. Measurements have been made with a PAN analytical Pixel1D detector using the Bragg Brentano mode in the range of  $5^\circ$  and  $90^\circ$  of  $2\theta$ . The same samples of 30 mm x 30 mm used for the optical analysis have been used here.

Additionally, the stability of the deposited layers is also tested by measuring their sheet resistances using the four point probe. To perform this analysis, samples have been placed in a damp heat test equipment at 85% humidity and 85 °C. ESPEC (LHU-124) system has been used to perform the damp heat test for a period of

900h. Each time the samples were taken out, measurement was taken using the four point probe and samples were placed back into the equipment. Additionally, to understand the natural degradation the sheet resistance of the samples were also recorded after a month after being exposed to ambient conditions.

## 4.2 Process Parameters

Based on the working of the PESALD setup as explained in section 3.2, Table 2 enlists the process parameters that have been adjusted during the course of this project. The range of variations performed and the reference condition used based on previously obtained results have also been provided.

Process Parameter	Range of Variation	Reference condition
DADI precursor pickup flow (slm)	0.1, 0.2, 0.3, 0.5, 0.7	0.5
Plasma down flow [F] (slm)		5
Plasma top flow (slm)	1, 2	2
Hydrogen concentration in the plasma [H <sub>2</sub> ] (%)	19, 39	39
Water concentration in the plasma [H <sub>2</sub> O] (%)	3.4, 6.7, 9.3	3.4
RPM [N]	20, 30, 40, 50, 60, 80	20, 30
No. of cycles [N <sub>c</sub> ]	800, 1600, 2400, 3200, 4000	800
Reactor temperature (°C)	120, 140, 150, 160, 180	150, 160
Plasma Voltage (kV)		5.2
Plasma repetition rate (kHz)		66.7

Table 2 List of process parameters and their range of variation

### Note

1. Flows are indicated in standard liters per minute which is a common unit in atmospheric pressure treatment. 1 slm corresponds with a liter gas volume at standard test conditions i.e 273 K temperature at 1 atmospheric pressure (1 bar = 10<sup>5</sup> Pa).
2. The DADI precursor pick-up flow gas is Argon and the bubbler is kept at a constant temperature of 22 °C. The total precursor flow is kept constant at 1.0 slm by adding N<sub>2</sub> gas to the Ar bubbler flow downstream the bubbler.
3. As mentioned in section 3.2, the plasma used in this setup comprises of H<sub>2</sub>, N<sub>2</sub> and H<sub>2</sub>O. Their compositions are varied to obtain the most optimum conditions. Plasma flow in the source used is a combination of two flows, down flow and top flow, this nomenclature is explained in section 3.4.3. The down flow comprising of H<sub>2</sub>, N<sub>2</sub> and H<sub>2</sub>O has been fixed at 5 slm for all the experiments. Either 1 or 2 slm N<sub>2</sub> has been used for the top flow. For the majority of the tests performed and all the results reported in this thesis, a top flow of 2 slm has been used. This is so because 1 slm top flow resulted in an additional heating effect of the plasma gas.
4. The plasma heats up the plasma source with an additional 30 °C at maximum. This temperature increase will have no or negligible effect on the substrate surface temperature.
5. Initially, only one Controlled Evaporation Mixing unit with maximum water vapor delivery of 8 g/h (corresponding to the reference condition of 3.4 %) was available during operation. However, during the project another CEM with a maximum water vapor delivery of 15 g/h could be added resulting in total percentages of 6.7 and 9.3% at net water vapor delivery of 16 and 23 g/h respectively. As a result of which the role of increased water concentration in the plasma could be investigated.
6. Here, RPM refers to the frequency of the rotating substrate below the fixed injector head as depicted in Figure 16 a) and no of cycles refers to the number of times the substrate rotates. This is a key parameter as it directly influences the exposure of the substrate underneath the injector head.

7. Reactor temperature refers to the temperature of the oven in which the PESALD process takes place. One of the main motive of this project is to obtain good quality IO:H layer at lowest possible temperature to increase the applicability of the process.  $\text{In}_2\text{O}_3$  is known to crystallize at 140 °C [80], hence as a starting point 150 °C is used as the reference for the reactor temperature.
8. The plasma voltage and repetition rate settings have not been varied based on experiments performed previously. A higher magnitude of plasma voltage and repetition rate resulted in heating of the source which led to high resistivities and a lower magnitude would result in poor layer quality due to insufficient radicle formation in the plasma.

### 4.3 Process sensitivity

It is important to note that during the depositions, the reproducibility of the process has often found to be questionable which could be attributed to the contamination in flow lines. An example of the reproducibility tests is shown in Figure 26. Here, Sample A, Sample B and Sample C, Sample D are deposited with identical process conditions. These depositions were performed in the same day. To know the exact process conditions check Appendix B.3. The difference in resistivity of the layers deposited using identical conditions at radii 30, 40 and 50 mm have been shown below. There was not a significant difference observed in the thickness of the layers for sample A and sample B. Meanwhile for sample C and sample D, there was no significant difference in thickness observed except at the outermost radius (50 mm), resulting in a higher difference in resistivity for this point. Sheet resistance vary significantly for each measurement for both the cases. Refer to the Appendix B.3 for the thickness and sheet resistance at the corresponding radii.

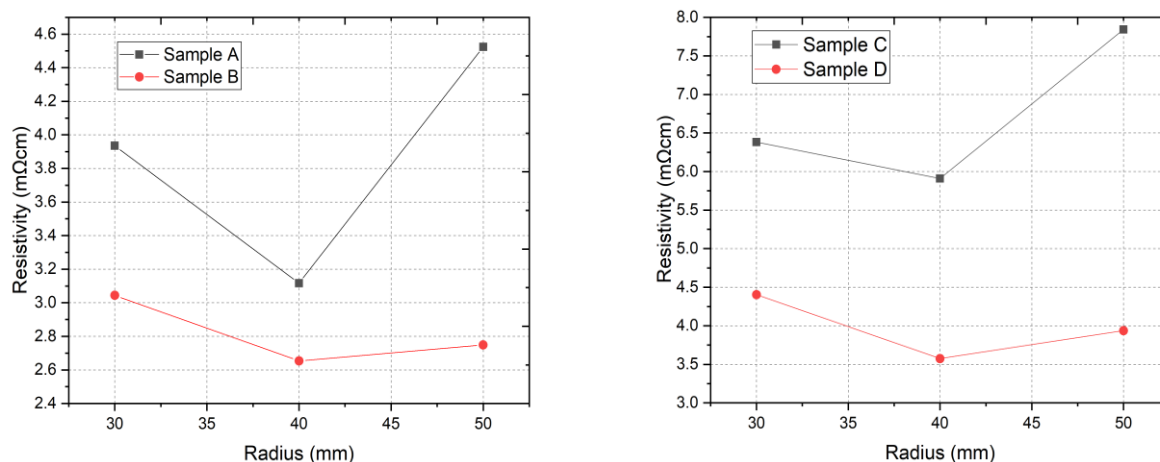


Figure 26 Reproducibility results for samples deposited at identical process conditions

Although, the sample size of these experiments is limited and there are not sufficient data points to pass a concrete verdict, certain interpretations can still be made since the magnitude of variation is quite significant even for the limited data set. Based on the results, it can be inferred that the reproducibility of the process is an issue. This could be due to the sensitivity of the process to minute oxygen concentrations in the plasma gas line. The process is very susceptible to oxygen contamination due to operation at atmospheric conditions. Another reason for the lack of reproducibility could be due to the contamination of the gas flow lines since the same lines have been used for performing other experiments. Before performing the experiments for IO:H, the PESALD setup was often used to perform depositions using Gallium. This could be one of the causes of contamination in the gas flow lines. Furthermore, a radial dependence in the deposited layers is evident from these results and is attributed to the plasma source design as previously mentioned in section 3.4.3.

### 4.4 Growth and electrical properties

To make an evaluation of the ALD process, it is essential to investigate the growth properties of the layer. A layer's growth rate is dependent on several factors like the concentration of reactants, activation energy, temperature etc. Growth per cycle or GPC, a commonly used terminology of the ALD industry, is used for performing this investigation. GPC refers to the ratio of the thickness of the deposited layer to the number of

cycles required for making the deposition. From GPC values at systematically varied operating conditions, a comment on the saturation regime is made. Additionally, since this project focuses on the deposition of a TCO layer by PESALD, attention needs to be paid towards the electrical properties of the deposited layer as well. To accomplish this, conductivity of the layer along with its carrier density and mobility are measured and compared. It is important to note that conductivity of a layer and its thickness are directly linked to each other as shown previously in equation 1.9. All the results presented in the coming sections are from the center of the donut shaped deposition area i.e. 40 mm radius from the centre, unless stated otherwise. This section provides the major essence of the report as process parameters are set and assigned based on the results obtained in this section.

First, the growth and electrical properties are investigated and used to find the appropriate DADI precursor partial pressure. This is followed by exploring the influence of different exposure times, simply by varying the substrate velocity. Based on these results a suitable substrate velocity is chosen as reference for the following experiments. Thirdly, the concentrations in the plasma gases are altered. Starting with the concentration of H<sub>2</sub>, this is followed by the simultaneous research of the concentration of H<sub>2</sub>O in the plasma along with the reactor temperature.

#### 4.4.1 Influence of DADI precursor partial pressure

DADI, the metal precursor used in this work has been used for the first time to perform deposition of IO:H using PESALD. Its properties and advantages over other precursors which resulted in it being the precursor of choice for this project were enlisted in section 3.3. Hence, based on the reference conditions previously obtained by using TMI (trimethyl indium) first the effect of DADI's partial pressure has been investigated. As previously stated in section 4.3, this is done by varying the flow of Argon gas through the bubbler while keeping the net flow constant.

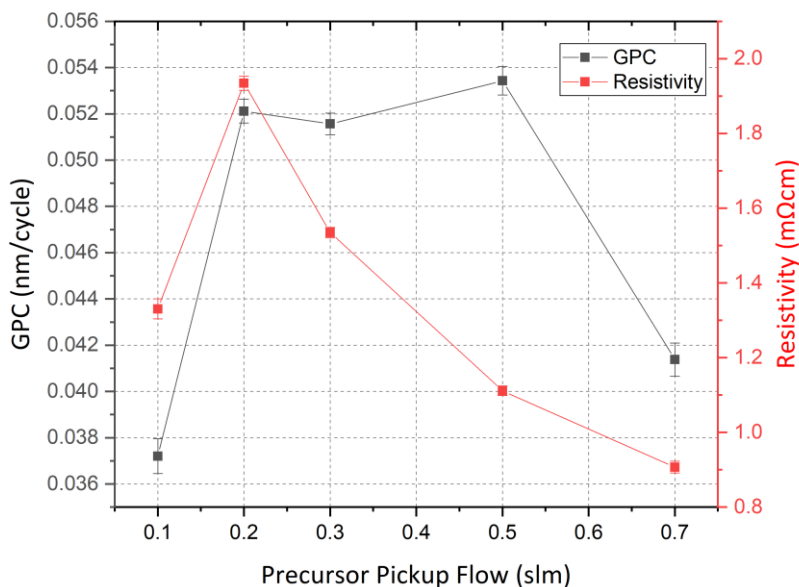


Figure 27 Influence of the DADI partial pressure on GPC and layer resistivity at 40mm radius. Process conditions:  $T=150^{\circ}\text{C}$ ,  $\text{RPM}=20$ ,  $N_c=800$ ,  $F=5\text{ slm}$ ,  $[\text{H}_2]=39\%$ ,  $[\text{H}_2\text{O}]=3.4\%$

Figure 27 depicts a plot of GPC and resistivity versus the DADI precursor pickup flow. A saturation in terms of GPC can be observed as the precursor pickup flow is increased from 0.2 to 0.5 slm. However, an unexpected deviation in trend is observed for the GPC at 0.7 slm. Purely based on the GPC, it can be deduced that even 0.2 slm precursor pickup flow is sufficient for a saturated growth. A maximum GPC of ~0.05 nm/cycle is observed by using DADI which is significantly lower as compared to the GPC observed by using TMI at similar process conditions (0.09 nm/cycle). This may be attributed to the phenomenon of steric hindrance, due to the bigger size of the DADI molecule as compared to TMI as it had been previously mentioned in section 3.5. This value of GPC however remains unprecedented as before this, Maeng et al. recorded a GPC of 0.06 nm/cycle using DADI precursor at a substrate temperature of 275 °C [81].

Even though 0.2 slm of precursor pickup flow seems sufficient for the layer growth, high resistivity of 1.9 mΩcm is observed at this pickup flow. The trend of resistivity suggests an improved conductivity of the layer with increased pickup flow, thus making high pickup flows of 0.5 and 0.7 slm particularly interesting in terms of conductivity. Based on this trend, a further decrease in resistivity could be expected at higher precursor partial pressure. This may be attributed to a changed stoichiometry of the different materials composing the layer. This hypothesis can be verified by performing an analysis of the layer composition, e.g. by the elastic recoil detection technique (ERD). It is important to note that the errors depicted for resistivity in this thesis are cumulative errors. These are calculated by taking into account the error in thickness measurements, for which the error provided from the ellipsometer as a result of the curve fitting is taken into account and the error in sheet resistance measurements, for which multiple measurements were made on different azimuthal positions at 40 mm radius. The errors for mobility and carrier density are obtained merely by performing the measurements multiple times.

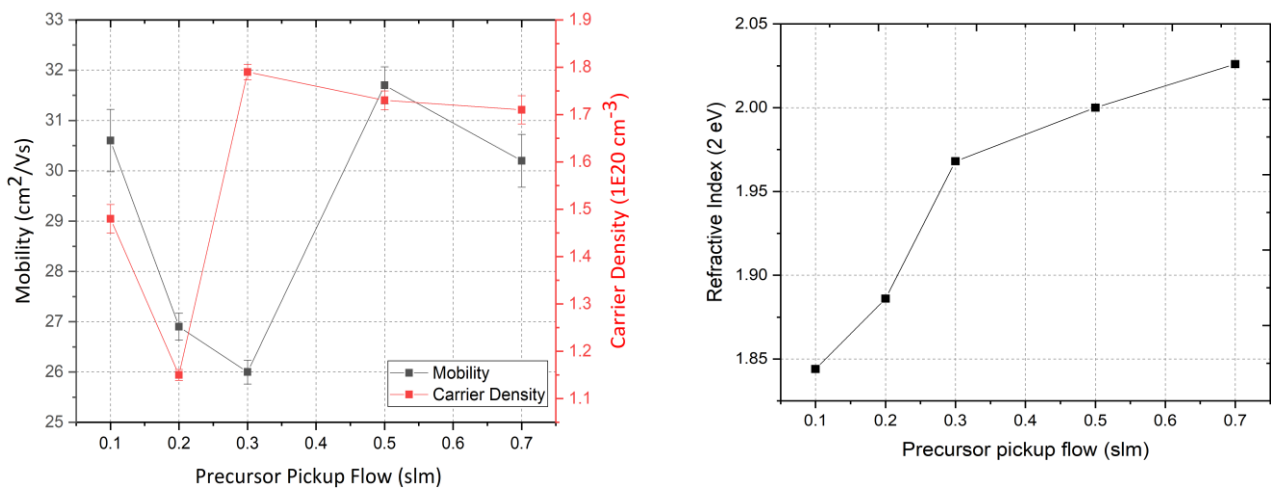


Figure 28 Influence of the DADI partial pressure on mobility, carrier density and refractive index at 40mm radius at identical process conditions as Figure 27

In order to choose the apt precursor partial pressure, the mobility, carrier density and refractive index data have been analysed. The results are displayed in Figure 28. The results for mobility and carrier density are concurrent with the results obtained with resistivity, stating 0.5, 0.7 slm as the most apt pickup flow with the highest mobility and carrier density. The refractive index also provides interesting information. An increase in refractive index is observed for increasing precursor pickup flow. Even though a saturation in GPC has been observed in this region the refractive index still changes. This means that the composition of the layer continues to change even in this saturated growth regime. This may be attributed to the increased amount of hydrogen in the layer as a DADI molecule comprises of 18 hydrogen atoms per indium. This can be observed in the ball stick model and structural formula of DADI depicted in Figure 24. Additionally, this range of refractive index at 2 eV, equally shown in Figure 64 is indicative of a crystallized structure of the deposited IO:H. This can be substantiated by the results obtained by Macco et al. as depicted in Appendix B.4. Hence, combining the electrical analysis with the growth based analysis, 0.5 slm appears to be the most suitable DADI precursor pickup flow for these process conditions.

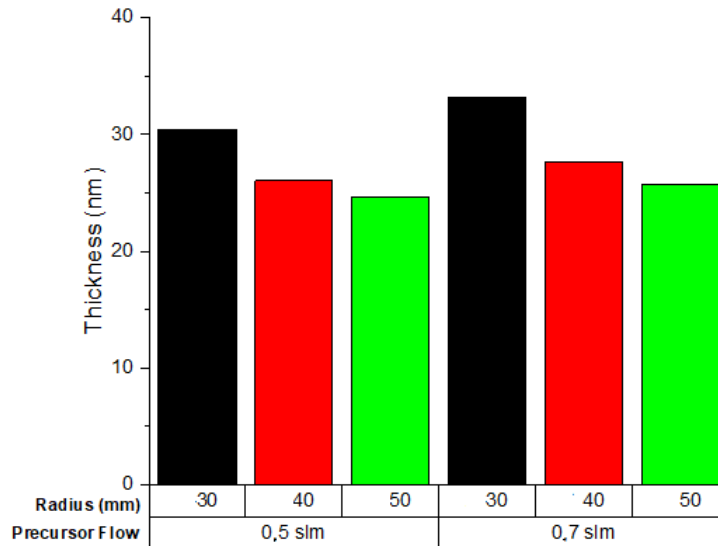


Figure 29 Influence of the DADI partial pressure on thickness deposited on Si Process conditions:  $T=150^{\circ}\text{C}$ ,  $\text{RPM}=80$ ,  $N_c=1000$ ,  $F=5\text{ slm}$ ,  $[\text{H}_2]=39\%$ ,  $[\text{H}_2\text{O}]=9.3\%$

In order to further affirm the correct precursor pickup flow (between 0.5 and 0.7 slm) for different process conditions, an experiment was performed on Si substrate and the growth of the layer was analysed. As the thickness measurement on a Si substrate is more accurate because of absence of back reflections. Here, the  $[\text{H}_2\text{O}]$  is increased three times and the rotation frequency of the substrate is 80 RPM as compared to 20 RPM in the previous case. The result obtained here is a typical example of an unsaturated process. The variation in the thickness of the sample at different radii of the donut is a clear indicator of unsaturation. Unsaturation could be caused by lack of precursor or radicals. In order to check this, the precursor pickup flow is increased however still a similar trend in thickness indicating unsaturation has been observed. Hence, it can be deduced that in the process growth is limited due to radicals and not the coating precursor. Thus, 0.5 slm is the sufficient precursor dose for this condition as well. On the basis of these results, 0.5 slm has been set as the precursor pickup flow for all other experiments.

#### 4.4.2 Influence of $[\text{H}_2]$

$\text{H}_2$  is one of the constituent gases of the plasma used for this process. In the past, experiments conducted in an absence of  $\text{H}_2$  from the plasma mix have resulted in poor conductivity of IO:H. It has been reported in literature that the concentration of singly charged H donors play a very significant role in determining the dominant scattering mechanism in IO:H. It is said that 4% of incorporated H acts as an active dopant in crystallized IO:H layers, based on this it can be concluded that inactive H atoms do not contribute to defect scattering. This is the primary factor that results in higher mobility of IO:H than commonly used TCO, ITO [50]. Hence, knowing the concentration of H in the layer is essential to draw any conclusion with regard to this. However, this investigation has not been performed in this project instead investigation is made to understand the influence of changed concentration of hydrogen gas in the plasma mix for the unique PESALD process.

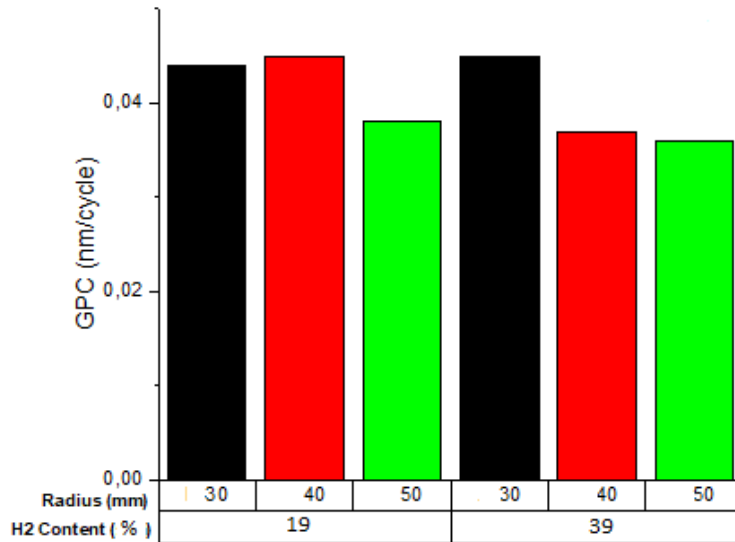


Figure 30 Influence of  $[H_2]$  in the plasma on GPC Process conditions:  $T=160^\circ C$ ,  $RPM=30$ ,  $N_c=2400$ ,  $F=5\text{ slm}$   $[H_2O]=6.7\%$

Figure 30 shows a plot of GPC versus  $[H_2]$  at three radii (30, 40 and 50 mm) of the deposited area. This is done in order to analyze the growth effects due to variable  $[H_2]$  in the plasma. As it can be seen from the result, there is not a very substantial difference in the GPC between the two concentrations at the inner and outer radii of the deposited area (30 mm radius and 40 mm radius) respectively. A reduction in GPC at the center of the donut (i.e. 40 mm radius) is however observed and could be attributed to the commonly known effect of  $H_2$  etching. However, overall the influence on GPC by increased  $[H_2]$  is not particularly significant.

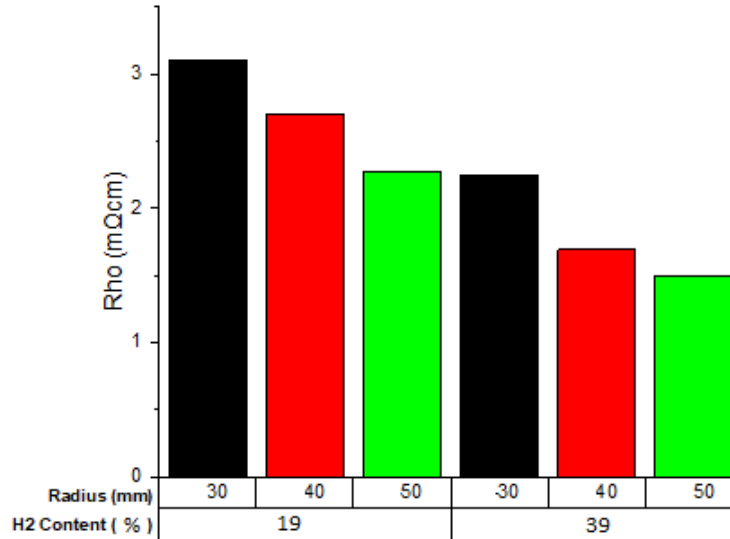


Figure 31 Influence of  $[H_2]$  in the plasma on resistivity using identical process conditions as Figure 30

Since the growth results did not provide a clear advantage or disadvantage of using a higher or lower  $[H_2]$ , it becomes essential to assess the electrical properties of the layer for the two concentrations. The results for the effect on resistivity of the layer at three radii on the deposited area are presented in Figure 31. Based on these results, it can be concluded that a higher  $[H_2]$  has resulted in improved resistivity over the entire deposited area. Furthermore, a higher  $[H_2]$  has resulted in improved mobility and carrier concentrations as well. A mobility of  $73\text{ cm}^2/Vs$  and carrier density of  $0.5 \times 10^{20}\text{ cm}^{-3}$  as compared to a mobility of  $55\text{ cm}^2/Vs$  and carrier density of  $0.4 \times 10^{20}\text{ cm}^{-3}$  have been observed. An explanation for improved electrical properties can be due to the role of hydrogen to counteract the oxygen contamination in the system. Since, the

deposition is performed under atmospheric pressure conditions (i.e. vacuum outgassing of the reactor has not been performed), there may be a considerable amount of oxygen in the system from desorption of the reactor materials even when the supplied gasses have a very high purity. In the past, previous experiments have shown that introducing oxygen has had detrimental effects in this process. Hence, it is a good possibility that high [H<sub>2</sub>] in the system acts as an agent acting against the O<sub>2</sub> contamination and thus improves the electrical properties of the layer. On the basis of this, high [H<sub>2</sub>] of 39% corresponding to 2 slm of flow has been used for the following experiments. It is important to note that a higher [H<sub>2</sub>] concentration was not tried for these experiments due to the safety concern that such high [H<sub>2</sub>] would pose due to its combustible and flammable characteristics.

#### 4.4.3 Influence of substrate velocity

The velocity of the substrate directly influences the amount of time different regions of the substrates are exposed to the reactor head. The exposure time is often used as a parameter to understand the growth and electrical properties. However, using exposure time as a parameter would be recommended if the exposure times at each radii were maintained constant. This is true for the pie shaped metal precursor slot however this does not hold true for the linear plasma slot. The plasma slot is linear over the entire radius of the deposition area, hence resulting in a radially varying exposure time. This is why substrate velocity is used as a parameter to understand the growth and electrical properties of the layer deposited. Additionally, it's important to note that this experiment is performed at a reactor temperature of 160 °C. And for each RPM setting, the thermal budget of the process is kept constant. Thermal budget is defined as the product of temperature and time in which deposition is performed. Hence, to keep the thermal budget constant the number of cycles is set to 2400, 3200, 4000 and 4000 for 30, 40, 50 and 80 RPM respectively. For 80 RPM, 4000 cycles were chosen instead of 6400 to avoid depositing very thick layers (>250 nm). The value for the precursor pickup flow (0.5 slm) and [H<sub>2</sub>] (39%) has been fixed and used based on the results previously discussed.

$$velocity (v) = \frac{2\pi N}{60} \times r \quad (4.1)$$

RPM (cycles/min)	Radial distance (mm)	Velocity (m/sec)
30	30	0.09
	40	0.13
	50	0.16
40	30	0.13
	40	0.17
	50	0.21
50	30	0.16
	40	0.21
	50	0.26
80	30	0.25
	40	0.34
	50	0.42

Table 3 List of velocities at different radii for different rotation frequencies

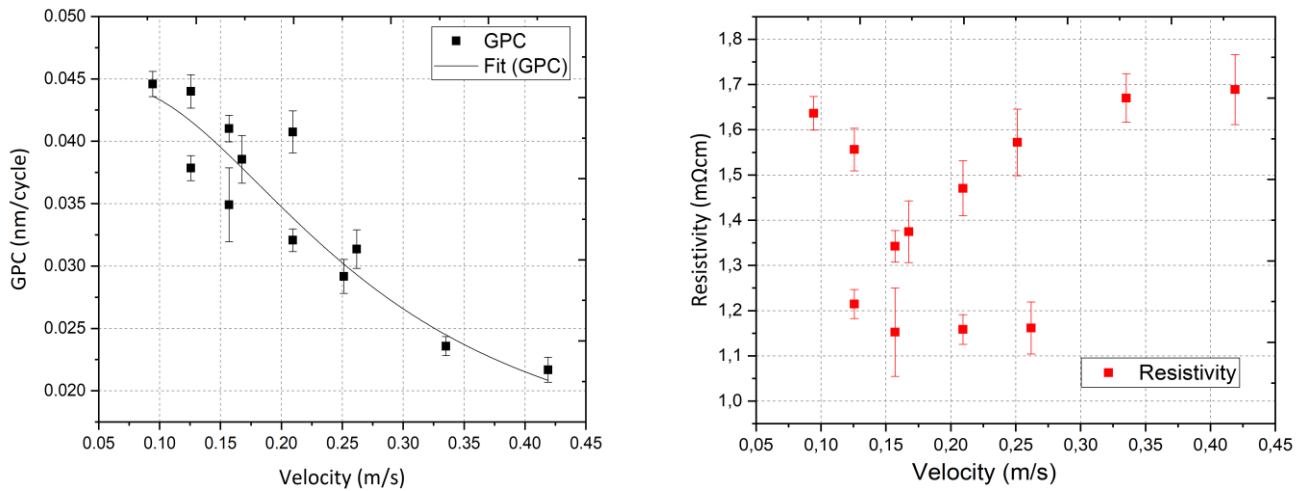


Figure 32 Influence of velocity of a point on the substrate on GPC and resistivity. Process conditions:  $T=160^{\circ}\text{C}$ ,  $F=5\text{ slm}$ ,  $[\text{H}_2]=39\%$ ,  $[\text{H}_2\text{O}]=9.3\%$

The influence of velocity on growth and electrical properties can be observed in Figure 32. Here, velocity refers to the velocity at a distinct radius on the substrate rotating with a particular rotation frequency. The velocities presented here are an accumulation of velocities at radii of 30, 40 and 50 mm for the rotation frequency of 30, 40, 50 and 80 RPM respectively. The velocities are calculated using equation 4.1, where  $N$  represents the rotation frequency and  $r$  represents the distance of the point from the centre of the donut (radial distance). The velocity obtained from the rotation frequency are shown in Table 3.

The trends obtained in Figure 32 clearly depict the influence of the linear plasma slot as growth and electrical properties for the same substrate velocities (or same exposure times) vary quite significantly from each other. On the basis of these results, it is seen that the GPC is continuously increasing at lower velocity indicating that there is no saturation reached for the ALD process even at low velocity (or high exposure time). This undersaturated growth is attributed to the shortage of plasma radicles in the process as the DADI precursor pickup flow is not the limiting factor here as previously depicted in section 4.4.1. Moreover, this discards the hypothesis of an etching effect by hydrogen which was proposed in the previous section. As the negative effect on the growth by hydrogen should have been more evident at low velocities (high exposure times). It is important to realise however that the type of radicles responsible for the growth in  $\text{H}_2\text{-H}_2\text{O-N}_2$  plasma is not known. Stable radicles like OH (hydroxyl),  $\text{HO}_2$  (peroxyl) and  $\text{H}_2\text{O}_2$  (peroxide) could be playing a role here. It should be kept in mind that based on results from previous section high  $[\text{H}_2]$  (39%) has been used for these experiments. This high concentration can have an influence on the radicle recombination reactions such as  $\text{OH}+\text{H}\rightarrow\text{H}_2\text{O}$ , hence resulting in under saturated growth conditions even at high precursor partial pressure and high exposure times.

Furthermore, after combining the results for the highest GPC with the lowest resistivity, two possible data points at 0.13 m/sec and 0.16 m/sec appear to be the most promising. These datapoints correspond to the centre of the deposition area (40 mm radius) at a rotation frequency of 30 RPM and inner radius of the deposition area (30 mm radius) at a rotation frequency of 50 RPM. Since there is a high probability that measurements on the boundaries of the deposition area are influenced by the flow effects in this process, due to the plasma source design, 30 RPM is chosen to be the suitable rotation frequency for this process. But since the results presented with respect to substrate velocity do not depict a clear optimum, analysis has also been made with respect to the rotation frequency to be certain.

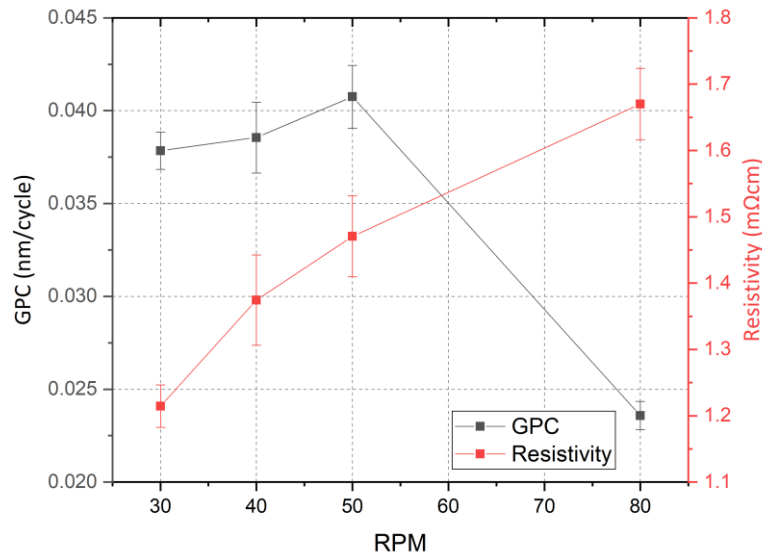


Figure 33 Influence of rotation frequency on the growth and electrical properties of the layer at 40 mm radius. Same process conditions as Figure 32

In order to be certain about the appropriate rotation frequency, results depicting the GPC and resistivity at the center of the deposition area (40 mm radius) is depicted in Figure 33. As it can be seen here, the GPC values are comparable in the range of 30-50 RPM indicating that growth is not limited by the exposure time. If growth was limited by the exposure time, higher GPC would have been observed for a lower RPM. In addition to this, as it can be observed the lowest resistivity is obtained at 30 RPM.

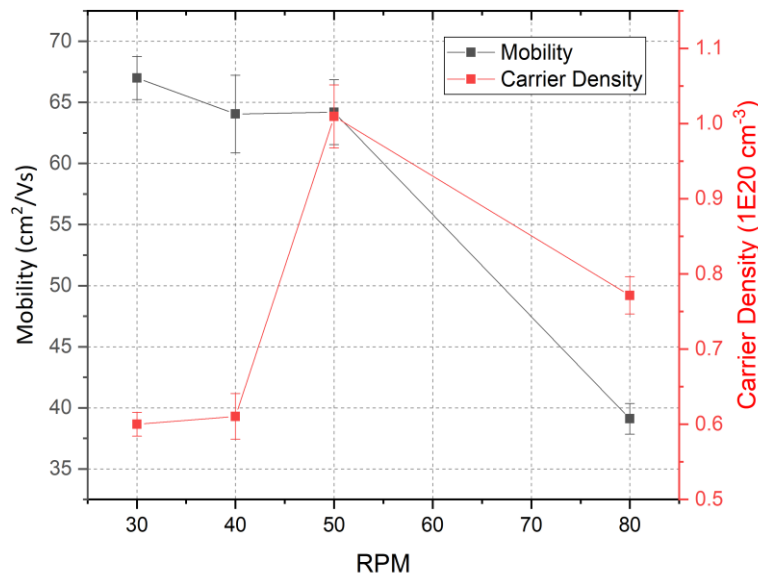


Figure 34 Influence of rotation frequency on the mobility and carrier density of the layer at 40 mm radius. Same process conditions as Figure 32

Figure 34 also confirms that 30 RPM is indeed the most apt rotation frequency due to its highest mobility in concurrence with its low resistivity and high GPC. However, this graph seems to be deviating from the expected trend of mobility, carrier density and resistivity. The carrier density seems to increase significantly (from 0.6-1.0 1E20 cm<sup>-3</sup>) when the rotation frequency is increased from 40 to 50 RPM, which should ideally result in an improvement in the conductivity. But this is not the case as resistivity has increased between 40 and 50 RPM. Also, it must be noted that the resistivity measured for the substrate at 50 RPM using hall measurement shows a very significant discrepancy as compared to the resistivity reported by using the four point probe and the ellipsometer. A resistivity of 1.1 mΩcm has been measured using the Hall measurement setup for this sample. This is one of the rare times when such a significant discrepancy has been observed

in the measurements between the two characterization techniques. Usually, the discrepancies observed are utmost 20%. This makes 50 RPM an optimum rotation frequency, however since all the resistivity values used to draw conclusions have been from the four point probe and the ellipsometer and in the past similar range of rotation frequencies (20-30 RPM) were used as a reference. It was decided to set 30 RPM as the optimum. Further reproducibility tests are suggested using rotation frequencies in the range of 30-50 RPM to be certain about the optimum.

#### 4.4.4 Influence of [H<sub>2</sub>O] in plasma and reactor temperature

Amongst all the radicals produced in the plasma mix of H<sub>2</sub>O, H<sub>2</sub> and N<sub>2</sub> for the IO:H deposition by PESALD, OH radicals are considered the most effective radicals. OH radicals are known to be very reactive. The H<sub>2</sub>O in the plasma seems to be the main source of the vital OH radicals, varying its concentration to observe its effects on the deposited layers is important. The water in the sputtering process is also known to contribute as a passivating agent for dangling bonds with hydrogen that decreases the scattering centers and hence, increases the mobility [82]. Additionally, another important factor playing a vital role in the deposition process is the temperature of the reactor. One of the driving forces for the use of the unique PESALD process is performing depositions at low temperatures. This would improve the applicability of the process. Furthermore, varying the temperature can have a major influence on both the growth behaviour and material properties in an ALD process as it directly influences the surface chemistry. An insight into the ideal temperature window of an ALD process has been previously provided in section 3.5. Based on the aforementioned factors, a simultaneous analysis has been performed for [H<sub>2</sub>O] of 6.7 and 9.3 % at a reactor temperature of 120, 140, 160 and 180 °C. An additional experiment was also performed at low [H<sub>2</sub>O] of 3.4% for 140 °C. It is important to note that the previously discussed results are used to set the process conditions for this set of experiments and this would be the last step in process development before applying it on a PV demonstrator.

It is essential to point out that the two lines depicting the resistivities, mobilities and carrier densities of sputtered ITO and sputtered IO:H in Figure 36 and Figure 37 respectively do not imply that the parameters remained constant for these samples at the variable temperature. Instead, these lines only depict the reference values for ITO and for IO:H developed at Solliance using sputtering. The layer properties for the sputtered samples are depicted in Table 4. The thickness of the reference sputtered ITO and IO:H sample is also kept comparable with the layer thickness deposited using ALD (100 ± 10nm). Improved electrical properties of the sputtered layer could be attributed to the vacuum environment in which these layers were deposited, hence low scope of contamination resulting in a high quality TCO.

	<b>Sputtered ITO</b>	<b>Sputtered IO:H</b>
Thickness (nm)	119	100
Carrier Density (cm <sup>-3</sup> )	1.78 X 10 <sup>20</sup>	2.05 X 10 <sup>20</sup>
Mobility (cm <sup>2</sup> /Vs)	51.9	117
Resistivity (mΩcm)	0.677	0.261

*Table 4 Overview of the electrical properties of the sputtered ITO and IO:H*

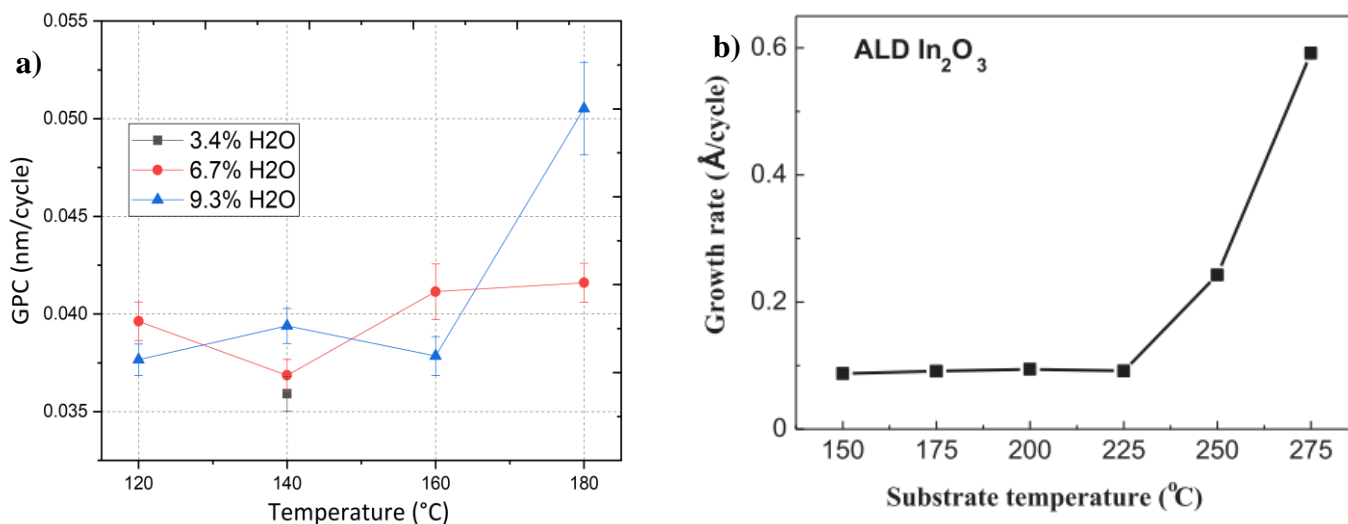


Figure 35 a) Influence of [H<sub>2</sub>O] and temperature on growth at center of the deposition area (R= 40 mm). Process conditions: N= 30 RPM, Nc= 2400, F=5 slm, [H<sub>2</sub>]=39% b) Influence of substrate temperature on GPC by Maeng et al. [66]

In Figure 35 a), the influence of reactor temperature and [H<sub>2</sub>O] on the GPC is observed. It is observed here that the GPC has not been influenced much by the reactor temperature and variable [H<sub>2</sub>O], except for one case where the temperature is increased to 180 °C and [H<sub>2</sub>O] is kept high at 9.3%. This rise in GPC here might be understood by hypothesizing the reaction mechanism during the plasma step of the PESALD process. It might be that during the reaction of chemisorbed DADI and OH radicals from plasma, faster desorption of reaction products due to increased temperature leads to additional reaction sites. As a result of which, the effect of steric hindrance is reduced during the ALD reaction, resulting in increased GPC (Refer section 3.5 for steric hindrance). An ideal case of ALD temperature window as discussed in section 3.5 is not observed here, however the GPC seems to be in a comparable range in the region of 120 to 160 °C. In this temperature range, soot (carbon deposits) as reaction product might also be formed. Additionally, it's good to mention that the GPC observed here is comparable to the previously reported GPC by Maeng et al using DADI precursor with ozone as co-reactant as depicted in Figure 35 b). In fact, it can be observed that a GPC of ~0.04 nm/cycle is achieved at relatively lower temperature due to the incorporation of plasma in the ALD process.

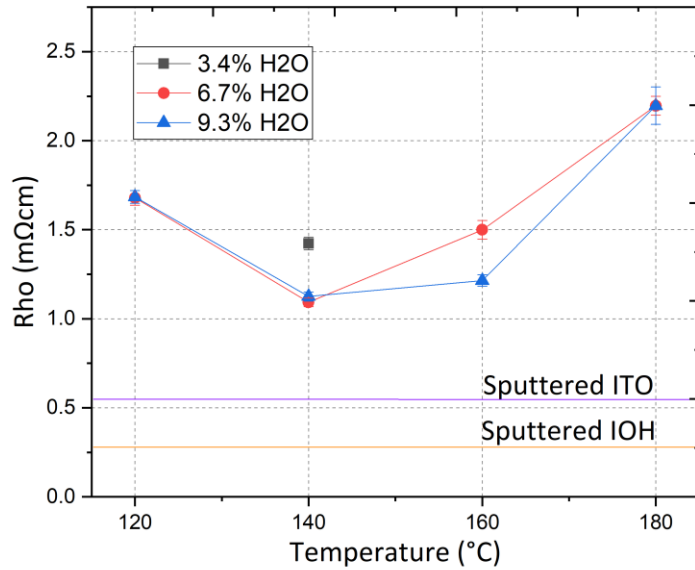


Figure 36 Influence of temperature and [H<sub>2</sub>O] on resistivity at center of the deposition area (R= 40 mm) Same process conditions as Figure 35. Note that the two lines depicting sputtered ITO and sputtered IOH are merely reference lines and do not intend to depict a constant resistivity of these samples as a function of temperature.

The resistivity of the layers as a function of the reactor temperature is depicted in Figure 36. From these results, a clear minimum in resistivity (~1.1 mΩcm) has been observed for a temperature of 140 and 160 °C. At 140 °C, there is no difference in resistivity for 6.7% and 9.3 % [H<sub>2</sub>O] however a difference in resistivity was caused by the different [H<sub>2</sub>O] for 160 °C. The increased OH radicals in the plasma mix due to a higher [H<sub>2</sub>O] of 9.3 % might have resulted in improved resistivity at a reactor temperature of 160 °C. For temperature of 120 and 180 °C as well, there is no difference in resistivity observed for 6.7% and 9.3 % [H<sub>2</sub>O] but a higher resistivity was measured at these temperatures. A crucial point to note here is that, a discrepancy in measured resistivity at 180 °C, 9.3 % [H<sub>2</sub>O] was observed by using the hall measurement setup indicating 0.7 mΩcm.

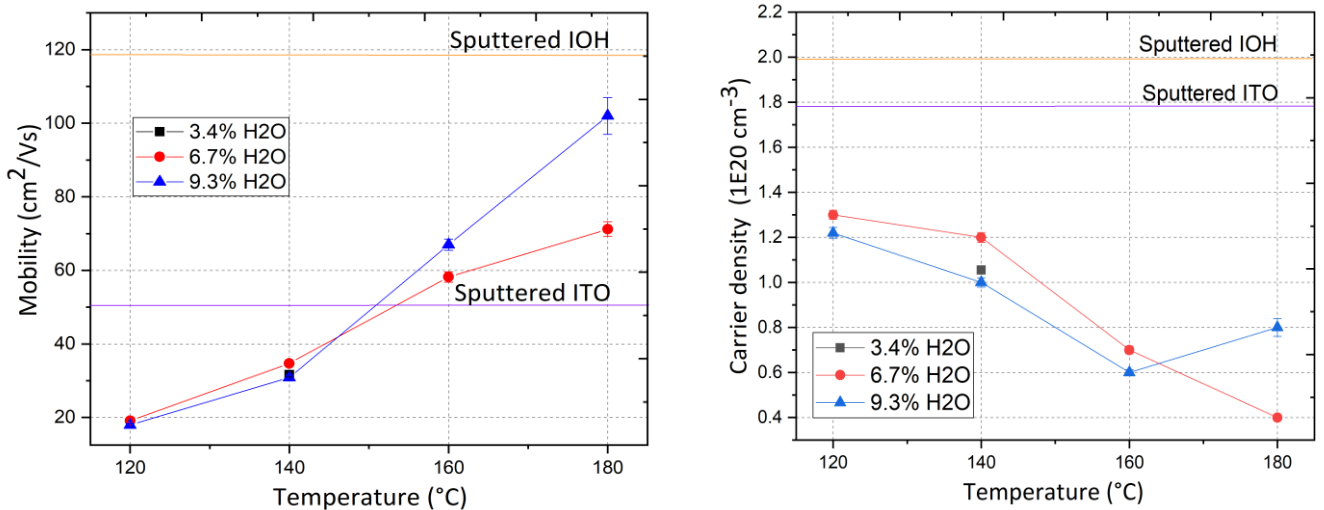


Figure 37 Influence of temperature and [H<sub>2</sub>O] on mobility and carrier density at center of the deposition area (R= 40 mm) Same process conditions as Figure 35. Note that the two lines depicting sputtered ITO and sputtered IOH are merely reference lines and do not intend to depict constant mobility and carrier density of these samples as a function of temperature.

Figure 37 depicts the trends of mobility and carrier density with temperature for different [H<sub>2</sub>O]. This result depicts an increase in mobility and decrease in carrier density with increasing temperature for both 6.7% and 9.3% [H<sub>2</sub>O]. This trend is consistent with the trends observed for post annealed IO:H deposited by ALD from

Macco et al [80]. This trend is indicative of a crystallized nature of the IO:H. In the work of Macco et al, improved crystallinity is reported with increasing mobility. From annealing studies of IO:H, it is seen that different factors play a role resulting in the trend for mobility and carrier density. In situ Hall measurements provide some crucial insights with regard to this but at the same time poses some voids which need to be further investigated [83]. Furthermore, it has been recently shown that post deposition crystallization is a crucial step in order to ensure high mobility for IO:H [82]. This could be the reason why high mobility is not obtained using PESALD process. However, it is important to keep in mind that most of the references focus on sputter deposited IO:H using post deposition annealing. This makes it difficult to compare these results to the ones reported since a post deposition annealing step is not required in this process as the layers are already crystalline. A more concrete comment on the crystallinity of the layers could be made by doing structural analysis. This effect will be shown and discussed in section 4.7. Combining these results with the result for resistivity depicted in Figure 36, sample deposited at a reactor temperature of 160 °C and 9.3% [H<sub>2</sub>O] seems to be the most optimum, as high mobility of 67 cm<sup>2</sup>/Vs and low resistivity of 1 mΩcm is obtained here.

The only measurement deviating from the expected trend here is the one with the discrepancy in the resistivity as well i.e 180 °C and 9.3% [H<sub>2</sub>O]. An increase in carrier density is observed for this result which corresponds with the decrease in resistivity measured using the hall measurement. However, just like how the discrepancy in the past was resolved, in order to maintain consistency, the measurements of the 4 point probe and ellipsometer were chosen to set the process condition. Besides, more experiments to confirm these results would be recommended. Furthermore, the mobility for the layers deposited at 140 °C remain uninfluenced by the different [H<sub>2</sub>O], however for 160 °C, higher [H<sub>2</sub>O] (9.3 %) is preferred. This is consistent to what was observed for the resistivity of the layers. For 120 °C, like the conductivity the mobility also remains low and hence the option to perform the deposition of highly conductive IO:H at a low temperature of 120 °C is discarded for both the [H<sub>2</sub>O]. Therefore, based on the aforementioned results it is clear that the process condition of 160 °C at 9.3% [H<sub>2</sub>O] is the most optimum. However, since the low conductivity (~1.1 mΩcm) observed here for IO:H using PESALD is unprecedented, other conditions using reactor temperature of 140 °C at 9.3% [H<sub>2</sub>O] and 6.7% [H<sub>2</sub>O] are also considered promising.

In order to further ascertain these conditions, these samples were then further optically and structurally characterized, to get a deeper insight into its material properties. Furthermore, the ageing effect of the layers deposited was also investigated.

## 4.5 Optical properties

Apart from the electrical properties, the optical properties of a TCO are pivotal in evaluating a TCO. The changes that light undergoes when interacting with a particular substance are referred to as the optical properties of the substance. A good TCO should allow high transmittance in the visible and near infrared region of the spectrum. However, there are many factors which influence the optical properties of a TCO. These include the thickness of the layer deposited, occurrence of FCA due to presence of charge carriers and the shifting of band gap due to excess charge carriers, which is explained by the concept of Burstein-Moss shift as previously discussed in section 1.3.4. The phenomenon of FCA and Burstein Moss shift are interrelated. The optical bandgap is increased due to degenerate doping by the Burstein Moss shift however this comes at an expense, since the free carriers generated by doping contribute to increased FCA [22]. In this section, the results of the optical properties for the samples prepared by using the optimum process conditions as previously discussed in section 4.4 are presented. These are the same samples obtained by changing the reactor temperature and [H<sub>2</sub>O], as discussed in section 4.4.4. The quest to ascertain the optimum reactor temperature and [H<sub>2</sub>O] is continued. In this way, the results obtained in the past from the growth and electrical analysis are simultaneously evaluated and compared with the optical results and an optimum for the reactor temperature and [H<sub>2</sub>O] is ascertained.

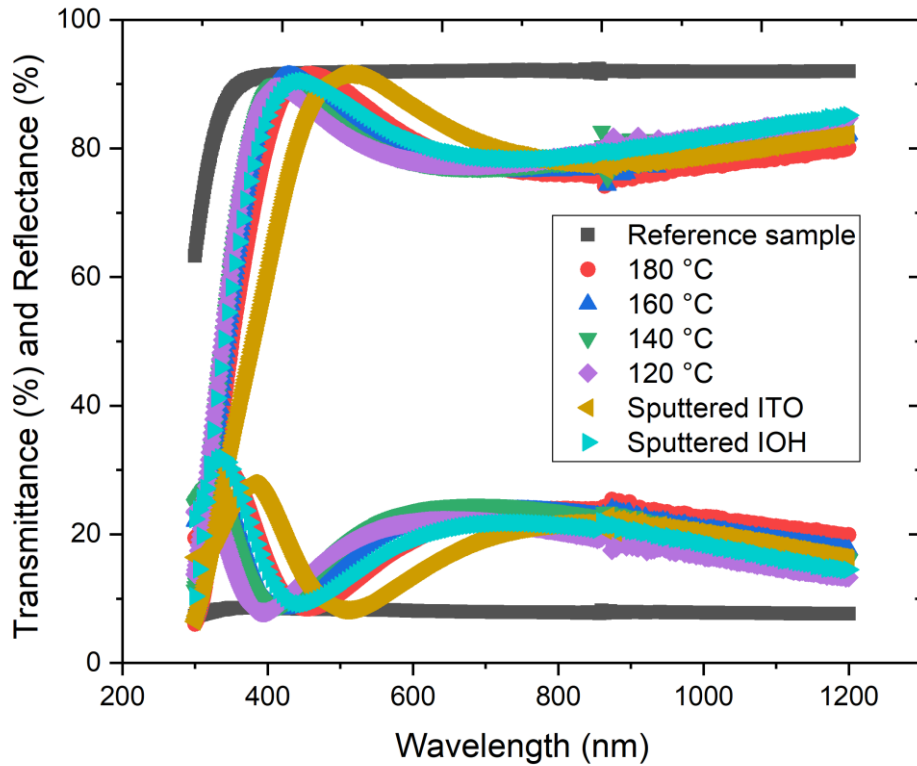


Figure 38 Transmittance & Reflectance of IO:H samples at different temperatures for 9.3% [H<sub>2</sub>O] same process condition as Figure 35

Figure 38 shows the transmittance and reflectance of the IO:H samples deposited at different reactor temperatures at 9.3% [H<sub>2</sub>O] along with the sputtered ITO and IO:H as a function of wavelength. The reference sample here depicts the uncoated glass substrate (Corning Eagle XG 0.7 mm). This glass substrate is used in high performance LCD's and was used to perform the depositions due to its high transparency. Moreover, it also possesses high surface quality, excellent thermal properties and high resistance to chemicals [84]. The measurements are obtained using a spectrophotometer. The change in [H<sub>2</sub>O] has had no real influence in the transmittance and reflectance measurements. This can be confirmed with the result obtained for different reactor temperatures for 6.7% [H<sub>2</sub>O], depicted in Figure 65 of Appendix B.5. Based on these results, an average transmittance of approximately 80% has been observed for each of these samples. A slightly higher reflectance than others can be observed for sputtered IO:H. Overall, changing the temperature has had no significant influence on the net transmittance and reflectance of the IO:H samples. The shift in wavelength corresponding to the peak in each of these samples is a consequence of the interference effects and the variable thickness of the material deposited onto the substrate. The higher the thickness, the greater the peak shifts towards to a higher wavelength. This trend can be observed for the data presented in Figure 38 and Figure 65.

Material	Thickness (nm)
Sputtered ITO	119
Sputtered IO:H	100
PESALD 180 °C IO:H	108
PESALD 160 °C IO:H	98
PESALD 140 °C IO:H	93
PESALD 120 °C IO:H	90

Table 5 Thickness of the samples compared in Figure 38

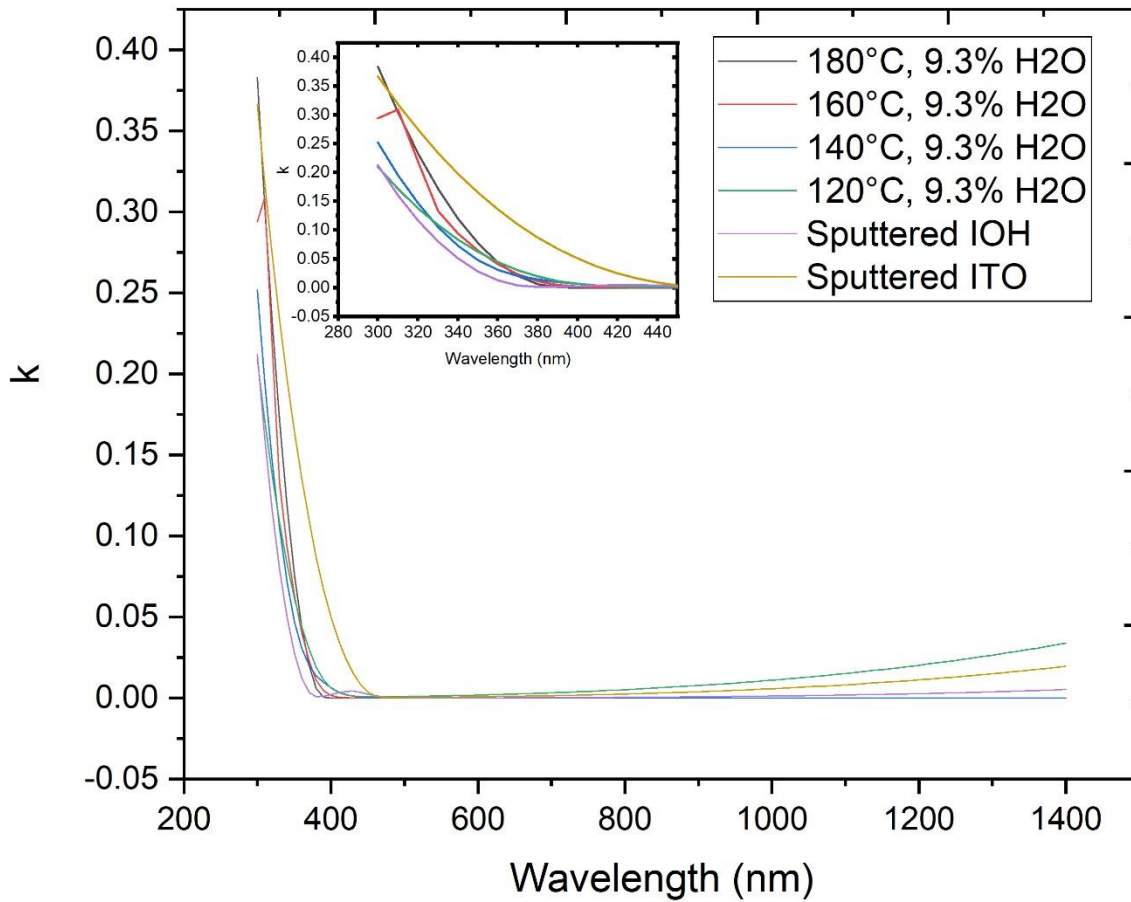


Figure 39 Extinction coefficient (k) vs wavelength for 9.3% [H<sub>2</sub>O] Identical process conditions as Figure 35

Figure 39 shows the extinction coefficient (k) for the samples deposited at different reactor temperatures at 9.3% [H<sub>2</sub>O]. SCOUT software is used in order to obtain these values. Extinction coefficient k is directly related to the absorption in the material as shown in eq. 4.2. Here, alpha refers to the absorption coefficient and λ refers to the wavelength. Based on this data comments can be made on UV and near infrared absorption (FCA).

$$\alpha = \frac{4\pi k}{\lambda} \tag{4.2}$$

From Figure 39, it can be observed that sputtered ITO displays the highest UV and near infrared absorption due to the high charge carrier density in it as previously reported in literature [42]. Furthermore, sputtered IO:H shows the lowest UV absorption followed by samples deposited at 140 °C, 120 °C, 160 °C and 180 °C respectively. Additionally, apart from the results for the sample deposited at 120 °C, which does not follow the expected trend as it has higher free carrier absorption in the near infrared region (NIR) than the sputtered IO:H. All samples deposited at 140, 160 and 180 °C show the lowest free carrier absorption in the NIR. This is as expected as low free carrier absorption in NIR for IO:H is a well documented phenomena [25, 42]. However, any comment regarding the improvement in FCA for samples deposited at different reactor temperatures is not possible from these results. Hence, due to the low UV absorption and low FCA, the sample deposited at 140 °C seems to have the most optimum optical property.

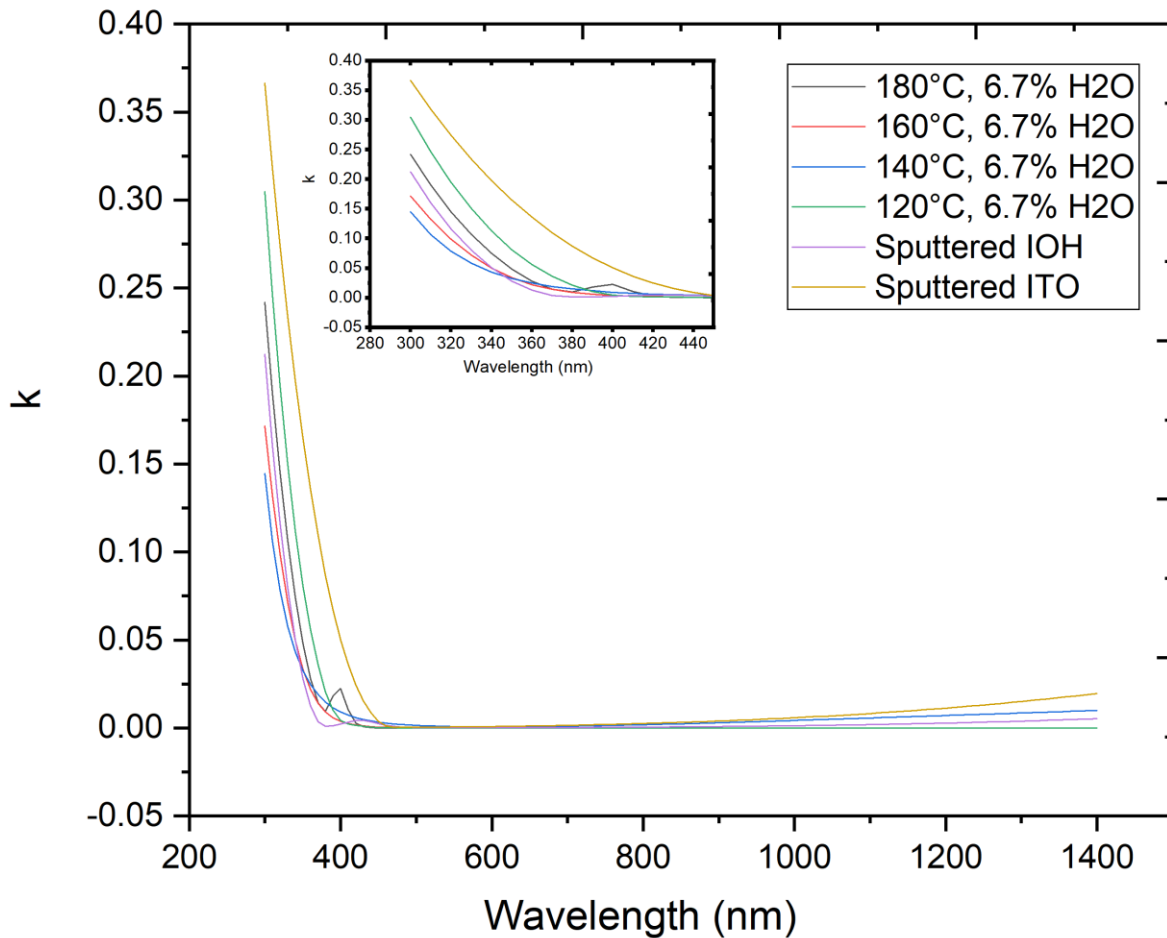


Figure 40 Extinction coefficient ( $k$ ) vs wavelength for 6.7% [H<sub>2</sub>O] Identical process conditions as Figure 35

Figure 40 depicts the extinction coefficient ( $k$ ) for the samples deposited at different reactor temperatures at 6.7% [H<sub>2</sub>O]. The highest UV and near infrared absorption of sputtered ITO is found to be consistent with the previous results. In addition to this, the lowest UV absorption is displayed by samples deposited at 140 °C, 160 °C and sputtered IO:H. Samples deposited at 180 °C and 120 °C show the highest UV absorption, amongst the samples deposited using PESALD. With regard to free carrier absorption in NIR, the lowest free carrier absorption is observed for samples deposited at 120 °C, 160 °C and 180 °C. However, for this case the sample deposited at 140 °C seems to have higher free carrier absorption which does not follow the expected trend for carrier density as observed from Figure 37. From Figure 40 and Figure 39, it can be thus inferred that better optical properties are obtained for the IO:H samples deposited using PESALD as compared to sputtered ITO. This falls in line with the literature review performed for ITO as previously stated in section 2.2.1. Furthermore, sample deposited at 140 °C for 9.3% [H<sub>2</sub>O] and sample deposited at 160 °C for 6.7% [H<sub>2</sub>O] provided the best optical properties.

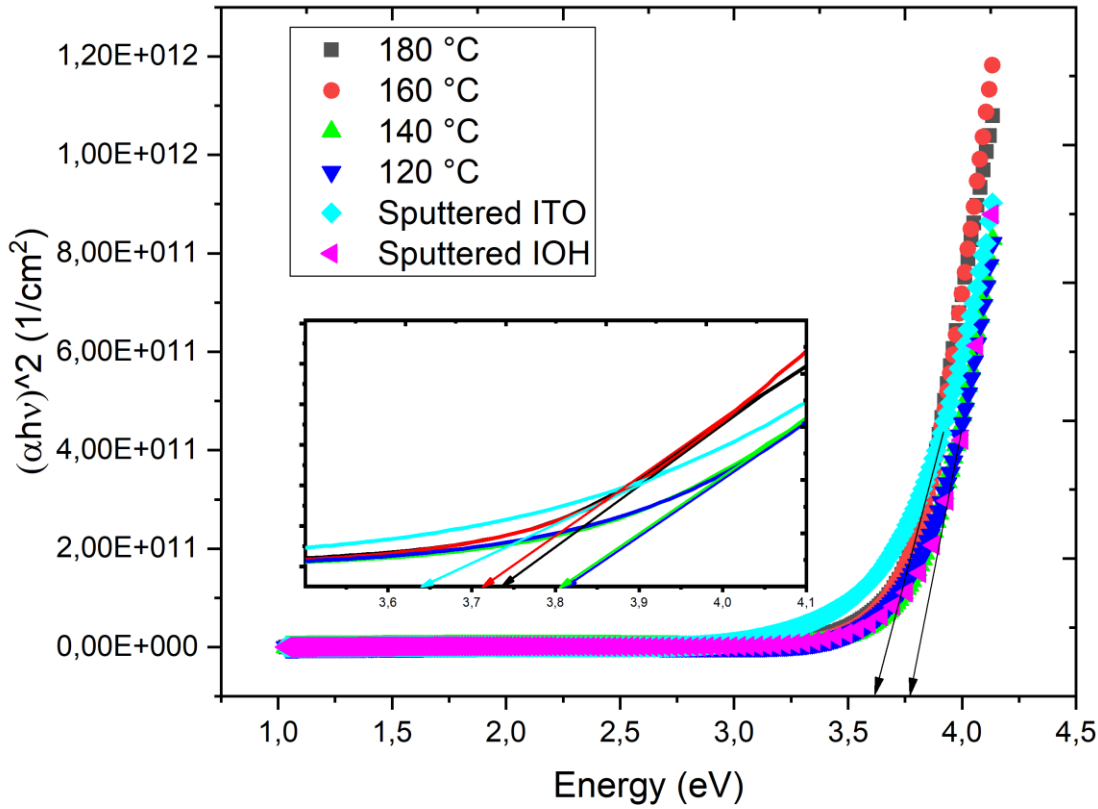


Figure 41 Tauc Plot for 9.3% [H<sub>2</sub>O]. Identical process conditions as Figure 35. Results for Sputtered IO:H is not visible in the enlarged picture due to the limited data points available for this sample.

Figure 41 shows a Tauc plot used for determining the optical bandgap ( $E_g$ ) of the layers deposited at different temperatures for 9.3% [H<sub>2</sub>O]. Eqn. 4.3 is used in order to obtain the optical bandgap. The value of the optical bandgap is obtained merely by extrapolating the linear part of the curve.

$$\alpha h\nu = A (h\nu - E_g)^m \quad (4.3)$$

Here  $h$  is the Planck's constant =  $6.63 \times 10^{-34}$  m<sup>2</sup> kg / s,  $\nu$  is the frequency at each wavelength,  $A$  is the absorption and  $m = 2$  for a direct allowed transition. Based on Figure 41, it can be deduced that the lowest optical bandgap amongst all the samples is observed for sputtered ITO (~3.65 eV). The highest optical bandgap is observed for samples deposited at 140 °C, 120 °C and sputtered IO:H (~3.8 eV). For the samples deposited at 160 °C and 180 °C, an optical bandgap in the range of (3.72-3.75 eV) has been observed. Hence, it is observed through these results that a higher optical bandgap is observed for the samples deposited at lower reactor temperatures. These results are coherent with the results for the extinction coefficient previously discussed in this section (see Figure 39). A higher UV absorption in samples is indicative of a lower optical bandgap. In addition to this, as reported in literature an increase in optical bandgap of a TCO with high bandgap ( $E_g > 3$  eV) is reported as the carrier density increases and this is attributed to the Burstein-Moss shift [22]. This effect is also confirmed as highest carrier density was reported at lowest temperatures (see Figure 37) however the reasoning remains dubious in the case of 160 °C and 180 °C. This further affirms the previous deviation in trend observed for resistivity and carrier density for the sample deposited at 180 °C for 9.3% [H<sub>2</sub>O]. The concept of the Burstein-Moss shift is elaborated in section 1.3.4. It is important to note here that the observed value of ~3.7- 3.8 eV for the optical bandgap of IO:H has been reported in literature as well [22]. Hence, the most optimum condition based on the combination of optical, growth and electrical property for 9.3% [H<sub>2</sub>O] would be of the sample deposited at 140 °C. Sample deposited at 120 °C, even though it offers good optical properties did not have appropriate electrical properties.

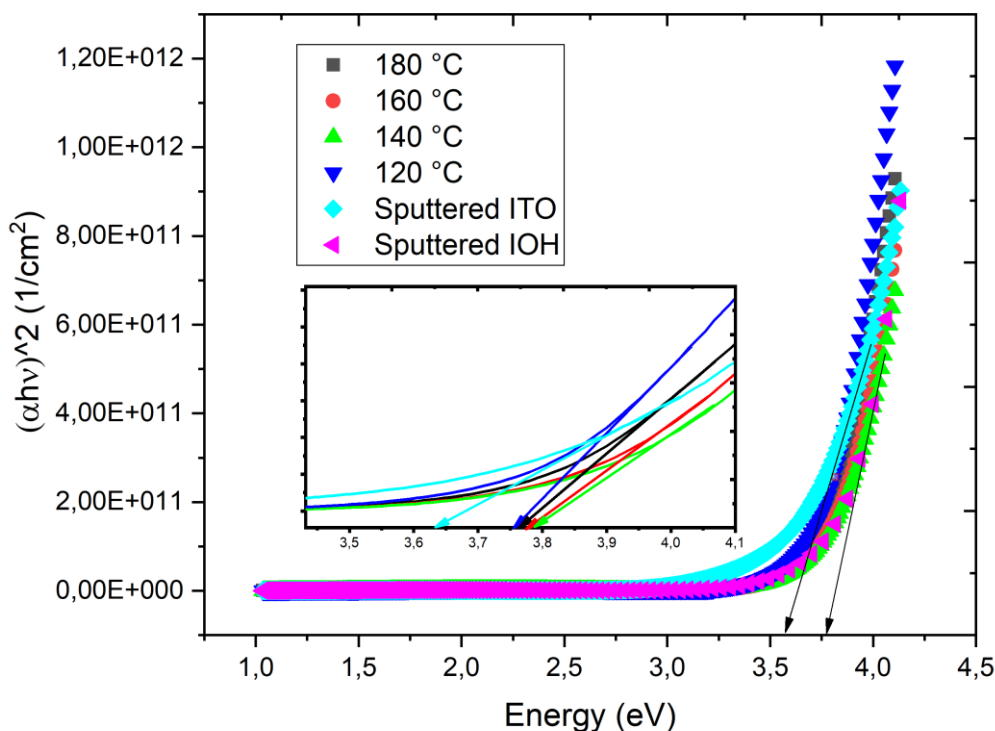


Figure 42 Tauc Plot for 6.7% [H<sub>2</sub>O]. Identical process conditions as Figure 35. Results for Sputtered IO:H is not visible in the enlarged picture due to the limited data points available for this sample.

Additionally, this analysis was also performed for 6.7% [H<sub>2</sub>O]. The Tauc plot for this case is depicted in Figure 42. The sample with the lowest optical bandgap is observed to be that of sputtered ITO, as expected. Amongst the IO:H samples, the lowest optical bandgap is observed here for the sample deposited at 120 °C (~3.75 eV) in agreement to its high UV absorption and the highest optical bandgap is observed for the sample deposited at 140 °C (~3.8 eV) in agreement to its lowest UV absorption (see Figure 40). Moreover, a slight increase in the optical bandgap for sample deposited at 180 °C (~3.75 to ~3.77 eV) and a higher increase in the optical bandgap for sample deposited at 160 °C (~3.72 to ~3.78 eV) is observed, both of these are also coherent with the results for UV absorption. The increased optical bandgap for 140 °C sample can be explained by the Burstein moss shift as high FCA was also observed for this sample. This makes this process condition not suitable for IO:H deposition. However, the expected trend relating the FCA with the optical bandgap by Burstein Moss shift is not evident for the samples deposited at 120 °C here. Hence, for 6.7% [H<sub>2</sub>O], 160 °C sample provides the most apt. process condition purely on the basis of optical properties however a high electrical resistivity was reported for this sample before, hence making it unsuitable.

Overall, by combining the net effect of growth, electrical and optical property till this point the sample deposited at 140 °C for 9.3% [H<sub>2</sub>O] could be considered the optimum condition for deposition of IO:H using PESALD. However, the sample deposited at a reactor temperature of 160 °C using 9.3% [H<sub>2</sub>O] could also be promising due to its superior mobility.

## 4.6 Structural properties

The structure of a material plays a crucial role in determining a material's electrical properties. For IO:H in particular, it has been previously reported that the crystallinity of the IO:H directly influences the electro-optical properties of the material [23]. The same samples obtained from section 4.4.4 by varying the temperature and [H<sub>2</sub>O] and which have been optically characterised in the previous section have been structurally analysed in this section. For doing so, X-ray diffraction technique is used. It should be noted that attempts were also made to perform Raman spectroscopy for the samples, however no reliable results were

obtained using this characterisation technique, possibly due to the low thickness of the samples. The results can be observed in Appendix B.6.

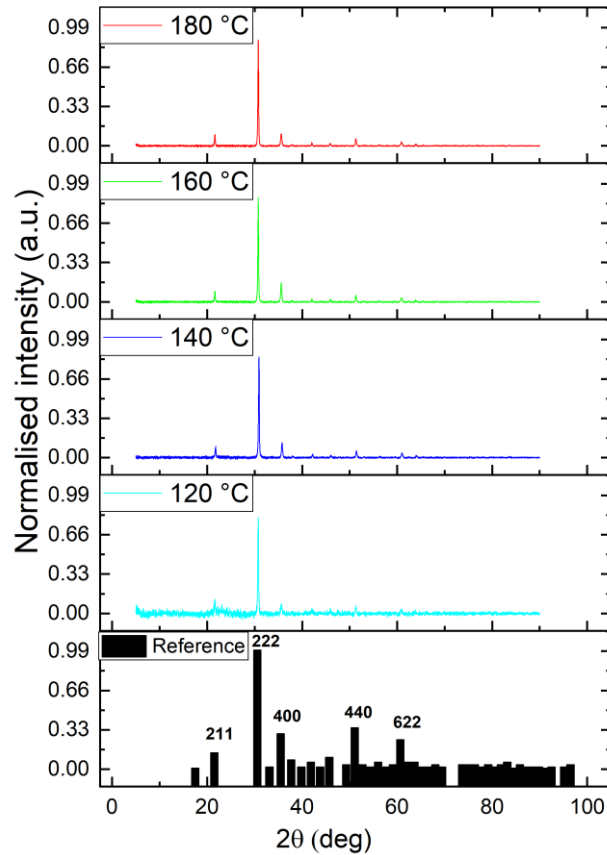


Figure 43 XRD diffractograms for PESALD IO:H for different reactor temperatures at 9.3% [H<sub>2</sub>O]. Same process conditions as Figure 35

Figure 43 depicts the XRD spectra for the samples obtained on the basis of variations made in section 4.5.4 at 9.3% [H<sub>2</sub>O]. The reference plot here shows the data for a reference sample of In<sub>2</sub>O<sub>3</sub> obtained from the software of the equipment. This is basically a powdered sample with random grain orientations with data obtained from Crystallography Open Database (COD) and card number 1010341 [85]. Based on this data, the most prominent orientation in the In<sub>2</sub>O<sub>3</sub> crystals are 222, 400, 440 and 622 which are found to be at 30°, 35°, 50° and 60° respectively. It is clear from the measured XRD spectra for the samples, that all the samples are crystalline. Even the sample deposited at the reactor temperature of 120 °C depicts the crystalline nature of the material. This is very interesting as indium oxide is known to crystallize at 140 °C [22]. Hence, the observed crystallinity in the sample can be attributed to the use of plasma in the process. Similar data is obtained for temporal ALD at deposition temperatures greater than 150 °C [23, 86] In order to analyse this data, first the preferred orientation in the layer is discovered. This is done by finding the texture coefficient of each aforementioned orientations. This is calculated using equation 4.4 [87].

$$P(h_i k_i l_i) = \frac{I(h_i k_i l_i)}{I_0(h_i k_i l_i)} \left( \sum_{i=1}^n \frac{I(h_i k_i l_i)}{I_0(h_i k_i l_i)} \right)^{-1} \quad (4.4)$$

Here  $P(hkl)$  is the texture coefficient of the plane specified by Miller Indices  $(hkl)$ ,  $I(hkl)$  and  $I_0(hkl)$  are the integrated intensity ratios at the specified miller index for the sample deposited and the measured sample.

Reactor temperature	Texture coefficient(211)	Texture coefficient (222)	Texture Coefficient (400)	Texture Coefficient (440)	Texture Coefficient (622)
180	0.28	0.35	0.21	0.09	0.08
160	0.25	0.32	0.27	0.08	0.08
140	0.26	0.35	0.22	0.08	0.09
120	0.28	0.35	0.19	0.08	0.08

Table 6 Texture coefficients for PESALD IO:H for different reactor temperatures at 9.3% [H<sub>2</sub>O]

Based on this, the orientation with the highest texture coefficient is considered the preferred orientation. The intensities were normalised to perform this analysis. As a result of which, a slight preference was found for the 222 orientation. The results for the texture coefficients are depicted in Table 6 Using this orientation, the approximate crystal size for the samples has been calculated. This is done by using equation 4.5 which is also called the Scherrer equation [88]. This equation is based on the concept that the width of a powder X-ray diffraction reflection is related to its diffraction crystal size. It should be noted that crystal size is different than particle size. As, a particle may be made up of a lot of crystallites. Furthermore, the Bragg-Brentano investigation used in this project is known to investigate crystallite sizes only through the thickness of the film. In order to know the crystallite size laterally, diffraction patterns need to be investigated at different tilts.

$$L = \frac{K\lambda}{\beta \cos \theta} \quad (4.5)$$

Here, L is the average crystal size, K is a constant (0.94) assuming spherical crystals with cubic symmetry,  $\lambda$  is the wavelength of Cu K $\alpha$  (0.154 nm),  $\beta$  is the full width at half maximum (FWHM) of the peak and  $\theta$  is the incident angle. The results of these calculations are depicted in Table 7. Recent research in this field have shown that the mobility for IO:H tends to increase with the crystal grain size [82]. In addition to this, It has also been reported previously by XRD studies that as the FWHM decreases and the crystallite size increases, the concentration of lattice imperfections also decrease, hence improving the quality of the layer [89]. In the results obtained for XRD for the IO:H deposited using PESALD, these trends have not been observed. Rather, the crystal size does not change significantly even though an increase in mobility was observed with increasing temperature as previously depicted in Figure 37. Overall, the reactor temperature does not seem to have a major influence on the structural properties of the layer.

Temperature (°C)	Peak position (2 $\theta$ )	FWHM	Crystal size (nm)
180	30.76	0.193	42.63
160	30.76	0.198	41.62
140	30.96	0.211	38.96
120	30.748	0.197	41.91

Table 7 Crystal Size of IO:H by PESALD for 9.3% [H<sub>2</sub>O]

A similar set of results have also been obtained for the samples deposited at 6.7% [H<sub>2</sub>O] as compared to the 9.7% [H<sub>2</sub>O] as shown in Figure 44. The texture coefficient for this case also showed slight preference for 222 orientation (see Appendix B.7) and not much influence in the crystal size was observed at the different reactor temperatures.

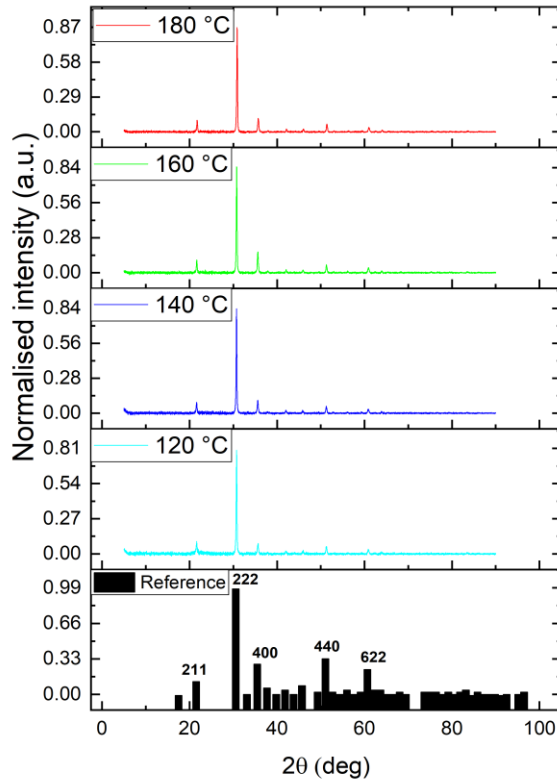


Figure 44 XRD diffractograms for PESALD IO:H for different reactor temperatures at 6.7% [H<sub>2</sub>O]. Same process conditions as Figure 35

Temperature (°C)	Peak position (2θ)	FWHM	Crystal size (nm)
180	30.08	0.217	38.13
160	30.76	0.217	37.90
140	30.72	0.209	39.40
120	30.75	0.217	37.91

Table 8 Crystal Size of IO:H by PESALD for 6.7% [H<sub>2</sub>O]

As it can be observed in Table 8 as well, temperature does not seem to have a major influence on the crystal size. However, comparing the crystal sizes at the same temperature for both 6.7% [H<sub>2</sub>O] and 9.3% [H<sub>2</sub>O] it can be observed that crystal sizes have decreased for all the reactor temperatures except 140 °C. In the case of 140 °C similar crystal sizes are observed, depicting the structural stability of the material deposited at this temperature for variable [H<sub>2</sub>O].

## 4.7 Ageing

The same samples obtained from section 4.4.4 whose optical and structural properties were presented and discussed in the previous sections are assessed on the criterion of long term stability here. Long term stability is vital for a TCO as front electrodes are crucial for optimum performance of a solar cell. This is investigated by placing the samples under damp heat (DH) conditions (85 °C, 85% relative humidity) for a duration of 900h. Sheet resistance of the samples have been measured on regular intervals in order to record the degradation of the samples.

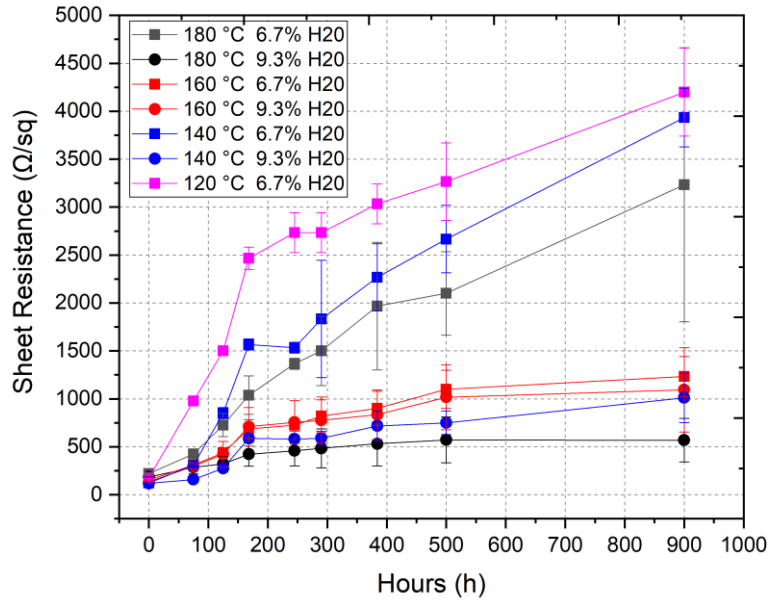


Figure 45 Degradation effect on sheet resistance under damp heat environment (85 °C & 85% relative humidity)

The degradation of the IO:H samples under damp heat conditions is presented in Figure 45, a substantial amount of degradation in the sheet resistance of the layer has been observed for all the samples. Interestingly, high stability in the layers has been observed for the samples deposited under higher [H<sub>2</sub>O] i.e. 9.3%. All samples deposited at [H<sub>2</sub>O] of 6.7% show significant degradation apart from the one deposited at 160 °C. For the samples deposited at 160 °C similar extent of degradation has been observed for both [H<sub>2</sub>O]. However, based on the results obtained the layer which seemed the most stable under DH conditions was the one deposited at 180 °C at 9.3% [H<sub>2</sub>O], followed by the one deposited at 140 °C at 9.3% [H<sub>2</sub>O].

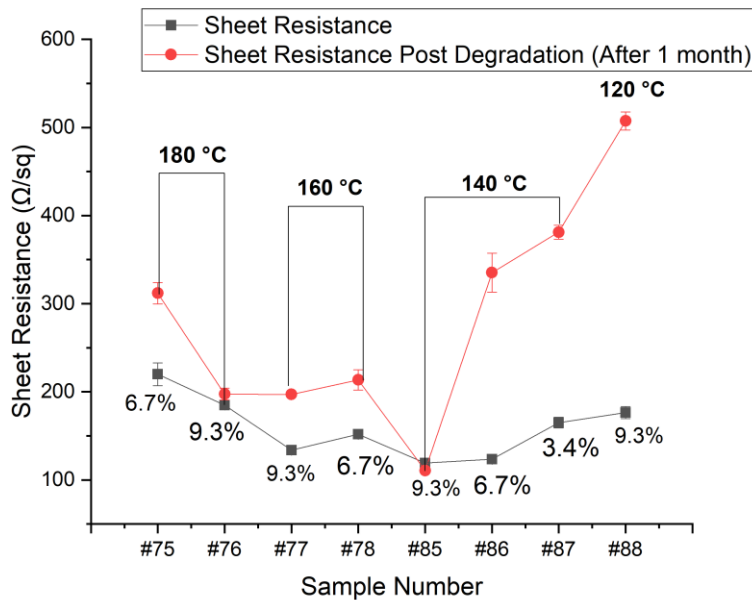


Figure 46 Degradation effect on sheet resistance under atmospheric conditions

In Figure 46, the change in sheet resistance of the samples after being exposed to atmospheric conditions for 1 month is depicted. The same trend in degradation as observed previously in Figure 45 has been noted here. It has been previously reported for other TCOs that the thickness of the TCO layers could also be playing a crucial role in its degradation [90]. The thickness of the samples is shown in Table 9. As observed in the work of Sundaramoorthy et al. the layer with a higher thickness undergoes less degradation. A similar trend is also observed for the IO:H deposited during this project. All the IO:H layers deposited at 9.3% [H<sub>2</sub>O]

tend to have a slightly higher thickness and lesser degradation as compared to the IO:H layers deposited at 6.7% [H<sub>2</sub>O]. This observation holds true for all reactor temperatures, interestingly at 160 °C where the thickness is the same for the layers deposited at both the [H<sub>2</sub>O], no major difference in degradation is observed.

In addition to this, samples were also optically examined by performing T & R measurements on them post degradation for both these cases. There was negligible change observed in the optical properties of the samples. These results are consistent with the results previously reported in literature for the damp heat tests of TCOs like ITO, IZO and IO:H [54].

Temperature (°C), [H <sub>2</sub> O]	Thickness (nm)
180, 9.3%	108
180, 6.7%	103
160, 9.3%	98
160, 6.7%	98
140, 9.3%	93
140, 6.7%	88
120, 6.7%	95

*Table 9 Thickness of the samples before degradation*

In order to get further insight, XRD was performed for the samples subjected to 900h of damp heat conditions. The mean size of crystals and FWHM at the preferred orientation of (222) were calculated on the basis of these measurements. These results were then compared with the results previously discussed in section 4.6 without placing the samples in the damp heat chamber. These results are summarized in Table 10. Here, no major changes in the structural property of the layers has been observed apart from the layer deposited at 180 °C and 9.3 % [H<sub>2</sub>O]. This is the same sample for which a deviation in trend was observed for the resistivity, carrier density and optical bandgap. Overall, the negligible effect on the structural property for IO:H when subjected to damp heat conditions is an expected result and has been documented before. This indicates that the adsorbed H<sub>2</sub>O related species through the damp heat chamber do not result in degrading the crystallinity of the film [54].

Temperature (°C), [H <sub>2</sub> O]	Mean Size 222 (nm)	Mean Size 222 after DH(nm)	FWHM 222	FWHM 222 after DH
180, 9.3%	42.63	38.04	0.193	0.217
180, 6.7%	38.13	38.03	0.217	0.211
160, 9.3%	41.62	36.62	0.198	0.224
160, 6.7%	37.89	37.97	0.217	0.221
140, 9.3%	38.95	38.21	0.212	0.215
140, 6.7%	39.40	37.23	0.209	0.217
120, 9.3%	41.91	NA	0.197	NA
120, 6.7%	37.9	38.97	0.217	0.217

*Table 10 Change in structural properties of the samples after being subjected to damp heat environment (85 °C & 85% relative humidity)*

Summarizing the results for ageing, it can be said that 9.3% [H<sub>2</sub>O] has resulted in a more stable layer for all the reactor temperatures. It is interesting to note that the nature of the layer deposited at 180 °C remains unclear due to the change observed for its crystal size. Hence, based on the aforementioned results 140 °C and 160 °C deposited at 9.3% [H<sub>2</sub>O] can be regarded as the optimum conditions.

## 4.8 Conclusion & recommendations

In this chapter, an investigation to obtain the process parameters for depositing IO:H using PESALD has been performed. The ellipsometer, 4 point probe and hall measurement setup are used primarily to perform a growth and electrical analysis and the following results are obtained.

1. The sensitivity of the process is first discussed and the issue of the lack of reproducibility possibly due to oxygen contamination or contamination of the gas flow lines is put forth.
2. In order to systematically perform the process development, firstly, the pickup flow for the novel DADI metal precursor has been determined. DADI as the metal precursor in this process has improved the overall stability of the system as compared to previously used TMI due to its lower reactivity. Based on the growth and electrical analysis, 0.5 slm is found to be the sufficient DADI precursor dose. Interestingly, growth analysis showed comparable values for GPC at relatively lower reactor temperature (120 °C) for DADI precursor using ALD due to the incorporation of plasma in the process. However, it would be interesting to further investigate the improved conductivity observed at when precursor pickup flow of 0.7 slm was used by performing a compositional analysis of the layer.
3. Similar methodology as for the metal precursor is used to obtain the sufficient H<sub>2</sub> concentration in the plasma. A [H<sub>2</sub>] of 39% i.e the highest possible, keeping safety of the system in mind is set to be the apt [H<sub>2</sub>] for this process. It is hypothesized that such high [H<sub>2</sub>] is used to scavenge the oxygen in the system, keeping in mind that the PESALD process is operated under atmospheric conditions.
4. By the same method, the rotation frequency of the substrate is obtained. No saturation in growth is observed even at high exposure times, hence discarding the possibility of etching effect by H<sub>2</sub>. A rotation frequency of 30 RPM is considered suitable for this process, however a discrepancy in the resistivity measured using the hall measurement setup and the combined results of the 4 point probe and the ellipsometer is observed for the results obtained at the rotation frequency of 50 RPM. It is recommended to further investigate this data point to be certain of the choice here.

Establishing the aforementioned parameters, an intensive analysis was performed based on electrical, optical, structural and ageing properties of the layer to obtain the suitable reactor temperature and [H<sub>2</sub>O] for the process. The results are summarised as follows.

1. Growth analysis showed 120-160 °C as the ALD temperature window. The high GPC observed at 180 °C could be due to soot formation or recombination of radicals in the plasma. It would be recommended to perform a compositional analysis like elastic recoil detection (ERD) or X-ray photoelectron spectroscopy (XPS) on the layers to confirm the hypothesis.
2. Electrical analysis showed highest conductivity at temperature of 140 °C and 160 °C. Conductivity is independent of [H<sub>2</sub>O] when deposition takes place at 140 °C and is dependent on [H<sub>2</sub>O] when deposition takes place at 160 °C, higher conductivity for sample deposited at 9.3% [H<sub>2</sub>O]. A higher mobility is observed for the samples deposited at 160 °C as compared to 140 °C. Hence, making the process condition involving a reactor temperature of 160 °C at 9.3% [H<sub>2</sub>O] the most optimum, followed by condition with reactor temperature of 140 °C at 9.3% [H<sub>2</sub>O] and 6.7% [H<sub>2</sub>O] due to the unprecedented low resistivity observed for these conditions. Additionally, highest mobility has been demonstrated at 180 °C but a high resistivity is observed. Hence, it is recommended to check the reproducibility of the result obtained for a reactor temperature of 180 °C.
3. Improved optical bandgap, low FCA and decreased UV absorption for 140 °C as compared to 160 °C at 9.3% [H<sub>2</sub>O]. For sample deposited on 160 °C at 9.3% [H<sub>2</sub>O], a higher UV absorption and hence a lower optical bandgap is observed. However, transmittance and reflectance of the layers remain independent of different [H<sub>2</sub>O] at any reactor temperature. Overall, an average transmittance of ~80% has been observed for all the samples independent of temperature and [H<sub>2</sub>O].
4. Structural analysis confirm crystallinity in all the deposited layers however structural properties remain uninfluenced by variable reactor temperature and [H<sub>2</sub>O].
5. Effect of ageing under DH conditions and atmospheric conditions has clearly depicted reduced degradation for samples deposited at 9.3% [H<sub>2</sub>O] as compared to 6.3% [H<sub>2</sub>O]. The ageing effect for sample deposited at a reactor temperature of 160 °C remains uninfluenced by [H<sub>2</sub>O] possibly due to similarity in thickness. Overall, similar and reduced level of degradation for both samples deposited with 9.3% [H<sub>2</sub>O] at 140 °C and 160 °C respectively has been observed.

Hence, based on the aforementioned results for growth, electrical, optical, structural and ageing properties, the most optimum conditions in order to apply the IO:H layer on a CIGS solar cell is considered to be the one with the reactor temperature of 140 °C and 160 °C at 9.3% [H<sub>2</sub>O].

# 5 IO:H as TCO on CIGS solar cells

In this chapter, the most optimum conditions for depositing IO:H using PESALD as obtained from chapter 4 are used to demonstrate a PV application of the process. CIGS is used as the absorber layer in the PV architecture for demonstrating this application. The chapter begins with elaborating on to the methodology of performing the experiments. This is followed by analysing and discussing the performance of the cells obtained by using this process. The performance is compared with that of reference cells on which aluminium doped zinc oxide (AZO) is used as the TCO.

The main objective of these experiments has been to investigate the applicability of the PESALD process for IO:H deposition on a CIGS solar cells and to compare its performance with reference CIGS solar cells on which AZO is used as the TCO. Additionally since, the thermal budget of the CIGS solar cell under such conditions has not been previously investigated, it is interesting to see how the cells would perform under such conditions. Finally, as it has been previously stated the ALD process has been successfully used to deposit the buffer layer, hence if the TCO layer could also be successfully deposited using the same process it would significantly increase the applicability of the process.

The research question related to the application of the IO:H developed by PESALD on CIGS solar cells is discussed and answered in this part of the report. The research question answered here is the following.

1. How does the IO:H layer perform on a CIGS solar cell?

## 5.1 Methodology

Based on the results obtained from chapter 4, two process conditions seemed appropriate to perform the deposition of IO:H on CIGS solar cells. The conditions are show in Table 11.

Process Parameter	Condition 1	Condition 2
DADI precursor pickup flow (slm)	0.5	0.5
Plasma down flow (slm)	5	5
Plasma top flow (slm)	2	2
H <sub>2</sub> [%]	39	39
H <sub>2</sub> O [%]	9.3	9.3
RPM	30	30
No. of cycles	4000	4000
Reactor temperature (°C)	<b>140</b>	<b>160</b>
Plasma Voltage (kV)	5.2	5.2
Plasma repetition rate (kHz)	66.7	66.7

Table 11 Process conditions for deposition on CIGS solar cells

The same process parameters as used in section 4.4.4 have been used here to perform the deposition, following the same line of thought. Based on the results of the growth, electrical, optical, structural and ageing properties, 9.3% [H<sub>2</sub>O] and two reactor temperatures, 140 °C and 160 °C are considered suitable to perform the deposition. It is important to note that the experiments are performed here using 4000 cycles as compared to 2400 cycles previously used for performing the deposition. This is done in order to deposit a thicker layer. For suitable conductivity of TCO on CIGS solar cells, it was suggested that a sheet resistance of 50-60 Ω/sq

must be ensured. Using equation 1.9, this could be done by depositing a thicker layer of IO:H. Hence, the number of cycles were increased. This resulted in an increase in thickness from a range of ~90 -120 nm to ~140-170 nm.



*Figure 47 Sample holder used to perform deposition of IO:H on CIGS solar cells*

Figure 47 depicts the sample holder used to perform the deposition. This sample holder is used as each CIGS solar cell is deposited on a 30x30x1.1 mm soda lime glass samples. Soda lime glass is used here as the glass substrate to deposit the CIGS because Na diffusion from the substrate plays a vital role in forming a uniform CIGS film [91]. The pockets in which the CIGS samples are placed, as shown in Figure 47 are 1.3 mm deep, as a result of which in order to perform the deposition on the 1.1 mm thick surface a 0.2 mm spacer is required. The role of a spacer is performed by simply sticking a double layered Kapton tape of 0.1mm thickness on the back of the cell. There was a significant improvement in the electrical and growth properties in the layers deposited when the tape was used, as compared to the case when the deposition was performed without any tape. Hence, all the depositions were performed by double coating the rear side of the cell with the tape. Ideally, each pocket is exactly identical to the other and hence, it should not have any influence on the layer properties. However, some differences in layer properties have still been observed. The sample size of the experiments is not large enough to make a concrete comment on this issue, as a result of which the best results have been presented in this chapter.

Firstly, experiments were conducted to check if the results obtained previously by using the proposed conditions could be reproduced by using the aforementioned setup. Depositions were performed on soda lime glass substrates and their growth and electrical properties were investigated. This was essential to do as the thickness of the layers had also been altered for these set of experiments. Based on the results obtained here, the condition by which the results could be reproduced was chosen to perform the deposition on the CIGS solar cells.

Affirming the apt. conditions for deposition on to 30x30mm soda lime glasses, IO:H on CIGS solar cells using PESALD was deposited. The experiments on the CIGS solar cells were performed in two batches. Each batch is symbolic of a set of CIGS solar cells prepared under identical conditions. Out of the two batches, first batch of CIGS solar cells due to uncontrollable circumstances (technical difficulties) were exposed to atmospheric

conditions before CdS, i-ZnO and the TCO layer was deposited on it, which resulted in their degradation. The deposition on the second batch was performed instantly after the sample was prepared and high performing CIGS solar cells were obtained. The performance of the cells was then characterised using J-V measurements. This was followed by measuring the external quantum efficiency (EQE) of the best cell on the sample.

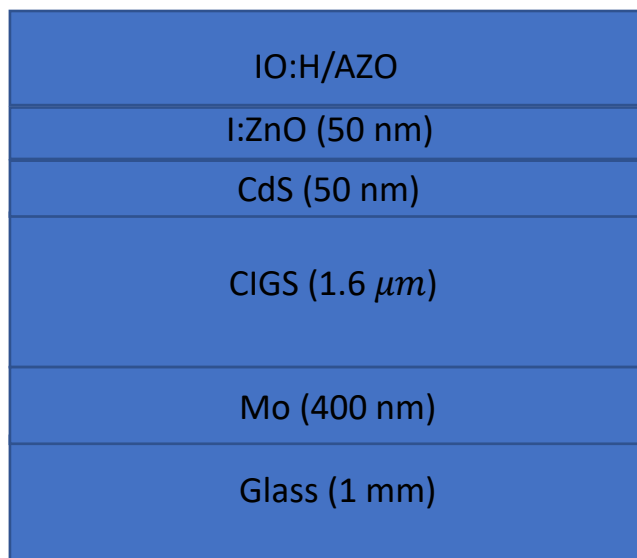


Figure 48 CIGS solar cell architecture

Figure 48 depicts the architecture of the  $\text{CuInGaSe}_2$  solar cell that has been used in this project. The stack made at TNO, Solliance, investigated here comprises of soda lime glass/molybdenum (Mo)/CIGS/cadmium sulphide (CdS)/intrinsic zinc oxide (i:ZnO)/TCO. The CIGS absorber has been deposited by using a two step or co-evaporation process on to the molybdenum coated soda lime glass substrate. It has been seen here that a higher temperature during deposition of CIGS has resulted in a better quality CIGS absorber layer. However, the bottleneck here is the melting temperature of the glass substrate. Additionally, the molybdenum and intrinsic zinc oxide are deposited by using sputtering whereas chemical bath deposition technique is used to deposit the buffer layer of CdS. For the TCO layer in the reference cells, a standard 270 nm layer of AZO as TCO is deposited using sputtering. After depositing the TCO by PESALD and sputtering for IO:H and AZO samples respectively, the metal contact is scribed on to the samples. The final solar cell is depicted in Figure 49. There are 9 samples depicted here and each sample has approximately 14 cells or 14 different points of measurements.

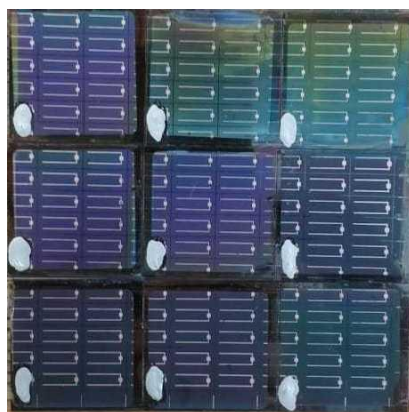


Figure 49 6 samples of CIGS solar cells

## 5.2 Reproducibility test

Soda lime glass substrates in the sample holder were first subjected to the two possible conditions enlisted in Table 11 for IO:H depositions. In the 1<sup>st</sup> condition, IO:H was deposited at 140 °C and in the 2<sup>nd</sup> condition, IO:H was deposited at 160 °C, keeping water concentration at 9.3% H<sub>2</sub>O and all other parameters were kept identical to the process conditions set at section 4.4.4. This was done in order to ensure that a reproducible result was produced. Moreover, the thickness of the sample was also increased as compared to the previously obtained result here hence it was important to check if this could have an influence on the growth or electrical property of the layer.

	<b>Resistivity (mΩcm)</b>	<b>Mobility (cm<sup>2</sup>/Vs)</b>	<b>Carrier Density (1E20 cm<sup>-3</sup>)</b>	<b>GPC (nm/cycle)</b>
140 °C (before)	1.12	30.9	1	0.039
140 °C (after)	1.2	42.3	1.11	0.035

*Table 12 Reproducibility test for Condition 1*

Table 12 displays the result for the tests performed at a reactor temperature of 140 °C. The result stating “140 °C before” is the one that has been already shown and discussed in section 4.4.4 whereas the result stating “140 °C after” is the new result obtained by performing the deposition on a soda lime glass using the sample holder. It can be observed here that using condition 1, an almost identical result with an improved mobility was obtained. This furthermore supports the argument that this condition is one of the most optimum condition for performing IO:H depositions using PESALD. This result is particularly interesting as it further affirms the unprecedented successful deposition of IO:H by PESALD at a relatively lower reactor temperature of 140 °C.

	<b>Resistivity (mΩcm)</b>	<b>Mobility (cm<sup>2</sup>/Vs)</b>	<b>Carrier Density (1E20 cm<sup>-3</sup>)</b>	<b>GPC</b>
160 °C (before)	1.21	67.0	0.6	0.038
160 °C (after)	2.05	49.1	0.595	0.039

*Table 13 Reproducibility test for Condition 2*

Following the same thought process as just stated, reproducibility tests were carried out at a reactor temperature of 160 °C. Table 13 shows the corresponding results that were obtained from these experiments. It can be clearly observed that the resistivity increased by a factor of 2 and mobility decreased significantly when the experiment was performed using the substrate holder. It can be clearly observed here that the results could not be reproduced for this condition. It is important to note that multiple experiments were performed before getting the results for condition 1 and condition 2, in order to ensure that the contamination of lines did not play a role in determining these results. Hence, based on the aforementioned results it has been decided to use condition 1 for performing IO:H depositions on CIGS solar cells.

## 5.3 Motivation

The motivation to deposit IO:H on CIGS solar cells had been previously discussed briefly in section 2.3. In order to perform the experiments, there were certain requirements that the TCO layer of IO:H needed to oblige to, in order to be suitable for a successful application. One of them being the band alignment of IO:H with the intrinsic zinc oxide (i-ZnO) layer. This prerequisite has been met via literature study. It has been reported in literature that IO:H and i-ZnO have a suitable band line up [92].

Another important requirement is the thermal stability of the CIGS solar cells, as during these experiments the cells would be exposed to a reactor temperature of 140 °C for a duration of 105 mins. Comparisons have been drawn from experiments in which a post deposition annealing step is performed in order to crystallise the IO:H on CIGS. From the work of Keller et al. [53] in which the CIGS solar cell is annealed at 200 °C for a duration of 1 h, no negative effect on the performance of the cell is reported. Furthermore, It has been reported that CIGS samples when heated upto 360 °C for 30 min did not show any changes in its external quantum efficiency [93]. In Figure 50, an accumulation of the literature data of CIGS solar cells data exposed to different temperature conditions in atmospheric air is shown [94]. It can be seen in the figure that at low temperatures (<180 °C) and low exposure times (<4 mins) the performance of the CIGS solar cells is improved by 15%. The critical temperature based on this analysis is found to be around 250 °C when the CIGS is exposed for is atleast 300 seconds [94]. However, the condition at which the CIGS solar cells are exposed to for the deposition of IO:H by PESALD is not depicted in this figure. Following this trend, it could be expected that an exposure of 105 mins at 140 °C might have some negative influence on the efficiency of the CIGS solar cells. Based on all the aforementioned results and conclusions, it seems interesting to see the influence of this thermal budget on the performance of the CIGS solar cells.

Additionally, in comparison to the solar cells where commonly used AZO is used as the TCO, using IO:H deposited by sputtering as the TCO has shown to enhance the  $V_{oc}$  by 20 mV by Jager et al [95]. This effect has shown to be reproducible for a wide range of thicknesses and is attributed to the interface properties of the i-ZnO and the TCO layer. A higher work function of IO:H and a lower bombardment of high energy ions during the sputter deposition of IO:H are other possible reasons attributed to the improved performance [95].

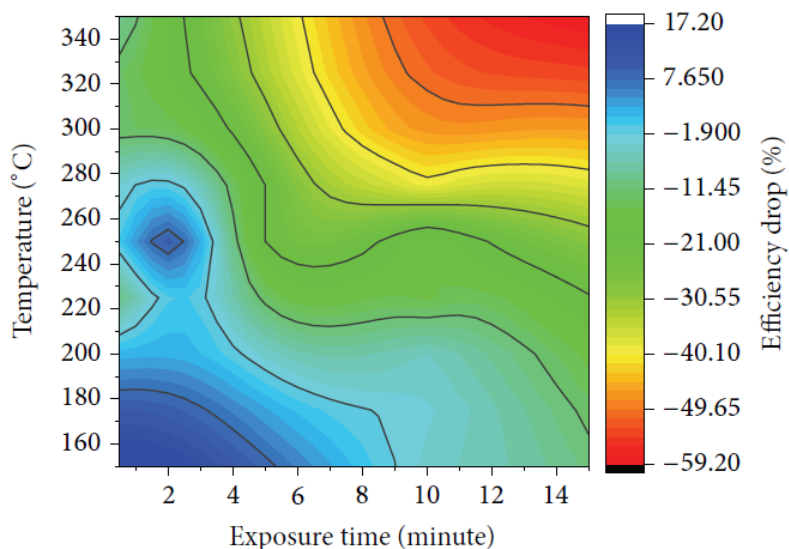


Figure 50 Effects on efficiency of CIGS solar cells for different heat treatment conditions as a function of temperature and time [93, 94, 96-100]

## 5.4 Performance of CIGS solar cells

Based on the optimum conditions, IO:H was deposited as a front TCO for CIGS solar cells using PESALD. All the results are obtained here, using identical process parameters i.e. condition 1 as elaborated in section 5.1. Each number mentioned here like #99, #100 #101 and #104 refers to one 30x30 mm sample of CIGS solar cell as depicted in Figure 49. Each sample has 14 cells on it, hence corresponding to 14 points on which measurements can be made. In order to show the variation of these measurements, box plots are used. It is important to note here that measurements in which fill factor was observed to be less than 50% and shunt resistance ( $R_{shunt}$ ) was less than 50  $\Omega$  were discarded as such results are illogical for a solar cell. The performance of the cells was characterised using a manual illuminated J-V measurement technique.

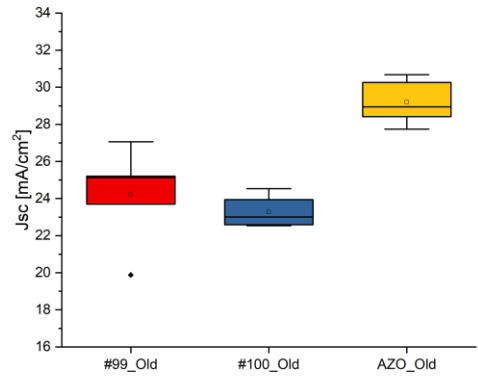
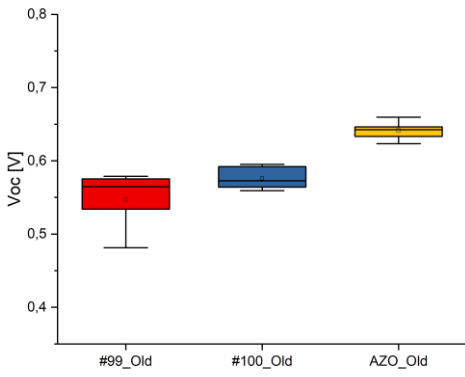
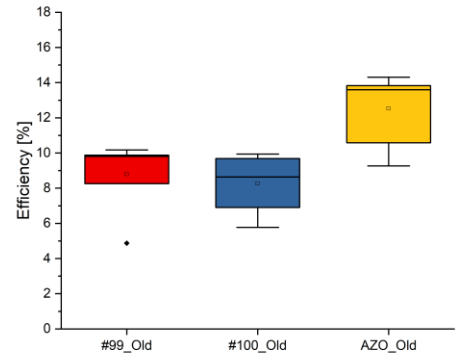
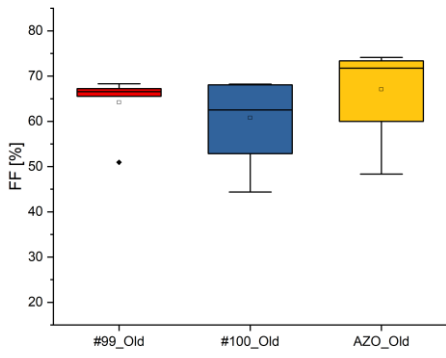


Figure 51 J-V characteristics for old batch samples

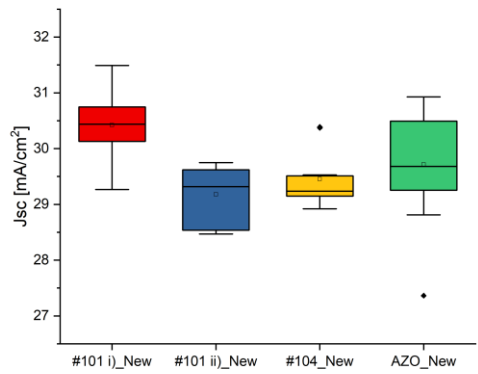
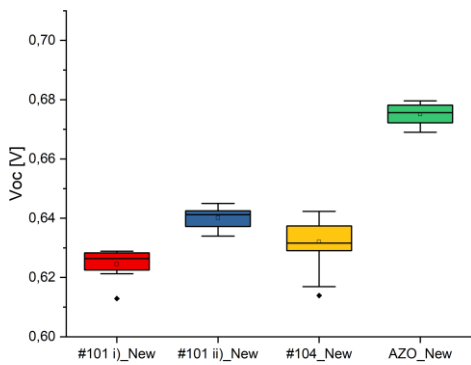
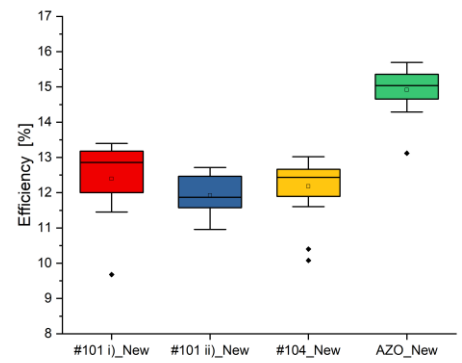
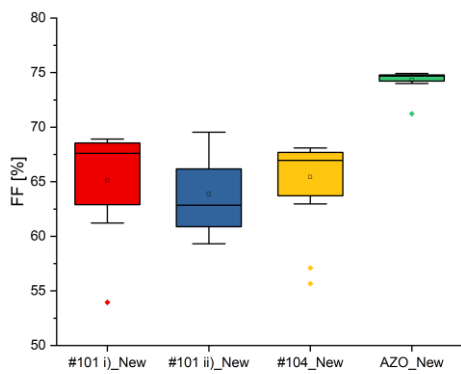


Figure 52 J-V characteristics for new batch samples

In Figure 51 and Figure 52, the fill factor (FF), efficiency, open circuit voltage ( $V_{oc}$ ) and short circuit current density ( $J_{sc}$ ) are shown for the old and new batches of CIGS solar cells. For the old batch, the samples on which IO:H as TCO is deposited using PESALD are depicted by “#99\_Old” and “#100\_ Old”. The reference sample with the sputtered AZO in the old batch is depicted by AZO\_Old. Similarly for the new batch, the samples on which IO:H as TCO is deposited using PESALD are depicted by “#101 i)\_New”, “#101\_ ii)\_New” and “#104\_New”. The reference sample with the sputtered AZO in the new batch is depicted by AZO\_New. A different number is used for each sample, as IO:H was deposited using PESALD in a different experiment for each of these samples. It is important to note here that “#101 i)\_New”, “#101\_ ii)\_New” means that IO:H was deposited in the same experiment on the CIGS samples. This was done by simultaneously placing two 30x30 mm CIGS samples in two pockets of the sample holder.

As mentioned previously in section 5.1, the samples prepared in the old batch were exposed to atmospheric conditions before the CdS, i-ZnO and the TCO layer were deposited on them. This resulted in a substantial decline in the performance of these samples. The difference in performance of the samples of both the batches is evident from Figure 51 and Figure 52. This decline is observed for all the performance parameters and is independent of the TCO used. In both the batches however, the performance of the solar cells deposited with reference AZO as TCO by sputtering appears to be better than the samples deposited with IO:H by PESALD. Overall, as expected since the same condition is used for performing all the experiments a consistency in the performance parameters of the IO:H samples is observed for both the batches. However, it is important to note that samples “#101 i)\_New” and “#101\_ ii)\_New” are prepared in the same experiment, still a difference in their performances is observed. A lower  $V_{oc}$ , higher  $J_{sc}$  and higher FF is observed for #101\_i) new as compared to #101\_ii) new. This could be attributed to either inconsistency in the quality of CIGS samples or to the sensitivity of the PESALD process.

Sample	$J_{sc}$ [mA/cm <sup>2</sup> ]	Voc [V]	FF [%]	Rseries [Ω]	Rshunt [Ω]	Efficiency [%]
#99_Old	25.12	0.58	68.33	5.93	5459.6	9.87
#100_Old	23.91	0.59	68.25	6.59	3584.9	9.69
AZO_Old	30.44	0.64	73.07	4.1	2718	14.31

Table 14 J-V characteristics for the best cells of the old batch samples

Sample	$J_{sc}$ [mA/cm <sup>2</sup> ]	Voc [V]	FF [%]	Rseries [Ω]	Rshunt [Ω]	Efficiency [%]
#101 i)_New	30.46	0.63	68.92	5.32	2392.4	13.18
#101 ii)_New	28.54	0.64	69.54	5.43	3238	12.72
#104_New	29.19	0.64	67.95	5.49	1158.8	12.73
AZO_New	29.66	0.68	74.73	4.67	7692.7	15.06

Table 15 J-V characteristics for the best cells of the new batch samples

In order to draw clear conclusions, the results for the best cells on each samples are depicted in Table 14 and Table 15 for old and new batch respectively. For the old batch, these results also confirm the degradation of the samples due to their atmospheric exposure. The degradation effects are more profound for the samples

with IO:H as compared to the #Old-AZO sample. For the new batch samples, a clear improvement in performance can be observed. The efficiency of the samples with IO:H increases from ~9.7% to ~12.7% and for samples with AZO, it increases from ~14.3% to ~15%.

It can be clearly seen from Table 15 that a lower FF is observed for the samples deposited with IO:H. A FF of ~75% is observed for the sample on which AZO is sputtered as compared to the 68-69% FF observed for IO:H samples. A low FF in this case can be attributed to the corresponding low shunt resistance and high series resistance. For a cell to perform well, its shunt resistance should be high and its series resistance should be low. This is so because shunt resistance act as a resistance to the recombination pathways and series resistance act as a resistance to the charge carriers that are to be collected on the electrode. A low shunt resistance ( $R_{shunt}$ ) of 1.2-3.2 k $\Omega$  as compared to 7.7 k $\Omega$  in this case is observed, this could be due to the high thermal budget, which the CIGS solar cell is subjected to while IO:H is deposited on it. Furthermore, high series resistance ( $R_{series}$ ) could be attributed to the high sheet resistance of IO:H deposited by PESALD. These results match with the efficiency drop that was expected on the basis of Figure 50. It has also been reported that CIGS solar cells using CdS as buffer layers undergo degradation after annealing at temperatures above 200 °C. This is attributed to the diffusion of Cd into the absorber layer of the solar cell. This could be one of the factors playing a role here, resulting in the decline in performance [99]. Moreover, the relatively lower  $V_{OC}$  of samples deposited with IO:H could be due to the diffusion of thermally activated elements in the CIGS. Such an effect has also been reported in the work of Wi et al., where a post annealing treatment of CIGS solar cells is performed in vacuum at temperature from 300-500 °C for a duration of 60 min. The rearrangement of atoms observed has been attributed to modify the local energy band gap and band alignment at the interface, resulting in decreased  $V_{OC}$ . Comparable thermal budget is used in the experiments for depositing IO:H using PESALD process on to the CIGS solar cells. However, a sputtered layer of ZN(O,S) buffer layer was used in the work of Wi et al, hence making it tough to compare the CIGS solar cells [101].

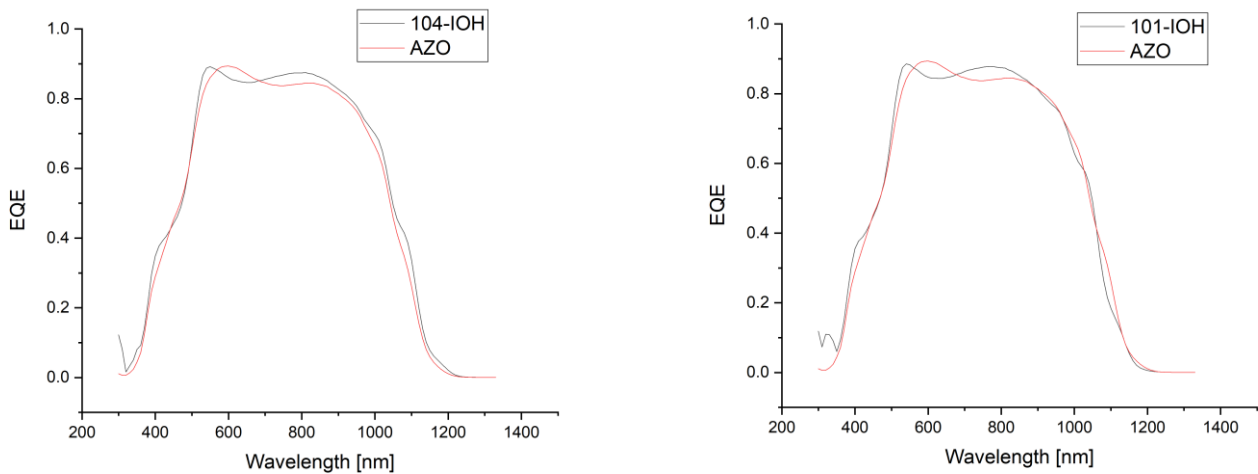


Figure 53 External quantum efficiency of IO:H samples compared to reference AZO for the new batch

Figure 53 depicts the results for the external quantum efficiencies (EQE) of the samples of IO:H compared with the reference AZO sample. Based on the superior results of the J-V characteristics, only the results from the samples of the new batch are shown here. These results are obtained for the best cell of each sample. Furthermore, 101-IOH here refers to the “101 i)\_New” sample, this sample was chosen over the “101 ii)\_New” sample. Overall, comparable EQE results are obtained for the IO:H samples as compared to the reference AZO. IO:H is known to have a high bandgap and low FCA in NIR, which should result in improved EQE [23]. However, contrary to what is expected no significant improvement for the EQE response in UV and NIR can be observed for IO:H samples as compared to the reference AZO sample in Figure 53. This indicates that the PESALD process needs to be further optimized to improve the quality of the IO:H deposited. The sudden change in EQE for the IO:H as compared to AZO here depict interference effects, showing a scope of improvement in the EQE response by optimizing the thickness of the IO:H layer deposited. Additionally, attempts were made to perform reflectance measurements on the surface of the samples in order to know the losses incurred in EQE for the samples due to reflectance but due to the small cell size (0.5 mm<sup>2</sup>) it was difficult to perform correct measurements.

	<b>104-IO:H</b>	<b>101-IO:H</b>	<b>AZO</b>
Jsc from IV (mA/cm <sup>2</sup> )	29.18	30.46	29.66
Jsc from EQE (mA/cm <sup>2</sup> )	32.74	32.14	31.9
Efficiency old (%)	12.73	13.18	15.1
Efficiency new (%)	14.28	13.91	16.2

*Table 16 Jsc measurements and efficiency correction using EQE measurement*

The  $J_{SC}$  obtained using illuminated J-V measurement cannot be entirely trusted as it might overestimate or underestimate the current. This could be due to the shading of the cell by the probe, resulting in the reduction of the total current or due to the fluctuation of the lamp used for J-V measurement. Hence, the area under the EQE curve is evaluated and correct  $J_{SC}$  is obtained. Using these corrected  $J_{SC}$ , efficiencies of the cells are recalculated. As it can be observed in Table 16, the  $J_{SC}$  for each sample were underestimated by the illuminated J-V measurement technique. Using the corrected values resulted in improved efficiencies for each of the cell. It can be concluded that similar or slightly higher  $J_{SC}$  is obtained using IO:H as TCO as compared to sputtered AZO. This is extremely motivating as this was the first time IO:H was deposited on CIGS solar cells using PESALD. Overall, an efficiency of 16.2% for the sputtered AZO cell as compared to ~14.3% and ~13.9% for the best IO:H cells has been observed. The decline in efficiency for the IO:H samples could be attributed to the high thermal budget, the CIGS solar cells are subjected to while IO:H is deposited onto them. A summary of literature studies based on this effect was previously depicted in Figure 50.

## 5.5 Conclusion & recommendations

In this chapter, the optimum conditions to deposit IO:H using PESALD as investigated in chapter 4 are applied on a CIGS solar cell. Firstly, attempts are made to reproduce the desired electrical properties as previously obtained using these conditions. Since, the desired electrical properties could only be reproduced for the sample deposited at the reactor temperature of 140 °C, this condition was solely utilized to perform TCO deposition using PESALD on the CIGS solar cell. These results were compared with those of reference CIGS solar cells where commonly used AZO was used as TCO. These solar cells were characterised using manual illuminated J-V and EQE measurements and the following results were obtained.

1. It has been shown that a successful demonstration of IO:H as a TCO using PESALD on CIGS solar cells is possible.
2. A better performance for the samples with sputtered AZO as TCO in terms of J-V characteristics and EQE however is observed as compared to samples with IO:H as TCO. This is contrary to what was expected, as IO:H is known to reduce FCA in NIR and have a higher optical bandgap as compared to AZO. The reduction in cell performance may be attributed to the high thermal budget the CIGS solar cell was subjected to in order to deposit IO:H using PESALD.
3. Similar  $J_{SC}$  are obtained for the samples deposited with IO:H as compared to the samples deposited with sputtered AZO. This is quite motivating as these are the first set of experiments ever performed to deposit IO:H using PESALD on CIGS solar cells.
4. The EQE spectra for the cell with IOH suggest interference effects which could be curbed down by optimising the thickness.
5. It would also be recommended to perform accurate reflectance measurements of the sample in order to know the reflection losses incurred. These losses could be curbed down by using anti reflection coating, which would improve the EQE of the solar cells.

# 6 Conclusion

The aim of this thesis is to develop the PESALD process for IO:H deposition and successfully demonstrate it as a TCO on a PV device. A novel metal precursor called DADI is used during this project to achieve this. The PESALD process used here is a two step process comprising of a metal precursor step and a plasma step operating at atmospheric conditions. The plasma is generated in a gas mixture comprising of H<sub>2</sub>, H<sub>2</sub>O and N<sub>2</sub>. A successful implementation of this process would open the opportunity to upscale parts of the PV manufacturing using the ability of Spatial ALD for continuous processing under atmospheric pressure conditions.

It has been shown through experiments that a successful deposition of a TCO layer of IO:H is possible using this process in Chapter 4. However, the reproducibility of the results remains an issue due to the sensitive nature of the process. Furthermore, a successful PV application for the process is shown in Chapter 5, where IOH is successfully deposited as a TCO for CIGS solar cells using PESALD.

In order to optimise the process conditions, systematic variations of process parameters were performed and the resultant layers were characterised. Appropriate conditions for process parameter like plasma voltage and plasma repetition rate have been. Primarily, the growth and electrical analysis of the deposited layers using the ellipsometer, 4 point probe and hall measurement setup is performed to ascertain the majority of the process parameters.

Firstly, the pickup flow for the novel DADI metal precursor is determined. A saturation in GPC has been seen even at low precursor flow of 0.2 slm. However, improved conductivity is observed for a higher precursor pickup flow. Combining, these two effects 0.5 slm is chosen as the appropriate precursor pickup flow. Following the same methodology, the apt. H<sub>2</sub> concentration in the plasma is determined. It has been seen that as the concentration of H<sub>2</sub> increases, the resistivity of the deposited layer is improved. This is attributed to the scavenging nature of H<sub>2</sub> which could be responsible in neutralising the degrading effect of the oxygen impurities in the system. Several times during the course of the experiments, there has been a need to purge the system for many hours due to the vulnerability of the system to oxygen contamination as the PESALD process operates under atmospheric conditions. Based on this analysis, 39% [H<sub>2</sub>] is considered suitable for the process. Next, the rotation frequency of the substrate is determined by using the same procedure. The results from the growth analysis here clearly depicted an unsaturated layer growth as the GPC kept on increasing even at high exposure times. However, for the variable rotation frequency a clear optimum in terms of conductivity has been observed here. Based on this, two rotation frequencies for the substrate, 30 and 50 RPM are considered suitable.

Now, that process conditions for the aforementioned process parameters are fixed. An intensive analysis based on growth, electrical, optical, structural and ageing properties is performed to obtain the appropriate [H<sub>2</sub>O] in the plasma and the apt reactor temperature. One of the primary goals of this thesis has been to investigate the applicability of the process at low temperature. Based on the growth analysis, comparisons can be drawn with the concept of the ALD temperature window. 120-160 °C seems to be the suitable temperature window for this ALD process, however no ideal trend of saturation is observed here. Electrical analysis showed highest conductivity at temperature of 140 °C and 160 °C. A higher mobility is observed for sample deposited at 160 °C (67 cm<sup>2</sup>/Vs) as compared to the sample deposited at 140 °C, hence making it a more optimum condition. Conductivity is independent of [H<sub>2</sub>O] for all investigated reactor temperatures except 160 °C. Mobility is found to be independent of [H<sub>2</sub>O] for 120 and 140 °C. Additionally, highest mobility has been demonstrated at 180 °C but an unexpected high resistivity is also observed. Overall, the most promising conditions on the basis of combined investigation of growth and electrical analysis seem to be a reactor temperature of 140 °C for both high and low [H<sub>2</sub>O] and 160 °C for high [H<sub>2</sub>O]. On the basis of optical analysis, it has been seen that all samples investigated here display an average transmittance of 80%. Moreover, it has been seen that there is a slightly improved optical bandgap and decreased UV absorption for 140 °C as compared to 160 °C at 9.3% [H<sub>2</sub>O]. However optical properties of the layer remain independent of different [H<sub>2</sub>O] at any reactor temperature. By the structural analysis, it has been shown that all the samples investigated showed crystalline behaviour. This is particularly interesting as this was also the case for the

sample deposited at 120 °C. It is known that  $\text{In}_2\text{O}_3$  crystallizes at 140 °C, hence crystalline nature for sample deposited at 120 °C is attributed to the plasma. However, no major influence in the structural property has been observed for the layers deposited at variable reactor temperature and  $[\text{H}_2\text{O}]$ . Finally, the effect of ageing by investigating the degradation in sheet resistance of the samples under atmospheric and Damp heat conditions has been shown. It has been observed here that all IO:H layers undergo significant degradation over time. The main takeaway here which is common for the samples degraded under damp heat and atmospheric conditions is that in both cases, the samples deposited using high  $[\text{H}_2\text{O}]$  undergo less degradation. No significant influence in structural and optical property of the samples has been observed due to degradation. Overall, reduced levels of degradation have been observed for both the samples deposited at 140 °C and 160 °C using 9.3%  $[\text{H}_2\text{O}]$ .

Hence, based on the aforementioned results a decision was made to investigate the possibility to use both the conditions (i.e 140 °C and 160 °C reactor temperature using 9.3%  $[\text{H}_2\text{O}]$ ) in order to deposit IO:H as TCO on CIGS solar cells.

Firstly, experiments were performed to reproduce the results for the electrical and growth properties using the sample holder which was to be used for performing these experiments. The results could be reproduced for the samples deposited at a reactor temperature of 140 °C however they could not be reproduced for the samples deposited at a reactor temperature of 160 °C. Hence, IOH was deposited on CIGS solar cells at a reactor temperature of 140 °C, the performance of these cells were compared with the performance of the reference cells on which sputtered AZO was used as the TCO. Based on the results for the JV characteristics and EQE measurements, it has been seen that better cell characteristics for the samples with sputtered AZO has been observed as compared to the ones with PESALD IOH. This could be attributed to the high thermal budget the CIGS solar cells are subjected to in order to deposit the IOH. Although, it is important to note that similar  $J_{sc}$  is obtained here for samples deposited with IOH as compared to the samples with sputtered AZO. Overall, it is extremely motivating that the process is capable of being used for PV application. However, the process needs to be further optimized to successfully deposit IOH on CIGS.

## Recommendations

As it had been made clear through this thesis, a successful deposition of IO:H as a TCO using the unique and innovative PESALD process is possible. However, the quality of the TCO deposited still needs to be further improved in order to make the layers competitive with the ones produced by using sputtering.

A further investigation needs to be made to improve the mobility of the layers as IO:H is known to be a high mobility ( $140 \text{ cm}^2/\text{Vs}$ ) TCO. This could be done by finding the dominant scattering mechanisms in the layer, which could be found out by comparing the optical mobility to the hall mobility. In addition to this, discrepancies in measurements were observed for certain process conditions. This issue could be resolved by performing more experiments at the same process conditions and checking the reproducibility of the process. This would also help in obtaining a clearer idea of the process sensitivity. Furthermore, improved gas conditions in the SALD reactor would be recommended in order to curb the issue of possible  $\text{O}_2$  and  $\text{H}_2\text{O}$  contamination in the process. In addition to this, it is essential to realize a more uniform gas distribution from the remote plasma source. The issue of radial dependence in the deposited layers due to the current plasma source design will be eliminated by doing so.

It is also important to further analyse the layers using characterisation techniques like EDS and a high quality CEM. As it had been mentioned during the thesis, knowing the exact concentration of H in the layers is essential. With an EDS, this could be known. Furthermore, to have a more concrete idea about the structural properties of the layer, a CEM analysis is necessary. Both these techniques would also help in knowing the exact composition of the layer.

Finally, due to limited time not enough experiments were performed on the solar cell. More investigation in this regard should be encouraged after optimising the layer thickness and performing accurate reflectance measurements on the solar cell. However, priority should be given to the recommendations regarding the development before investigating the TCO on a solar cell.

# Glossary

TCO - Transparent conductive oxide  
PESALD – Plasma enhanced spatial atomic layer deposition  
CIGS - Copper indium gallium selenide  
CdTe – Cadmium Telluride  
BIPV – Building integrated photovoltaics  
AZO – Aluminium doped zinc doped  
IOH - Hydrogen doped indium  
FCA – Free carrier absorption  
ALD – Atomic layer disposition  
PVD – Physical vapour deposition  
CVD - Chemical vapour deposition  
MOCVD – Metalorganic chemical vapour deposition  
ALE – Atomic layer epitaxy  
RF – Radio frequency  
DC- Direct current  
ITO – Tin doped indium oxide  
IZO – Indium doped zinc oxide  
IO:H – Hydrogen doped indium oxide  
IO:Zr – Zirconium doped indium oxide  
AZO- Aluminium doped zinc oxide  
PVD - Physical vapor deposition  
SALD - Spatial atomic layer deposition  
DADI – dimethylamino-kN propyl-kC]dimethyl-Indium  
CEM - Controlled evaporation mixing  
[In acac<sub>3</sub>] - Indium acetylacetonate  
TMIn – Trimethylindium  
InCp – Cyclopentadienylindium  
GPC - Growth per cycle  
DBD - Dielectric barrier discharge  
XRD - X ray diffraction  
NIR - Near infrared region  
COD - Crystallography open database

FWHM - Full width at half maximum

DH – Damp heat

EQE – External quantum efficiencies

## Scientific symbols

$n_e$  – High carrier density

$n_{deg}$  - Induced degeneration

$a_0^*$  - Effective bohr radius

$\vec{E}$  – External field

$(\vec{J})$  – Current density

$\sigma$  - Conductivity

$n_e$  - Charge carrier density

$R_{SH}$  – Sheet resistance

$\mu_e$  – Electron mobility

$\mu_{net}$  - Total electron mobility

$\mu_i$  - Contribution of each scattering mechanism

$\mu_{iip}$  – Ionised impurity scattering

$\lambda_{mfp}$  – Mean free path

$\mu_{gbs}$  - Grain boundary scattering

$\mu_{nis}$  – Mobility due to neutral impurity scattering

$\mu_{ps}$  - Mobility due to phonon scattering

$\omega_p$  – Plasma frequency

$\omega_\tau$  - Damping term

$J_{sc}$  - Short circuit current density

$V_{oc}$  - Open circuit voltage

F.F – Fill Factor

$\tau$  – Exposure time

$\omega$  – Angular velocity

$E_g$  – Optical bandgap

$R_{shunt}$  – Shunt resistance

$R_{series}$  – High series resistance

# Appendix A

## Characterization techniques

In this section the working of the characterisation techniques used during this project is described.

### IOH layer characterisation techniques

#### Four-Point Probe Setup

In order to get a clear picture of the conductivity of the material, it is important to measure the sheet resistance. Keithley 2611A system was used to measure the sheet resistance of the samples. 15 cm x 15 cm samples of IO:H deposited on glass were used for this experiment. A four point probe is a simple apparatus with 4 probes in contact with the surface for which the resistivity needs to be calculated. A current is passed through the outer probes, which in turn induces a voltage on the inner probes. This voltage is then measured by a voltmeter and the sheet resistance is calculated.

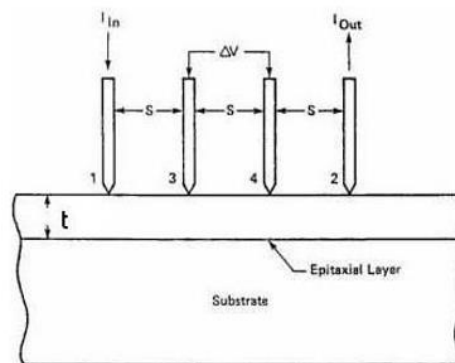


Figure 54 Four-Point Probe Measurement [102]

#### Ellipsometer Setup

The thickness of a sample is determined by using an optical technique called spectroscopic ellipsometry. A Horiba ellipsometer as depicted in Figure 55 was used in this project to perform the SE measurements. In order to find the thickness using an ellipsometer, a linearly polarized beam of light is incident on the sample nearby the Brewster angle where reflected light is characterized by a large change of the polarization state. Polarization can be understood as a property applicable to light waves which specifies the geometrical orientation of oscillations. Polarized light with its electric field along the plane of incidence is referred as p-polarized and polarized light with its electric field perpendicular to the plane of incidence is called s-polarized. The Brewster angle is defined as the angle of incidence which results in the reflected and refracted ray becoming perpendicular to each other.



Figure 55 Ellipsometer setup

The working of the ellipsometer is depicted in Figure 56 below. An ellipsometer measures the polarization state, expressed by the ratio of the parallel (p-polarized) and perpendicular (s-polarized) components relative to the plane of incidence. This is done in the following order by the ellipsometer:

- A linearly polarized light is first incident on the sample. The amplitudes of both incident p and s polarization light is the same and the phase difference between them is equal to 0, hence  $E_{ip} = E_{is}$ .
- In the reflected ray, it can be observed that s and p polarizations show different changes in amplitude and phase. The change in s and p polarized light is what is measured using the ratio  $r_p/r_s$  which is further expressed via  $\Psi$  and  $\Delta$ . Where,  $\Psi$  represents the amplitude ratio and  $\Delta$  represents the phase difference between s and p polarized light wave.
- The refractive index (n) and the extinction coefficient (k) can be directly determined from  $\Psi$  and  $\Delta$  with the help of Fresnel equations.[103]
- Since a layer on a substrate would result in multiple reflections, a model is used to represent the total reflectance of the substrate and the layer. As a result of which, the measured  $\Psi$  and  $\Delta$  values are fitted with the simulated  $\Psi$  and  $\Delta$  values from the model where the layer thickness, and n and k of the layer are fitting parameters.

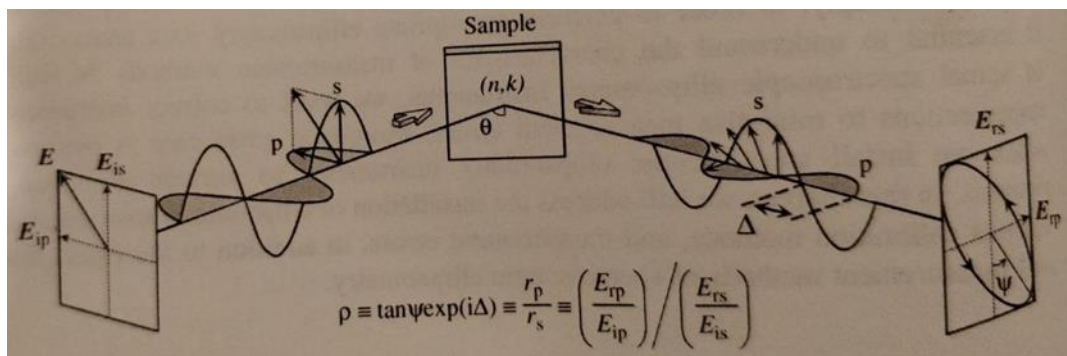


Figure 56 Working Principle of Spectroscopic Ellipsometry[103]

For thin coated films, reflections from the top and bottom surfaces of the film are coherent. This means that there is a constant phase difference between the top and bottom surfaces of the film. In this project, a glass substrate was used for performing the deposition. Due to the transparent nature of the substrate, additional reflections occur from the back surface while performing ellipsometry. It is important to note that the light ray reflected from the back surface must travel through the substrate twice. This results in incoherence with the front surface reflection and complicates the measured spectra in the ellipsometer. Hence, it is essential to suppress these back reflections. This is done by sticking a Scotch type tape on the back side of the glass substrate. The refractive index of the tape matches well with glass, making this technique effective in curbing back reflections[104].

## Hall Measurement Setup

A setup commonly used in determining the electrical properties of a material is the Hall measurement setup. Ecopia HMS 5000 system was used in this project to perform the hall measurements. Mobility of charge carriers, carrier density and resistivity values are obtained from this setup. As the name suggests, these measurements are based on the phenomenon of Hall effect.

Hall effect is the production of potential difference across an electric current in a conductor when a magnetic field is applied perpendicular to it. This potential difference is referred to as the Hall Voltage. Its existence can be explained by the concept of Lorentz force as shown in Figure 57. Lorentz force is a force exerted on an electrical charge when it moves in the presence of a magnetic field.

When such a situation occurs in a conductor, all the charge carriers of a similar polarity are moved to one side creating a potential difference between the two sides of the conductor. As previously mentioned this voltage is referred to as the Hall voltage. The charge carrier density ( $n_s$ ) and the electron mobility ( $\mu$ ) are further calculated by using the following formula in this setup.

$$\mu = \frac{V_H}{R_S I B} \quad (\text{A.1})$$

$$n_s = \frac{I B}{e |V_H|} \quad (\text{A.2})$$

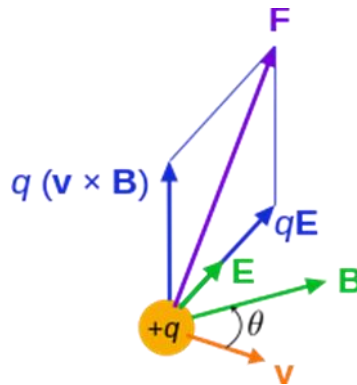


Figure 57 Lorentz force

For this experiment, the samples were cut into 3 cm x 3 cm by using laser cutting. This particular dimension of the sample was chosen due to the size of the sample holder in the apparatus. The sample was stuck on to the cartridge, using conductive Ag contact. This cartridge can be plugged easily into the system and the electrical properties of the sample can be obtained by inputting the thickness of the sample. The thickness of the sample was obtained by using the ellipsometer.



Figure 58 Hall measurement setup [105]

## Spectrophotometer

The reflectance and transmittance through a sample is measured by using a spectrophotometer. In this project, Cary UV/Vis/NIR 5000 from Agilent was used for this purpose. The spectral range of 300-1200nm was used because this wavelength range includes the visible and near infrared part of the spectrum. Transmittance of a substance is understood as the amount of light that passes through the substance when it is subjected to certain intensity of light. Reflectance on the other hand is used to measure the amount of light that is reflected from the surface. Transmittance and reflectance can be calculated by using the following formulas.

$$\text{Transmittance} = \frac{I_T}{I_0} \quad (\text{A.3})$$

$$\text{Reflectance} = -\log \frac{I_T}{I_0} \quad (\text{A.4})$$

Where  $I_T$ ,  $I_R$  and  $I_0$  refer to the intensity of the light transmitted, reflected and incident on the sample respectively. Eq.1.9 is referred to as the Beer Lambert law. Absorbance of the sample which refers to the amount of light absorbed by the sample can also be calculated by using the spectrophotometer. This is done by using the following formula.

$$1 = A + T + R \quad (\text{A.5})$$

Where A, T and R refer to the absorbance, reflectance and transmittance respectively. For this experiment, the same samples as mentioned in the hall measurement setup have been used. As it can be observed in Figure 59 the position of mirror M2 is adjusted depending on whether the experiment is performed for transmittance or reflectance. For transmittance, the mirror M2 is placed further behind as compared to its position when used for reflectance.

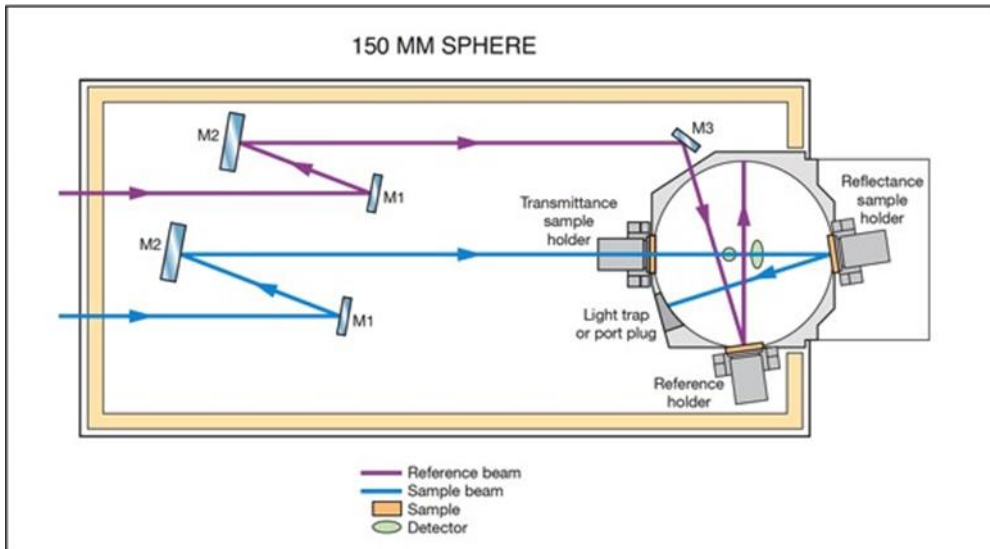


Figure 59 Integrating sphere[106]

The trajectory of the ray of light for transmittance and reflectance respectively is depicted in Figure 60. In order to calibrate the reference, first the experiment is performed by keeping no sample. This is done so that the reference is set to the maximum transmittance. This is followed by keeping the test sample at the entry point of the incident rays in the integrating sphere for measuring transmittance. Meanwhile, for the case of reflectance the sample is placed at a radially opposite position wrt its position in the case of transmittance.

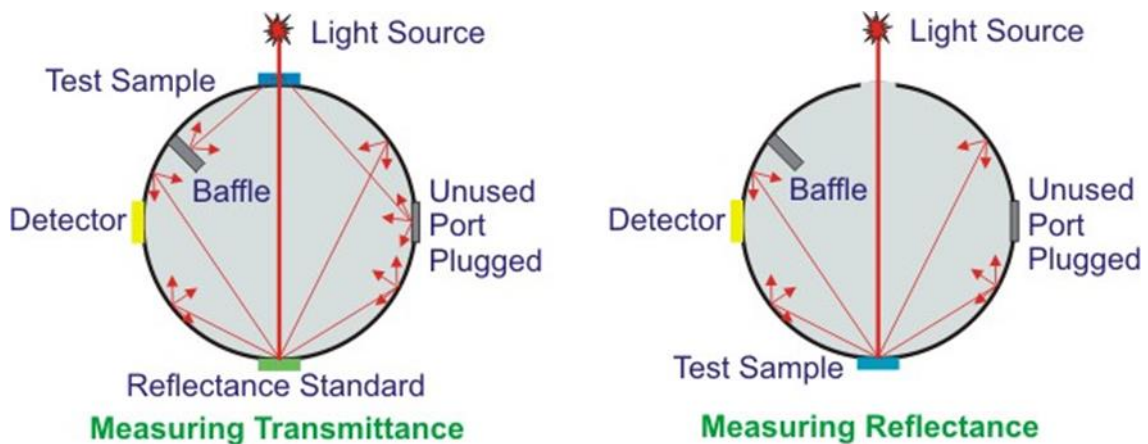


Figure 60 Measuring transmittance and reflectance[107]

## X-ray diffraction

The concept of diffraction is commonly observed when an electromagnetic radiation strikes on a symmetrical structure with some geometrical variations equivalent to the wavelength of the incident radiation. During, X-ray diffraction, the beam of monochromatic X-rays of wavelength 0.154 nm (standard Cu K $\alpha$  radiation) is incident on the crystalline material. These rays get reflected and undergo either constructive or destructive interference. The intensity and direction of these rays are then detected. The position of the X-ray scattered peaks are determined by using the Bragg's law. It is given by the following equation.

$$n\lambda = 2d \sin \theta \quad (\text{A.7})$$

Here  $\lambda$  refers to the wavelength of the incident beam,  $\theta$  is the angle of incidence in degrees,  $d$  is the interatomic distance in meters, and  $n$  is an integer.  $2d \sin \theta$  is the difference between the path of the two waves undergoing interference. A constructive interference occurs when the two waves are in phase or analytically the difference between their paths lengths is equivalent to the integer multiple of the wavelength. Hence, when  $n=1,2,3$ .

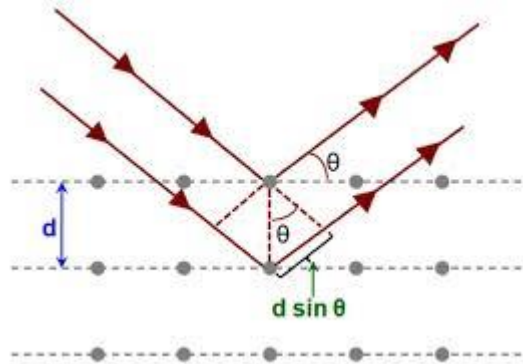


Figure 61 Bragg's law [108]

This characterisation technique provides crucial detail into the crystal structure of the material. Every crystalline material is known to possess its distinct characteristic peaks in XRD. These peaks are indicative of the possible orientations of the crystal in the material. Based on this information, the material can be identified and details about the crystallinity of the material could be made.

## CIGS solar cell characterisation techniques

### Illuminated J-V curve

One of the most common methods to characterise the solar cell is to test the device under standard illumination of  $100 \text{ W/m}^2$  at a temperature of  $25 \text{ }^\circ\text{C}$ . Basic parameters to measure the performance of the cell can be measured using this technique. Open circuit voltage ( $V_{OC}$ ), short circuit current density ( $J_{SC}$ ) and Fill Factor (FF) are obtained using this technique. These parameters can then be used to obtain the efficiency of the cell. The following formula is used to obtain the  $V_{OC}$  of the cell.

$$V_{OC} = \frac{k_B T}{q} \ln \left( \frac{J_{ph}}{J_0} + 1 \right) \quad (\text{A.8})$$

Here,  $J_{ph}$  refers to the photo-generated current density,  $J_0$  refers to the saturation current density,  $k$  is the Boltzmann constant equal to  $1.38 \times 10^{-23} \text{ m}^2\text{kg s}^{-2}\text{K}^{-1}$ ,  $T$  is the temperature in Kelvin and  $q$  is the charge of an electron equal to  $1.6 \times 10^{-19} \text{ C}$ . The efficiency of the solar cells can then be calculated by using the following formula.

$$\eta = \frac{V_{OC} J_{SC} FF}{I_{in}} \quad (\text{A.9})$$

Here  $I_{in}$  refers to the standard incident intensity of  $1000 \text{ W/m}^2$ .

### External quantum efficiency (EQE)

The external quantum efficiency (EQE) of a solar cell is the ratio of the number of charge carriers collected by the solar cell to the number of photons of a given energy incident on the solar cell. It is given by the following formula.

$$EQE(\lambda) = \frac{I_{ph}(\lambda)}{q \phi_{ph}(\lambda)} \quad (\text{A.10})$$

Here  $I_{ph}$  is the photocurrent,  $q$  the elementary charge and  $\varphi_{ph}(\lambda)$  is the photon flux. In an ideal scenario, the EQE of a solar cell at all wavelengths smaller than that of its bandgap should be equivalent to 1. However, this is not the case due to recombination or reflection effects.

The short-circuit current can then be obtained by integrating over the entire spectrum as shown in the following equation.

$$J_{SC} = \int_{\lambda_1}^{\lambda_2} EQE(\lambda) \varphi(\lambda) d\lambda \tag{A.11}$$

# Appendix B

## Additional information

### B.1 Expected growth and nucleation during the ALD process and subsequent solid phase crystallization by B. Macco.

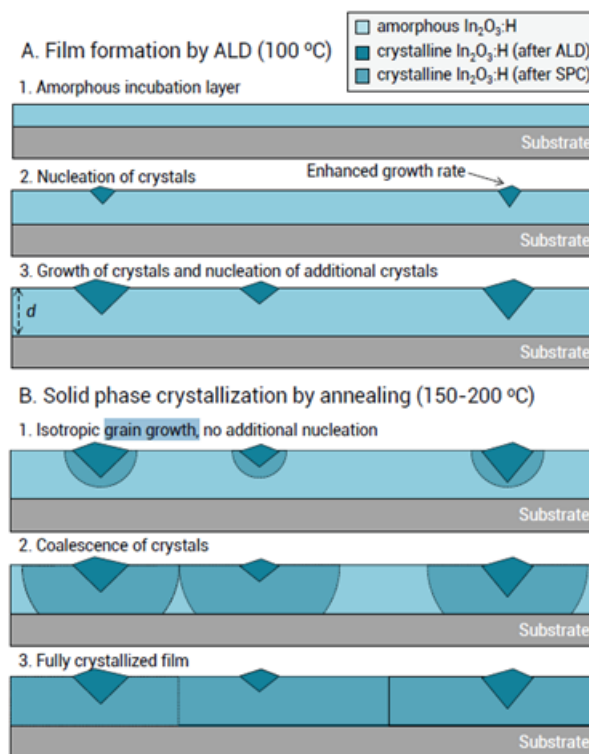


Figure 62 Proposed model by Macco et al to depict the growth and nucleation process in the ALD process [23]

### B.2 Paschen's law

An electric arc is developed between two parallel metal plates in a gas by applying the breakdown voltage. The breakdown voltage is found to be dependent on the pressure and the length between the electrodes. On varying the length and pressure between the electrodes for different inert gases like He, Ne, Ar,  $N_2$  and  $H_2$ , different values for the breakdown voltages are obtained. Plotting the values of breakdown voltages as a

function of the product of pressure and length between the electrodes, results in formation of specific curves for different inert gases. These curves are depicted in Figure 63 and are referred as the Paschen curves. The equation obtained from these curves can be used to obtain the breakdown voltage as a function of gap length and pressure, and is referred as Paschen's law.

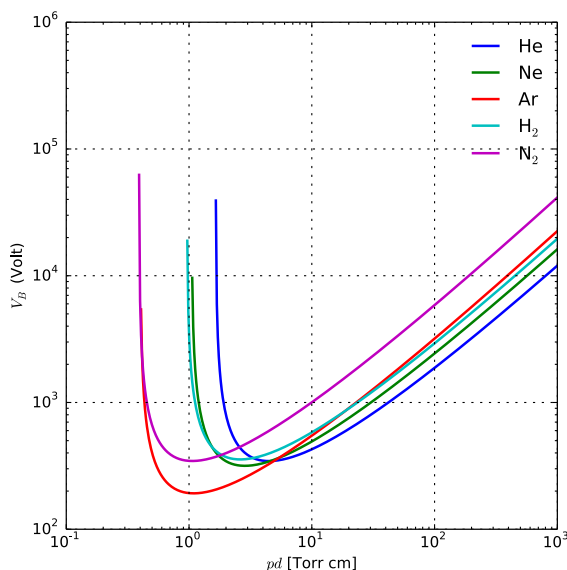


Figure 63 Paschen curves [109]

### B.3 Process conditions used for determining the process sensitivity

Process parameters used for Sample A and Sample B are the following.

<b>DADI precursor pickup flow (slm)</b>	<b>0.5</b>
<b>Plasma down flow (slm)</b>	5
<b>Plasma top flow (slm)</b>	1
<b>H<sub>2</sub> [%]</b>	39
<b>H<sub>2</sub>O [%]</b>	3.4
<b>RPM</b>	20
<b>No. of cycles</b>	800
<b>Reactor temperature (°C)</b>	150
<b>Plasma Voltage (kV)</b>	5.2
<b>Plasma repetition rate (kHz)</b>	66.7

Thickness and corresponding sheet resistance measured for Sample A and Sample B for three distinct radii, 30, 40 & 50mm.

	<b>Thickness at R-30mm (nm)</b>	<b>Sheet Resistance at R-30mm (Ω/sq)</b>	<b>Thickness at R-40mm (nm)</b>	<b>Sheet Resistance at R-40mm (Ω/sq)</b>	<b>Thickness at R-50mm (nm)</b>	<b>Sheet Resistance at R-50mm (Ω/sq)</b>
<b>Sample A</b>	41.5	948.9	36.7	849.4	34.8	1300
<b>Sample B</b>	40.8	746.5	34.1	777.9	32.6	843.2

Process parameters used for Sample C and Sample D are the following.

<b>DADI precursor pickup flow (slm)</b>	<b>0.5</b>
<b>Plasma down flow (slm)</b>	5
<b>Plasma top flow (slm)</b>	1
<b>H<sub>2</sub> [%]</b>	39
<b>H<sub>2</sub>O [%]</b>	3.4
<b>RPM</b>	40
<b>No. of cycles</b>	800
<b>Reactor temperature (°C)</b>	150
<b>Plasma Voltage (kV)</b>	5.2
<b>Plasma repetition rate (kHz)</b>	66.7

Thickness and corresponding sheet resistance measured for Sample C and Sample D for three distinct radii, 30, 40 & 50mm.

	<b>Thickness at R-30mm (nm)</b>	<b>Sheet Resistance at R-30mm (Ω/sq)</b>	<b>Thickness at R-40mm (nm)</b>	<b>Sheet Resistance at R-40mm (Ω/sq)</b>	<b>Thickness at R-50mm (nm)</b>	<b>Sheet Resistance at R-50mm (Ω/sq)</b>
<b>Sample C</b>	25.2	2533	22.2	2666	25.3	3100
<b>Sample D</b>	27.2	1620	19.7	1820	18.4	2140

## B.4 Refractive index of amorphous and crystallized IO:H

The refractive index  $n$  and the extension coefficient  $k$  (imaginary part of  $n$ ) of amorphous and crystallized IO:H is provided by Macco et al below. The optical constants were obtained by fitting ellipsometry data using a combination of a Drude and Tauc-Lorentz oscillator[25] .

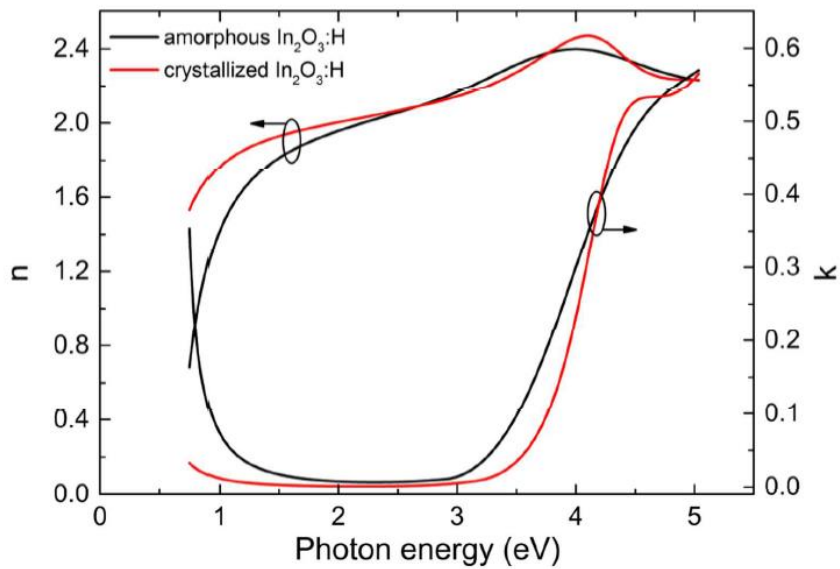


Figure 64 Refractive index  $n$  and extinction coefficient  $k$  of amorphous and crystallized IO:H [25]

### B.5 Transmittance & reflectance measurements for IO:H samples at 6.7% [H<sub>2</sub>O] for variable reactor temperatures

Figure 65 represents the transmittance and reflectance results for IO:H samples at different temperatures at 6.7 % [H<sub>2</sub>O]. These results are quite similar to the one depicted in Figure 38 and depict that change in [H<sub>2</sub>O] had negligible effects on transmittance and reflectance of the samples.

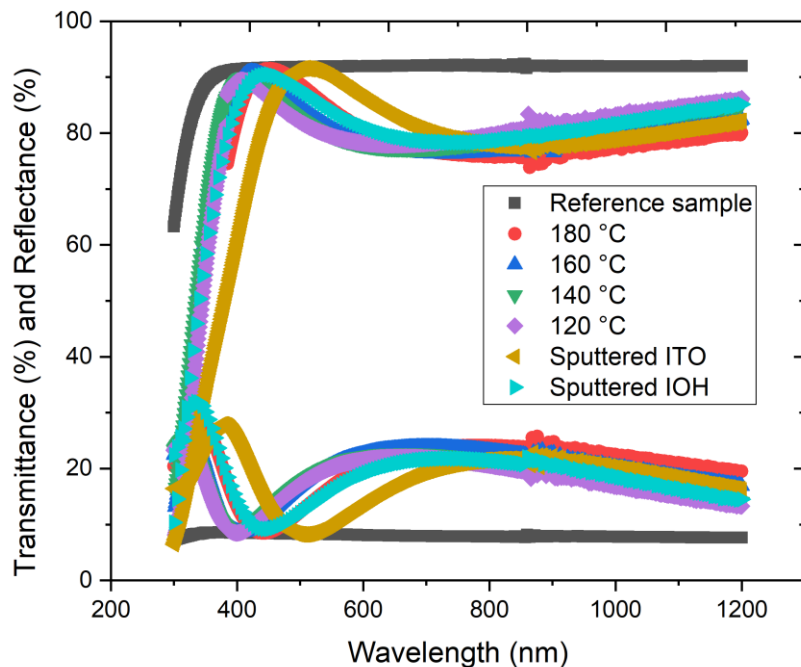


Figure 65 Transmittance & Reflectance of IO:H samples at different temperatures for 6.7 % [H<sub>2</sub>O] same process condition as Figure 31

## B.6 Raman spectroscopy

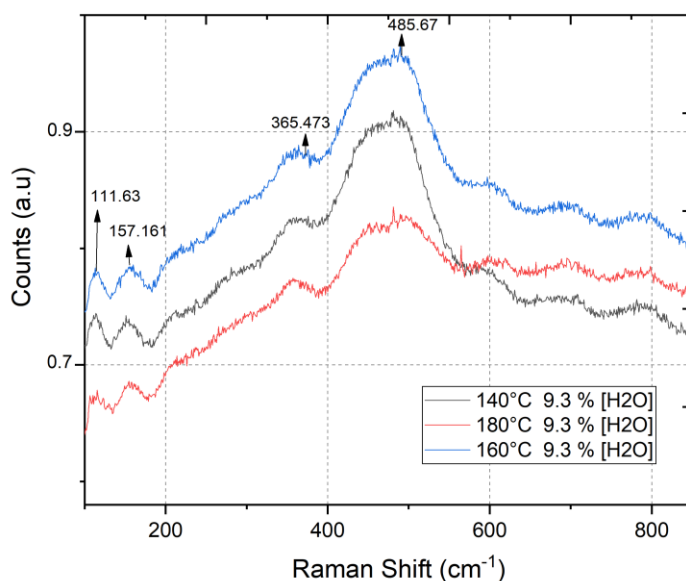


Figure 66 Raman spectroscopy results for samples deposited at different reactor temperatures at 9.3% [H<sub>2</sub>O]

As it can be observed in Figure 66, no distinct and clear peaks are observed for the IO:H samples deposited using PESALD. This could be due to the thickness of the deposited samples. This measurement hence, was not considered reliable and no hypothesis/conclusions are drawn from this. It would be advised to perform Raman spectroscopy on a thicker layer of IO:H in the future.

## B.7 Texture coefficient calculations for IO:H samples at 6.7% [H<sub>2</sub>O] for variable reactor temperatures

Reactor temperature	Texture coefficient(211)	Texture coefficient (222)	Texture Coefficient (400)	Texture Coefficient (440)	Texture Coefficient (622)
180	0.28	0.343097923	0.19943975	0.091244687	0.083227214
160	0.25	0.320915445	0.264053997	0.079526921	0.08366088
140	0.28	0.359931999	0.193299232	0.084894273	0.081025268
120	0.32	0.350394415	0.146959289	0.088547136	0.084402377

Table 17 Texture coefficient calculations at 6.7% [H<sub>2</sub>O]

# Bibliography

- [1] K. J. Arno Smets, Olindo Isabella, Rene Van Swaaij, Miro Zeeman, *Solar Energy*. 2015.
- [2] G. Gordon-Harper. "Solar Energy Installations in 2017 topped Gas, Coal and Nuclear Combined, Amid Steady Growth in Renewables." [sdg.iisd.org/news/solar-energy-installations-in-2017-topped-gas-coal-and-nuclear-combined-amid-steady-growth-in-renewables/](http://sdg.iisd.org/news/solar-energy-installations-in-2017-topped-gas-coal-and-nuclear-combined-amid-steady-growth-in-renewables/) (accessed 18/1/2019).
- [3] IEA. "Renewables 2017." <https://www.iea.org/publications/renewables2017/> (accessed 18/1/2019).
- [4] T. D. Lee, A.U. Ebong, "Thin Film Solar Technology: A review," *IEEE*, 2015.
- [5] T. D. Lee, A. U. Ebong, "A review of thin film solar cell technologies and challenges," *Renewable and Sustainable Energy Reviews*, vol. 70, pp. 1286-1297, 2017, doi: 10.1016/j.rser.2016.12.028.
- [6] H. B. R. Naciri , A. Mzerd, A. Rahioui , M. Abd-Lefdil, C. Messaoudi, "The role of the CdS buffer layer in the CuInS<sub>2</sub> Thin film solar cel," *Revue des Energies Renouvelables CER'07 Oujda*, 2007.
- [7] F. A. Kushiya K., Sugiyama I., Miura T., Okumura D., Sato M., Ooshita M., Yamase O, "Large area ZnO films optimized for graded band-gap Cu(InGa)Se<sub>2</sub>-based thin-film mini-modules," *Solar Energy Materials and Solar Cells*, pp. 291–297, 1997, doi: 10.1016/S0927-0248(97)00055-X.
- [8] R. M. Pasquarelli, D. S. Ginley, R. O'Hayre, "Solution processing of transparent conductors: from flask to film," *Chem Soc Rev*, vol. 40, no. 11, pp. 5406-41, Nov 2011, doi: 10.1039/c1cs15065k.
- [9] S. M. K.L. Chopra, D. K. Pandya, "Transparent Conductors- A Status Review," 1982.
- [10] D. G. Elvira Fortunato, Hideo Hosono and David C. Paine, "Transparent Conducting Oxides for Photovoltaics," *MRS Bull.* , vol. 32, 242-7, 2007.
- [11] C. L. Su Sheng, Sheng Xu, "P-type transparent conducting oxides," *Physica Status Solidi (A) Applications and Materials*, 2006, doi: 10.1002/pssa.200521479.
- [12] M. I. H. Wayesh Qarony, M. Khalid Hossain, M. Jalaluddin, A.Haque, A.R.Saad, Yuen HongTsang, "Efficient amorphous silicon solar cells: characterization, optimization, and optical loss analysis," *Results in Physics*, vol. Volume 7, 2017. [Online]. Available: <https://doi.org/10.1016/j.rinp.2017.09.030>.
- [13] M. T. Horantner, Giles E. Eperon, Henry J. Snaith, "Metal halide perovskite tandem and multiple-junction photovoltaics," *Nature reviews chemistry*, vol 1, 2017.
- [14] N. F. Mott, L. Friedman, "Metal-insulator transitions in VO<sub>2</sub>, Ti<sub>2</sub> O<sub>3</sub> and Ti<sub>2-x</sub> V<sub>x</sub> O<sub>3</sub>," *Philosophical Magazine*, vol. 30 (2), pp. 389–402, 1974, doi: 10.1080/14786439808206565.
- [15] I. Hamberg, C. G. Granqvist, "Evaporated Sn-doped In<sub>2</sub> O<sub>3</sub> films: Basic optical properties and applications to energy-efficient windows," *Journal of Applied Physics*, vol. 60 (11), pp. R123–R160, 1986, doi: 10.1063/1.337534.
- [16] Y. Zhang, Z. Jin, M. H. White, "A quantum mechanical mobility model for scaled NMOS transistors with ultra-thin high-K dielectrics and metal gate electrodes.," *Solid-State Electronics*, vol. 52, (11), pp. 1810–1814, 2008, doi: 10.1016/j.sse.2008.08.003.
- [17] Q. Ma, D. B. Buchholz, D. Alducin, "The Structure and Properties of Amorphous Indium Oxide," *Chemistry of Materials*, vol. 26, pp. 5401–5411, 2014, doi: 10.1021/cm502689x.
- [18] A. Luque, S. Hegedus, *Handbook of Photovoltaic Science and Engineering*. John Wiley & Sons, Ltd., second edn, 2011.
- [19] J. Dekker, "Transparent Conductive Oxides on Polymeric Substrates by Pulsed Laser Deposition," Ph.D., Eindhoven University of Technology, 2007.
- [20] H. Hosono, D. C. Paine, D. S. Ginley, *Handbook of transparent conductors* (Springer, New York). 2010.
- [21] R. L. Petritz, "Theory of Photoconductivity in Semiconductor Films," *Physical Review*, vol. 104, no. (6), pp. 1508–1516, 1956, doi: 10.1103/PhysRev.104.1508.
- [22] J. Y. W. Seto, "The electrical properties of polycrystalline silicon films," *Journal of Applied Physics*, vol. 46, 12, pp. 5247–5254, 1975, doi: 10.1063/1.321593.
- [23] B. Macco, "Atomic layer deposition of metal oxide thin films for Si heterojunction solar cells," PhD, T.U. Eindhoven, 2016.

- [24] C. Erginsoy, "Neutral Impurity Scattering in Semiconductors.," *Physical Review*, vol. 79, no. (6), pp. 1013–1014, 1950, doi: 10.1103/PhysRev.79.1013.
- [25] B. Macco, Y. Wu, D. Vanhemel, W. M. M. Kessels, "High mobility In<sub>2</sub>O<sub>3</sub>:H transparent conductive oxides prepared by atomic layer deposition and solid phase crystallization," *physica status solidi (RRL) - Rapid Research Letters*, vol. 8, no. 12, pp. 987-990, 2014, doi: 10.1002/pssr.201409426.
- [26] X.-D. Zhou, G.J. Exarhos "Thin Solid Films," vol. 515, no. 7025, 2007.
- [27] A. P. F. Ruske, V. Sittinger, B. Szyszka, D. Greiner, B. Rech, "Optical modeling of free electron behavior in highly doped ZnO films," *Thin Solid Films*, vol. 518, pp. 1289–1293, 2009.
- [28] A. Klein *et al.*, "Transparent Conducting Oxides for Photovoltaics: Manipulation of Fermi Level, Work Function and Energy Band Alignment," *Materials (Basel)*, vol. 3, no. 11, pp. 4892-4914, Nov 2 2010, doi: 10.3390/ma3114892.
- [29] G. Rupprecht, *Z. Phys.*, vol. 139, 1954.
- [30] F. F. a. B. F, *Phys. Rev. B*, vol. 77, 2008.
- [31] M. Marezio, "Refinement of the crystal structure of In<sub>2</sub>O<sub>3</sub> at two wavelengths" *Acta Crystallogr.*, vol. 20, 1966.
- [32] O. Bierwagen, "Indium oxide—a transparent, wide-band gap semiconductor for (opto)electronic applications," *Semiconductor Science and Technology*, vol. 30, no. 2, 2015, doi: 10.1088/0268-1242/30/2/024001.
- [33] R. P. Karazhanov, S Zh. Karazhanov, P. Vajeeston, A. Ulyashin, and T. G. Finstand, H. Fjellvag, "Phase stability, electronic structure, and optical properties of indium oxide polytypes" *Phys. Rev.*, vol. 76, 2007.
- [34] R. L. Weiher, R. P. Ley, "Optical Properties of Indium Oxide," *Journal of Applied Physics*, vol. 37, no. 1, pp. 299-302, 1966, doi: 10.1063/1.1707830.
- [35] C. J. V. Scherer, A. Krapf *et al.*, "Transport and angular resolved photoemission measurements of the electronic properties of In<sub>2</sub>O<sub>3</sub> bulk single crystals.," *100*, vol. 21, 2012], doi: 10.1063/1.4719665.
- [36] J. E. Crowell, "Chemical methods of thin film deposition: Chemical vapor deposition, atomic layer deposition and related technologies," *Journal of Vacuum Science & Technology*, vol. 21, 2003, doi: 10.1116/1.1600451.
- [37] A. K. K. Ellmer, and B. Rech, "Transparent Conductive Zin Oxide Basic and Applications in Thin Film Solar Cells," 2008.
- [38] J. Ramanujam. U. P. Singh, "Copper indium gallium selenide based solar cells – a review," *Energy Environ. Sci*, vol. 10, no. 1306, 2017, doi: 10.1039/c7ee00826k.
- [39] J. Gaines. "Challenges for Non-Ideal Atomic Layer Deposition Processes & Systems." <https://www.lesker.com/newweb/blog/post.cfm/challenges-for-non-ideal-atomic-layer-deposition-processes-systems> (accessed 5/3/2019).
- [40] P. Poodt *et al.*, "Spatial atomic layer deposition: A route towards further industrialization of atomic layer deposition," *Journal of Vacuum Science & Technology A: Vacuum, Surfaces, and Films*, vol. 30, no. 1, 2012, doi: 10.1116/1.3670745.
- [41] G. Legeay, X. Castel, "A gradual annealing of amorphous sputtered indium tin oxide: Crystalline structure and electrical characteristics," *Thin Solid Films*, vol. 520, no. 11, pp. 4021-4025, 2012, doi: 10.1016/j.tsf.2012.01.029.
- [42] H. Fujiwara, T. Koida, "High-mobility hydrogen doped In<sub>2</sub>O<sub>3</sub> transparent conductive oxide for a-Si:H/c-Si heterojunction solar cells," *Elsevier*, 2008.
- [43] X. Chen., C. Liu., J. Du., J. Ni., G. Hou., Y. Zhao. , X. Zhang. , "Highly transparent and conductive indium tin oxide thin films for solar cells grown by reactive thermal evaporation at low temperature," *Applied Physics A.*, vol. 117, 2014, doi:10.1007/s00339-014-8436-x.
- [44] A. R. M. W. O. Edynoor, "Transparent coating oxide- Indium Zinc Oxide as conductive coating: A review," 2017.
- [45] W. Witte, R. Carron, D. Hariskos, F. Fu, R. Menner, S. Buecheler, "IZO or IOH Window Layers Combined with Zn(O,S) and CdS Buffers for Cu(In,Ga)Se<sub>2</sub> Solar Cells," *physica status solidi (a)*, vol. 214, no. 12, 2017, doi: 10.1002/pssa.201700688.

- [46] M. Morales-Masis, "Highly Conductive and Broadband Transparent Zr-Doped In<sub>2</sub>O<sub>3</sub> as Front Electrode for Solar Cells," *IEEE JOURNAL OF PHOTOVOLTAICS*, vol. Vol 8, 2018.
- [47] J. Burst. T. A. Gessert, X. Li, M. Scott, T. J. Coutts, "Advantages of transparent conducting oxide thin films with controlled permittivity for thin film photovoltaic solar cells," *Thin Solid Films*, vol. 519, pp. 7146–7148, 2011.
- [48] A. N. Tiwari, T. S. Calnan, "High mobility transparent conducting oxides for thin film solar cells," *Thin solid Films*, 2009.
- [49] T. Koida, H. Fujiwara, M. Kondo, "High-mobility hydrogen-doped In<sub>2</sub>O<sub>3</sub>In<sub>2</sub>O<sub>3</sub> transparent conductive oxide for a-Si:H/c-Si heterojunction solar cells," *Solar Energy Materials and Solar Cells*, vol. 93, no. 6-7, pp. 851-854, 2009, doi:10.1016/j.solmat.2008.09.047.
- [50] Y. Wu, B. Macco, "High mobility In<sub>2</sub>O<sub>3</sub>:H transparent conductive oxides prepared by atomic layer deposition and solid phase crystallization," *Phys. Status Solidi RRL* **8**, No. 12, 987-990, 2014.
- [51] K. Okada *et al.*, "Correlation between resistivity and oxygen vacancy of hydrogen-doped indium tin oxide thin films," *Thin Solid Films*, vol. 519, no. 11, pp. 3557-3561, 2011, doi: 10.1016/j.tsf.2011.01.249.
- [52] M. S. Sebastian Husein, Bradley West, Laura Ding, Fabien Dauxou, Monica Morales-Masis, "Carrier scattering mechanisms limiting mobility in hydrogen doped indium oxide," *Journal of Applied Physics*, vol. 123, no. 245102, 2018, doi: 10.1063/1.5033561.
- [53] J. Keller *et al.*, "Direct comparison of atomic layer deposition and sputtering of In<sub>2</sub>O<sub>3</sub>:H used as transparent conductive oxide layer in CuIn<sub>1-x</sub>Ga<sub>x</sub>Se<sub>2</sub> thin film solar cells," *Solar Energy Materials and Solar Cells*, vol. 157, pp. 757-764, 2016, doi: 10.1016/j.solmat.2016.07.012.
- [54] T. Tohsophon, A. Dabirian, S. De Wolf, M. Morales-Masis, and C. Ballif, "Environmental stability of high-mobility indium-oxide based transparent electrodes," *APL Materials*, vol. 3, no. 11, 2015, doi: 10.1063/1.4935125.
- [55] J.-H. Y. Chi-Ying Hsiao, Jyh-Rong Gong, Dong-Yuan Lyu, "Transparent conductive IZO films prepared by atomic layer deposition using DEZn/TMIn and N<sub>2</sub>O," *3rd International Nanoelectronics Conference (INEC)*, 2010, doi: 10.1109/INEC.2010.5424867.
- [56] M. R. Timo Asikainen, Markku Leskelä, "Atomic layer deposition growth of zirconium doped In<sub>2</sub>O<sub>3</sub> films," *Thin Solid Films*, vol. 440, no. 1, 2003.
- [57] R. A. P. Ribeiro, E. Longo, J. Andres, and S. R. de Lazaro, "A DFT investigation of the role of oxygen vacancies on the structural, electronic and magnetic properties of ATiO<sub>3</sub> (A = Mn, Fe, Ni) multiferroic materials," *Phys Chem Chem Phys*, vol. 20, no. 45, pp. 28382-28392, Nov 21 2018, doi: 10.1039/c8cp04443k.
- [58] M. C. T. Matthew D. McCluskey, Samuel T. Teklemichael, "Hydrogen in oxide semiconductors," *Materials Research Society*, vol. 27, no. 17, 2012, doi: 10.1557/jmr.2012.137.
- [59] X. Z. P. Reunchan, S. Limpijumngong, A. Janotti, C.G. Van and d. Walle, "Vacancy defects in indium oxide: An ab-initio study.," *Curr. Appl Phys*, vol. 11, 2011.
- [60] M. Grundmann, "The Physics of Semiconductors," *Springer Berlin*, 2006.
- [61] M. M. Jephias Gwamuri, Jeyanthinath Mayandi, Patrick K. Bowen, Joshua M. Pearce, "Influence of Oxygen Concentration on the Performance of Ultra-Thin RF Magnetron Sputter Deposited Indium Tin Oxide Films as a Top Electrode for Photovoltaic Devices," *Materials*, vol. 9, no. 1, p. 63, 2016.
- [62] R. B. O. Nilsen, E.V. Monakhov, N. Muthukumarasamy, H. Fjellvag, B.G. Svensson, "Thin films of In<sub>2</sub>O<sub>3</sub> by atomic layer deposition using In(acac)<sub>3</sub>," *Thin Solid Films*, vol. 517, p. 6320, 2009.
- [63] A. B. F. Martinson, J.W. Elam, M.J. Pellin, A.J.T. Hupp, "Atomic layer deposition of In<sub>2</sub>O<sub>3</sub> using cyclopentadienyl indium: a new synthetic route to transparent conducting oxide films.," *Chem. Mater*, vol. 18, p. 3571, 2006.
- [64] M. R. T. Asikainen, M. Leskelä, T. Prohaska, G. Friedbacher, M. Grasserbauer., "AFM and STM studies on In<sub>2</sub>O<sub>3</sub> and ITO thin films deposited by atomic layer epitaxy," *Appl. Surf. Sci.*, vol. 99, pp. 91-98, 1996.
- [65] J. A. Libera, J. N. Hryn, and J. W. Elam, "Indium Oxide Atomic Layer Deposition Facilitated by the Synergy between Oxygen and Water," *Chemistry of Materials*, vol. 23, no. 8, pp. 2150-2158, 2011, doi: 10.1021/cm103637t.

- [66] W. J. Maeng, D.-w. Choi, J. Park, J.-S. Park, "Atomic layer deposition of highly conductive indium oxide using a liquid precursor and water oxidant," *Ceramics International*, vol. 41, no. 9, pp. 10782-10787, 2015, doi: 10.1016/j.ceramint.2015.05.015.
- [67] F. F. Chen, "Introduction to Plasma Physics and Controlled Fusion," *New York: Springer International*, 2015.
- [68] H. B. Profijt, S. E. Potts, M. C. M. Knoops, Wilhelmus M. M. Kessels, "Plasma-assisted atomic layer deposition: basics, opportunities and challenges," *Journal of Vacuum Science and Technology*, vol. 29, no. 5, 2011, doi: 10.1116/1.3609974.
- [69] C. S.-B. F. Massines, F. Fanelli, N. Naudé, N. Gherardi, "Atmospheric Pressure Low Temperature Direct Plasma Technology: Status and Challenges for Thin Film Deposition," *Plasma Processes and Polymers*, vol. 9, no. 11-12, pp. 1041-1073, 2012.
- [70] L. Bárdos, H. Baránková, "Plasma processes at atmospheric and low pressures," *Vacuum*, vol. 83, no. 3, pp. 522-527, 2008, doi: 10.1016/j.vacuum.2008.04.063.
- [71] F. Arefi-Khonsari, "Depot et traitement des polymeres par procedes plasma " *Formation Continue INPG – 17eme session – Traitements de Surface par Plasmas, 24 – 28 Mars 2003, Grenoble, France, 2003.*
- [72] C. T. Claire Tendero, Pascal Tristant, Jean Desmaison, Philippe Leprince, "Atmospheric pressure plasmas: A review," *Spectrochimica Acta Part B*, vol. 61, pp. 2-30, 2005.
- [73] V. I. Gibalov, G. J. Pietsch, "Dynamics of dielectric barrier discharges in different arrangements," *Plasma Sources Science and Technology*, vol. 21, no. 2, 2012, doi: 10.1088/0963-0252/21/2/024010.
- [74] T. B. Kai-Erik Elers, Marko Peussa, Brad Aitchison, Suvi Haukka, and Steven Marcus, "Film Uniformity in Atomic Layer Deposition," *Chem. Vap. Deposition*, vol. 12, pp. 13-24, 2006.
- [75] S. M. George, "Atomic Layer Deposition: An Overview," *Chem. Rev.*, vol. 110, pp. 111-131, 2010.
- [76] A. Hultqvist, S. F. Bent, Richard W. Johnson, "A brief review of atomic layer deposition from fundamentals to applications," *Materials Today*, vol. 17, no. 5, 2014.
- [77] T. U. E. Martijn Vos. "Atomic layer process development -10 steps to successfully develop, optimize and characterize ALD recipes." <https://www.atomiclimits.com/2019/02/12/atomic-layer-deposition-process-development-10-steps-to-successfully-develop-optimize-and-characterize-ald-recipes/> (accessed. 23/7/2019)
- [78] T. Suntola, "Atomic Layer Epitaxy," *Handbook of Crystal Growth*, vol. 3, Part B: Growth Mechanisms and Dynamics; Hurlle, D. T. J., Ed.; Elsevier: Amsterdam, 1994.
- [79] <http://www.chemspider.com/Chemical-Structure.9645106.html>. (accessed 08/09, 2019).
- [80] B. Macco, "Electron Scattering and Doping Mechanisms in Solid-Phase Crystallized In<sub>2</sub>O<sub>3</sub>:H Prepared by Atomic Layer Deposition," *ACS Appl. Mater. Interfaces*. doi: 10.1021/acsami.6b13560, 2015.
- [81] D.-W. Choi, W.J. Maeng, "Atomic layer deposition of highly conductive indium oxide using a liquid precursor and water oxidant," *Ceramics International*, 2015.
- [82] A. S. Ruslan Muydinov, Markus Wollgarten, Paweł Piotr Michałowski, A. P. Ulrike Bloeck, Darja Erfurt, Reiner Klenk, Stefan Körner, and I. L. a. B. Szyszka, "Crystallisation Phenomena of In<sub>2</sub>O<sub>3</sub>:H Films," *Materials*, vol. 12, no. 266, 2019, doi: 10.3390/ma12020266.
- [83] H. Wardenga, "In Situ Hall Effect Monitoring of Vacuum Annealing of In<sub>2</sub>O<sub>3</sub>:H Thin Films," *Materials*, vol. 8, pp. 561-574, 2015.
- [84] A. Technologies. "Corning® Eagle XG® LCD Glass Free of Heavy Metals." <https://abrisatechnologies.com/products-services/glass-products/specialty-glass/corning-eagle-xg/> (accessed 20/06, 2019).
- [85] "Crystallographic Open Database - Information card for 1010341." <http://www.crystallography.net/cod/1010341.html> (accessed 15/07, 2019).
- [86] Y. Wu, "Growth, phase and doping control in ZnO and In<sub>2</sub>O<sub>3</sub> thin films prepared by atomic layer deposition," Eindhoven University of Technology, 2016.
- [87] K. A. B. Subramanian, C. Sanjeeviraja, P. Kuppasami, M. Jayachandran "Reactive DC Magnetron Sputtered Zirconium Nitride (ZrN) Thin Film and its Characterization," *J. Phys.: Conf. Ser.*, vol. 114, 012039, 2008.

- [88] P. Scherrer, "Bestimmung der Grösse und der inneren Struktur von Kolloidteilchen mittels Röntgenstrahlen.," *Nachr. Ges. Wiss. Göttingen* vol. 26, pp. 98-100, 1918.
- [89] S. Z. K. S. Lalitha, P. Ravindran, S. Senthilarasu, R. Sathyamoorthy, J. Janabergenov., "Electronic structure, structural and optical properties of thermally evaporated CdTe thin films," *Physica B*, vol. 387, 227, 2007.
- [90] F. J. P. R. Sundaramoorthy, C. DeHart, T. Gennett, F.Y. Meng, M. Contreras, and T. Gessert, "Stability of TCO Window Layers for Thin-Film CIGS Solar Cells upon Damp Heat Exposures – Part II," *Reliability of Photovoltaic Cells, Modules, Components, and Systems II*, vol. 7412, 2009, doi: 10.1117/12.826604.
- [91] X. Y. Weimin Li, Armin G. Aberle & Selvaraj Venkataraj "Effect of sodium diffusion on the properties of CIGS solar absorbers prepared using elemental Se in a two-step process," *Scientific Reports*, vol. 9, no. 2637, 2019.
- [92] G. Z. H. Song, A. Yang, "The growth of ZnO on buffer layers and the valence band offset determined by X-ray photoemission spectroscopy," *Solid State Communications*, vol. 150, no. 41-42, pp. 1991–1994, doi: 10.1016/j.ssc.2010.08.022.
- [93] M. A. C. K. Ramanathan, J. R. Tuttle, "Effect of heat treatments and window layer processing on the characteristics of CuInGaSe<sub>2</sub> thin film solar cells," in *Proceedings of the 25th IEEE Photovoltaic Specialists Conference*, May, 1996, pp. 837-840.
- [94] N. D. Marco Giacomo Flammini, Maxime Le Ster, Brendan Dunne, Johan Bosman, and Mirjam Theelen, "The Influence of Heating Time and Temperature on the Properties of CIGSSe Solar Cells," *International Journal of Photoenergy*, vol. 2016, 2016.
- [95] T. Jäger *et al.*, "Improved open-circuit voltage in Cu(In,Ga)Se<sub>2</sub> solar cells with high work function transparent electrodes," *Journal of Applied Physics*, vol. 117, no. 22, 2015, doi: 10.1063/1.4922351.
- [96] S. K. a. T. Nakada, "High-temperature degradation mechanism of Cu(In,Ga)Se<sub>2</sub>-based thin filmsolar cells" *Applied Physics Express*, vol. 1, 7, 2008, Art no. 075002.
- [97] J. Y. D. S. Chen, F. Xu, "Effect of rapid thermal annealing on the compositional ratio and interface of Cu(In,Ga)Se<sub>2</sub> solar cells by XPS," *Applied Surface Science*, vol. 264, pp. 459-463.
- [98] S. S. L. X. Wang, W. K. Kim, "Solar Energy Materials and Solar Cells," vol. 90, pp. 2855-2866, Investigation of rapid thermal annealing on Cu(In,Ga)Se<sub>2</sub> films and solar cells.
- [99] T. G. K. J.-H.Wi, J.W.Kim, "Photovoltaic performance and interface behaviors of Cu(In,Ga)Se<sub>2</sub> solar cells with a sputtered-Zn(O,S) buffer layer by high-temperature annealing," *ACS Applied Materials and Interfaces*, vol. 7, pp. 17425-17432, 2015.
- [100] Y. S. F. Liu, Q. He, and Z. Zhou, "Rapid thermal annealing on dS/Cu(In, Ga)Se<sub>2</sub>-based solar cells," in *International Conference on Materials for Renewable Energy and Environment (ICMREE '13)*, Chengdu, China, August, 2013.
- [101] T. G. K. Jae-Hyung Wi, Jeong Won Kim, Woo-Jung Lee, Dae-Hyung Cho, Won Seok Han and Yong-Duck Chung, "Photovoltaic Performance and Interface Behaviors of CIGS Solar cells with a sputtered Zn(O,S) Buffer Layer by High Temperature Annealing," *ACS Applied Materials & Interfaces*, vol. 7, 31, 2015.
- [102] G. g. c. Sino. <http://www.globalsino.com/micro/1/1micro9919.html>. (accessed.29/7/2019).
- [103] H. Fujiwara, *Spectroscopic Ellipsometry*. Wiley, 2007.
- [104] R. A. Synowicki, "Suppression of backside reflections from transparent substrates," *physica status solidi* vol. 5, 5, pp. 1085-1088, 2008, doi: 10.1002.
- [105] H. Opto-Mechatronics. [https://www.holmarc.com/hall\\_effect\\_apparatus.php](https://www.holmarc.com/hall_effect_apparatus.php). (accessed. 29/7/2019)
- [106] P. Elmer. "Applications and Use of Integrating Spheres with the LAMBDA 650 and 850 UV/Vis and LAMBDA 950 UV/Vis/NIR Spectrophotometers." [https://www.perkinelmer.com/labsolutions/resources/docs/BRO\\_LAMBDA8509501050.pdf](https://www.perkinelmer.com/labsolutions/resources/docs/BRO_LAMBDA8509501050.pdf) (accessed. 29/7/2019)
- [107] Wikiwand. [http://www.wikiwand.com/en/Integrating\\_sphere](http://www.wikiwand.com/en/Integrating_sphere). (accessed. 29/7/2019)
- [108] S. Baskaran, "Structure and Regulation of Yeast Glycogen Synthase," University of California, Berkley. 2010.

- [109] M. A. Lieberman, Lichtenberg, Allan J., " Principles of plasma discharges and materials processing,"  
*Hoboken, N.J.: Wiley-Interscience.*, vol. 546, 2005